Prepared for submission to JHEP

Holographic Anisotropic Background with Confinement-Deconfinement Phase Transition

Irina Aref'eva[a] **and Kristina Rannu**[a,b]

[a] *Steklov Mathematical Institute, Russian Academy of Sciences, Gubkina str. 8, 119991, Moscow, Russia*

[b] *Peoples Friendship University of Russia, Miklukho-Maklaya str.6, 117198, Moscow, Russia*

E-mail: arefeva@mi.ras.ru, rannukristina@gmail.com

arXiv:1802.05652v3 [hep-th] 14 May 2018

Abstract: We present new anisotropic black brane solutions in 5D Einstein-dilaton-two-Maxwell system. The anisotropic background is specified by an arbitrary dynamical exponent ν, a nontrivial warp factor, a non-zero dilaton field, a non-zero time component of the first Maxwell field and a non-zero longitudinal magnetic component of the second Maxwell field. The blackening function supports the Van der Waals-like phase transition between small and large black holes for a suitable first Maxwell field charge. The isotropic case corresponding to $\nu = 1$ and zero magnetic field reproduces previously known solutions. We investigate the anisotropy influence on the thermodynamic properties of our background, in particular, on the small/large black holes phase transition diagram.

We discuss applications of the model to the bottom-up holographic QCD. The RG flow interpolates between the UV section with two suppressed transversal coordinates and the IR section with the suppressed time and longitudinal coordinates due to anisotropic character of our solution. We study the temporal Wilson loops, extended in longitudinal and transversal directions, by calculating the minimal surfaces of the corresponding probing open string world-sheet in anisotropic backgrounds with various temperatures and chemical potentials. We find that dynamical wall locations depend on the orientation of the quark pairs, that gives a crossover transition line between confinement/deconfinement phases in the dual gauge theory. Instability of the background leads to the appearance of the critical points $(\mu_{\vartheta,b}, T_{\vartheta,b})$ depending on the orientation ϑ of quark-antiquark pairs in respect to the heavy ions collision line.

Keywords: AdS/QCD, holography, phase transition

Contents

1 Introduction **2**

2 Black brane anisotropic solutions **4**
- 2.1 The equations of motion and boundary conditions 4
- 2.2 Solutions with factor $b(z) = \exp P(z)$ and spatial anisotropy 6
- 2.3 Solutions with factor $b(z) = \exp(cz^2/2)$ and spatial anisotropy 9
  - 2.3.1 Blackening function 9
  - 2.3.2 Coupling function f_2 12
  - 2.3.3 Scalar Field 14
  - 2.3.4 Scalar potential 17
- 2.4 Scalar invariants 20
- 2.5 RG flow 21

3 Thermodynamics of the background **28**
- 3.1 Temperature 28
- 3.2 Entropy 33
- 3.3 Free energy 36

4 Confinement-deconfinement phase transition **41**
- 4.1 Equation for the dynamical wall 41
- 4.2 $P(z) = cz^2/2$ 42
  - 4.2.1 Zero temperature 43
  - 4.2.2 Non-zero temperature, zero chemical potential 44
  - 4.2.3 Non-zero chemical potential 46
  - 4.2.4 The dynamical wall position 48
  - 4.2.5 Phase transition lines and critical points 50

5 Conclusion and discussion **54**

A Equations of motion **57**

B Simplest solutions to system (2.5)–(2.10) **59**
- B.1 Solutions for anisotropic metric $\nu \neq 1$ and $c = 0$, $A_t \neq 0$ 59
- B.2 Solutions for anisotropic metric $\nu \neq 1$ and $c = 0$, $A_t = 0$ 60
- B.3 Vacuum solutions 61

1 Introduction

Study of the phase diagram of QCD, as a function of temperature T and chemical potential μ, corresponding to baryon density or some other conserved charge, is one of the great modern challenge. The diagram of QCD displays a rich structure [1, 2]. Particularly interesting and important features of the phase diagram are the nature of the chiral phase transition, the location of the chiral critical point and its properties. There are well known obstacles to study this problem by usual tools, such as perturbative theory or lattice calculations.

The gravity/gauge duality provides an alternative tool for understanding dynamics of the strong coupling system, where standard methods are not enough. One such system is the quark-gluon plasma (QGP) produced in the heavy-ions-collisions (HIC) [3–5]. It is believed that the QGP is created in a very short time after the collision ($\tau_{\rm therm} \approx$ few $0.1\,{\rm fm}/c$) and there are indications that during this time the QGP is anisotropic [6]. In [7] we have considered a special anisotropic backgrounds, parametrized by the dynamical exponent ν, and found out that the shock wave model of HIC for $\nu = 4.45$ reproduces the experimental energy dependence of the total multiplicity, $\mathcal{M} \sim s^{0.155}$ [8]. Note that all attempts to reproduce this dependence in isotropic models failed [9–21].

On the other hand, static holographic models perfectly reproduce main properties of QCD [3–5, 22]. Therefore, it would be interesting to know how these properties are changed in anisotropic backgrounds. Some of these questions have been already addressed in [23–36] and refs therein. In particular, in [35] the confinement-deconfinement crossover transition in the temperature-chemical potential plane has been observed. However, in this paper, analogous to [37] and many others [38–43], it was not assumed that the metric is supported by some Lagrangian. Let us remind, that for the isotropic case, $\nu = 1$, the background used in [37] was constructed in [44] as a solution of equations of motion in the Einstein-dilaton theory. Later, this background has been generalized for non-zero electro-field [45, 46] in the Einstein-dilaton-Maxwell theory in order to describe the confinement-deconfinement phase transition holographically, (see also [42, 43, 47–49] and early papers [50–52]). The anisotropic $\nu \neq 1$ black brane background with a trivial warp factor and a non-zero electro-magnetic field has been constructed in [33]. As it already has been mentioned, the collision of shock waves in this 5-dimensional dual vacuum background gives the total multiplicity dependence on energy in the form $\mathcal{M} \sim s^{0.155}$, which reproduces the experimental dependence [8].

This paper is devoted to the construction of the anisotropic 5-dimensional background specified by an arbitrary dynamical exponent ν, a nontrivial warp factor, a non-zero time component of the first Maxwell field and a non-zero longitudinal magnetic component of the second Maxwell field. To see clearly possible new effects caused

by anisotropy, it is useful to deal with an explicit analytical solution. For this purpose we take the particular case of the simplest warp factor $b(z) = e^{\frac{cz^2}{2}}$. We find the dilaton potential by the potential reconstruction method similar to the isotropic case [46] (and refs therein). We show that only $c \leq 0$ guarantees real solutions for the dilaton (compare with [19] and refs therein). We construct the blackening function that supports the Van der Waals-like phase transition between small and large black holes for a suitable first Maxwell field charge. The isotropic case corresponding to $\nu = 1$ and zero magnetic field reproduces previously known solutions [45, 46]. We investigate the anisotropy influence on the thermodynamic properties of our background, in particular, on the small/large black holes phase transition diagram. We find that the anisotropy changes the location of the domain of instability.

We also discuss applications of the model to the bottom-up holographic QCD. We note that the RG flow interpolates between the UV section with two transversal suppressed coordinates and the IR section with the suppressed time and longitudinal coordinates due to anisotropic character of our solution. We study the temporal Wilson loops extended in longitudinal and transversal directions by calculating the minimal surfaces of the corresponding probing open string world-sheet for various values of temperature and chemical potential. We find that for particular sets of the model parameters the dynamical wall appears. The appearance of dynamical walls also depends on the orientation of the temporal Wilson loop, that gives a crossover transition line between confinement-deconfinement phases in the dual gauge theory. This effect has been also observed in the anisotropic model considered in [35]. In the background, investigated in the present paper, there are two more anisotropic effects. Namely, the instability of the background restricts leads to the appearance of critical points $(\mu_{\vartheta,b}, T_{\vartheta,b})$. Each critical point is located at intersection of the confinement/deconfinement open string phase transition line and the small/large black holes phase transition line of our background. The lines of the first type depend on orientation of the quark-antiquark pairs and the lines of the second type are fixed for the given anisotropy parameter ν. In other words, positions of the critical points $(\mu_{\vartheta,b}, T_{\vartheta,b})$ depend on the orientation of quark-antiquark pair in respect to the heavy ions collision line. Averaging on all possible orientations on the quark-antiquark pairs, one gets a family of the critical points. In our model it also happens, that the confinement/deconfinement transition line, oriented along the transversal direction, is below the small/large black holes phase transition line. This means that near the small chemical potential the small/large black hole transition line is hidden by the confinement/deconfinement transition line for the pair of quarks oriented in the transverse direction. Recall that a small/large black holes transition line near the top of the holographic phase diagram is treated as

a problem, since this behavior is not supported neither by experimental data nor by calculations performed in the framework of effective theories. Let us also remind, that most of the effective models suggest the existence of a QCD critical point (μ_{CEP}, T_{CEP}) somewhere in the middle of the phase diagram, where the crossover line becomes a first order transition line. There were attempts to relate (μ_{CEP}, T_{CEP}) with the small/large black holes background transition [51, 52], but here there is a problem with the first order phase transition in the top of the QCD phase diagram, that is not present at the QCD phase diagram [1, 2]. The isotropic holographic model improving this has been proposed in [49] just by removing the small/large black holes background transition, see also [53, 54]. We note, that the presence of the small/large black holes background transition endows our anisotropic model by a rich phase structure.

The paper is organized as follows. In Sect. 2 we construct the anisotropic 5-dimensional solution with an arbitrary dynamical exponent ν, a nontrivial warp factor, a non-zero time component of the first Maxwell field and a non-zero longitudinal magnetic component of the second Maxwell field. In Sect. 2.3 we consider exponential warp factors with quadratic exponent and show that only negative definite quadratic form guarantees the real solutions for the dilaton. In Sect. 3 we discuss the thermodynamics of the constructed background and find out the small/large black holes transition line in the (μ, T)-plane. Sections 2.5 and 4 are devoted to applications to QCD. In Sect. 2.5 we shortly discuss the RG flows corresponding to constructed solutions. In Sect. 4.1 we find dynamical walls corresponding to the temporal Wilson loops extended in the longitudinal and transversal directions. In Sect. 4.2.5 we determine the relative position of the background and the confinement-deconfinement phase transition lines and discuss the corresponding critical points. In Appendix A we derive E.O.M. and in Appendix B we present simplest solutions, the black hole solutions for $c = 0$, with zero and non-zero chemical potential, and the vacuum solution for $c < 0$ for completeness.

2 Black brane anisotropic solutions

2.1 The equations of motion and boundary conditions

We consider a 5-dimensional Einstein-dilaton-two-Maxwell system. In the Einstein frame the action of the system is specified as

$$S = \int \frac{d^5x}{16\pi G_5}\sqrt{-\det(g_{\mu\nu})}\left[R - \frac{f_1(\phi)}{4}F_{(1)}^2 - \frac{f_2(\phi)}{4}F_{(2)}^2 - \frac{1}{2}\partial_\mu\phi\partial^\mu\phi - V(\phi)\right], \quad (2.1)$$

where $F_{(1)}^2$ and $F_{(2)}^2$ are the squares of the Maxwell fields $F_{\mu\nu}^{(1)} = \partial_\mu A_\nu - \partial_\nu A_\mu$ and $F_{\mu\nu}^{(2)} = q\, dy^1 \wedge dy^2$, $f_1(\phi)$ and $f_2(\phi)$ are the gauge kinetic functions associated with the

corresponding Maxwell fields, $V(\phi)$ is the potential of the scalar field ϕ.

We search the black brane solution in the anisotropic background. For this purpose we use the metric ansatz in the following form:

$$ds^2 = \frac{L^2\, b(z)}{z^2}\left[-\, g(z)dt^2 + dx^2 + z^{2-\frac{2}{\nu}}\left(dy_1^2 + dy_2^2\right) + \frac{dz^2}{g(z)}\right], \tag{2.2}$$

$$\phi = \phi(z), \qquad A_\mu^{(1)} = A_t(z)\delta_\mu^0, \tag{2.3}$$

$$F_{\mu\nu}^{(2)} = q\; dy^1 \wedge dy^2, \tag{2.4}$$

where $b(z)$ is the warp factor and $g(z)$ is the blackening function; we set the AdS radius $L = 1$ and all the quantities in formulas and figures are presented in dimensionless units.

The variation of the action (2.1) over metric components $g_{\mu\nu}$ gives 4 independent equations, corresponding to 00-, 11-, 22- and 44-components of the Einstein tensor, that are presented in the Appendix A. These equations can be transformed to the following ones:

$$g'' + g'\left(\frac{3b'}{2b} - \frac{1}{z} - \frac{2}{\nu z}\right) - \frac{z^2}{b} f_1 A_t'^2 = 0, \tag{2.5}$$

$$b'' - \frac{3(b')^2}{2b} + \frac{2b'}{z} - \frac{4b}{3\nu z^2}\left(1 - \frac{1}{\nu}\right) + \frac{b}{3}(\phi')^2 = 0, \tag{2.6}$$

$$2g'\left(1 - \frac{1}{\nu}\right) + g\left(1 - \frac{1}{\nu}\right)\left(\frac{3b'}{b} - \frac{4}{z} - \frac{4}{\nu z}\right) + \frac{q^2 z^{-1+\frac{4}{\nu}}}{b} f_2 = 0, \tag{2.7}$$

$$-V - \frac{z^4}{2b^2} A_t'^2 f_1 - \frac{3z^2 b' g'}{2b^2} - \frac{3z^2 g b'^2}{b^3} + \frac{9zgb'}{2\nu b^2} + \frac{15zgb'}{2b^2} + \frac{zg'}{\nu b} + \frac{2zg'}{b} + \\ + \frac{z^2 g \phi'^2}{2b} - \frac{8g}{\nu b} - \frac{4g}{b} = 0. \tag{2.8}$$

Here and below $' = d/dz$. The variation of the action (2.1) over the scalar field ϕ and the components $A_\mu^{(1)}$ of the first Maxwell field leads to the following EOM:

$$\phi'' + \phi'\left(\frac{g'}{g} + \frac{3b'}{2b} - \frac{\nu+2}{\nu z}\right) + \frac{z^2 A_t'^2}{2bg}\frac{\partial f_1}{\partial \phi} - \frac{q^2 z^{-2+\frac{4}{\nu}}}{2bg}\frac{\partial f_2}{\partial \phi} - \frac{b}{z^2 g}\frac{\partial V}{\partial \phi} = 0, \tag{2.9}$$

$$A_t'' + A_t'\left(\frac{b'}{2b} + \frac{f_1'}{f_1} - \frac{2-\nu}{\nu z}\right) = 0 \tag{2.10}$$

The EOM for the second Maxwell field doesn't give any contribution into system (2.5)–(2.10) as its left-hand side is identically zero:

$$\partial_\mu\left(\sqrt{-g}\, f_2(\phi)\, F_{(2)}^{\mu\nu}\right) = \partial_4\left(\sqrt{-g}\, f_2(\phi)\, F_{(2)}^{4\nu}\right) \equiv 0.$$

We also impose the boundary conditions in the form:

$$b(0) = 1 \tag{2.11}$$

$$g(0) = 1 \quad \text{and} \quad g(z_h) = 0, \tag{2.12}$$

$$A_t(0) = \mu \quad \text{and} \quad A_t(z_h) = 0, \tag{2.13}$$

where z_h is the horizon. As to the scalar field, it is natural to require that $\phi(z)$ is real for $0 < z \leq z_h$ and that

$$\phi(z_h) = 0. \tag{2.14}$$

2.2 Solutions with factor $b(z) = \exp P(z)$ and spatial anisotropy

One can use the following strategy to find particular solutions of the system of equations (2.5)–(2.10).

- Choose the form of functions $b(z)$ and $f_1(z)$.
- Using these $b(z)$ and $f_1(z)$, find the time component of the electric field $A_t(z)$ from (2.10).
- Using $f_1(z)$, $b(z)$ and $A_t'(z)$, get the blackening function $g(z)$ from (2.5).
- Using $b(z)$, find the derivative of the scalar field $\phi'(z)$ from (2.6). To have a solution one has to be sure that

$$b'' - \frac{3b'^2}{2b} + \frac{2b'}{z} - \frac{4b(\nu-1)}{3\nu^2 z^2} \leq 0. \tag{2.15}$$

- Using $g(z)$ and $b(z)$, get $f_2(z)$ from (2.7).
- Finally, get $V = V(z)$ from (2.8).

Let us express the warp factor $b(z)$ via a polynomial $P(z)$[1]:

$$b(z) = e^{P(z)}, \tag{2.16}$$

and take the coupling factor $f_1(z)$:

$$f_1(z) = z^{-2+\frac{2}{\nu}}. \tag{2.17}$$

[1]For the isotropic case this form of factor b has been considered, in particular, in [45, 46], other form of this factor has been also considered in [55].

In this case the equation (2.10) becomes

$$A_t'' + A_t' \left(\frac{P'(z)}{2} - \frac{1}{z} \right) = 0 \tag{2.18}$$

and it's solution has the form

$$A_t = C_1 \int_0^z e^{-\frac{P(\xi)}{2}} \xi d\xi + C_2. \tag{2.19}$$

If we take into account the boundary conditions (2.13), the integration constants equal to

$$C_1 = -\frac{\mu}{\int_0^{z_H} e^{-\frac{P(\xi)}{2}} \xi d\xi} = -\tilde{\mu}, \quad C_2 = \mu \tag{2.20}$$

and the solution (2.19) becomes

$$A_t = \mu \left(1 - \frac{\int_0^z e^{-\frac{P(\xi)}{2}} \xi d\xi}{\int_0^{z_H} e^{-\frac{P(\xi)}{2}} \xi d\xi} \right) = \tilde{\mu} \int_z^{z_H} e^{-\frac{P(\xi)}{2}} \xi d\xi. \tag{2.21}$$

In a similar way equation (2.5) takes the form

$$g'' + g' \left(\frac{3}{2} P'(z) - \frac{1}{z} - \frac{2}{\nu z} \right) - \tilde{\mu}\, e^{-2P(z)} z^{2+\frac{2}{\nu}} = 0, \tag{2.22}$$

and its solution is:

$$g = C_4 + \int_0^z e^{-\frac{3P(\xi)}{2}} \left(C_3 + \tilde{\mu}^2 \int_0^\xi e^{-\frac{P(\chi)}{2}} \chi d\chi \right) \xi^{1+\frac{2}{\nu}} d\xi. \tag{2.23}$$

Using the first boundary condition in (2.12) we can determine the integration constant $C_4 = 1$, and taking into account the boundary condition on the horizon we find C_3

$$C_3 = -\frac{1 + \tilde{\mu}^2 \int_0^{z_H} e^{-\frac{3P(\xi)}{2}} \left(\int_0^\xi e^{-\frac{P(\chi)}{2}} \chi d\chi \right) \xi^{1+\frac{2}{\nu}} d\xi}{\int_0^{z_H} e^{-\frac{3P(\xi)}{2}} \xi^{1+\frac{2}{\nu}} d\xi}, \tag{2.24}$$

therefore the solution (2.23) becomes:

$$\begin{aligned} g = 1 &+ \tilde{\mu}^2 \int_0^z e^{-\frac{3P(\xi)}{2}} \left(\int_0^\xi e^{-\frac{P(\chi)}{2}} \chi d\chi \right) \xi^{1+\frac{2}{\nu}} d\xi \\ &- \frac{1 + \tilde{\mu}^2 \int_0^{z_H} e^{-\frac{3P(\xi)}{2}} \left(\int_0^\xi e^{-\frac{P(\chi)}{2}} \chi d\chi \right) \xi^{1+\frac{2}{\nu}} d\xi}{\int_0^{z_H} e^{-\frac{3P(\xi)}{2}} \xi^{1+\frac{2}{\nu}} d\xi} \int_0^z e^{-\frac{3P(\xi)}{2}} \xi^{1+\frac{2}{\nu}} d\xi. \end{aligned} \tag{2.25}$$

Equation (2.7) gives the following expression for the coupling function $f_2(z)$:

$$f_2(z) = -\frac{\nu-1}{q^2\nu}\, e^{P(z)} z^{1-\frac{4}{\nu}} \left[2e^{-\frac{3P(z)}{2}} z^{1+\frac{2}{\nu}} \left(C_3 + \tilde{\mu}^2 \int_0^z e^{-\frac{P(\xi)}{2}} \xi d\xi \right) \right. \tag{2.26}$$
$$\left. + \frac{3z\nu P'(z) - 4(\nu+1)}{z\nu} \left(1 + C_3 \int_0^z e^{-\frac{3P(\xi)}{2}} \xi^{1+\frac{2}{\nu}} d\xi + \tilde{\mu}^2 \int_0^z e^{-\frac{3P(\xi)}{2}} \left(\int_0^\xi e^{-\frac{P(\chi)}{2}} \chi d\chi \right) \xi^{1+\frac{2}{\nu}} d\xi \right) \right].$$

Equation (2.6) allows to find the scalar field $\phi(z)$:

$$\phi(z) = C_5 + \int_0^z \sqrt{-3P''(\xi) + \frac{3}{2}P'^2(\xi) - \frac{6}{\xi}P'(\xi) + 4\,\frac{\nu-1}{\xi^2\nu^2}}\, d\xi. \tag{2.27}$$

Using the boundary condition (2.14), we get

$$C_5 = -\int_0^{z_h} \sqrt{-3P''(\xi) + \frac{3}{2}P'^2(\xi) - \frac{6}{\xi}P'(\xi) + 4\,\frac{\nu-1}{\xi^2\nu^2}}\, d\xi \tag{2.28}$$

and therefore

$$\phi(z) = \int_{z_h}^z \sqrt{-3P''(\xi) + \frac{3}{2}P'^2(\xi) - \frac{6}{\xi}P'(\xi) + 4\,\frac{\nu-1}{\xi^2\nu^2}}\, d\xi. \tag{2.29}$$

Finally, equation (2.8) gives the scalar potential $V(\phi(z))$:

$$V(\phi(z)) = \frac{9}{2}P'(z)\, e^{-P(z)} z \left[1 + \frac{1}{\nu} - C_3 \left(\frac{e^{-\frac{3P(z)}{2}}}{2}\, z^{2+\frac{2}{\nu}} - \left(1+\frac{1}{\nu}\right) \int_0^z e^{-\frac{3P(\xi)}{2}} \xi^{1+\frac{2}{\nu}} d\xi \right) \right.$$
$$\left. + \tilde{\mu}^2 \left(\frac{e^{-\frac{3P(z)}{2}}}{2}\, z^{2+\frac{2}{\nu}} \int_0^z e^{-\frac{P(\xi)}{2}} \xi d\xi - \left(1+\frac{1}{\nu}\right) \int_0^z e^{-\frac{3P(\xi)}{2}} \left(\int_0^\xi e^{-\frac{P(\chi)}{2}} \chi d\chi \right) \xi^{1+\frac{2}{\nu}} d\xi \right) \right]$$
$$+ \frac{3}{2}\, e^{-P(z)} z^2 \left(P''(z) + \frac{3}{2}\, P'^2(z) + 4\,\frac{1+3\nu+2\nu^2}{2z^2\nu^2} \right) \tag{2.30}$$
$$\times \left[1 + C_3 \int_0^z e^{-\frac{3P(\xi)}{2}} \xi^{1+\frac{2}{\nu}} d\xi + \tilde{\mu}^2 \int_0^z e^{-\frac{3P(\xi)}{2}} \left(\int_0^\xi e^{-\frac{P(\chi)}{2}} \chi d\chi \right) \xi^{1+\frac{2}{\nu}} d\xi \right]$$
$$+ e^{-\frac{5P(z)}{2}} z^{2+\frac{2}{\nu}} \left[\left(\frac{3}{4}P'(z)\, z + 2 + \frac{1}{\nu} \right) \left(C_3 + \tilde{\mu}^2 \int_0^z e^{-\frac{P(\xi)}{2}} \xi d\xi \right) - \tilde{\mu}^2\, e^{-\frac{P(z)}{2}}\, \frac{z^2}{2} \right].$$

If we substitute the expressions (2.16), (2.17), (2.21) and (2.25)–(2.30) into the constraint (2.9) and take into account that $\partial V/\partial\phi = V'/\phi'$, we can make certain that the left-hand side of (2.9) disappears. Therefore the system (2.5)–(2.10) is self-consistent and satisfied by the general solution (2.16), (2.17), (2.21) and (2.25)–(2.30).

2.3 Solutions with factor $b(z) = \exp(cz^2/2)$ and spatial anisotropy

As we are interested in effects that can be caused by the anisotropy of the chosen metric ansatz, it is needed to find some particular solution of the system (2.5)–(2.10) and investigate it's properties explicitly. For this purpose we preferred to start from the simplest form of the warp-factor, the same as in [37]:

$$b(z) = e^{\frac{cz^2}{2}}, \tag{2.31}$$

and take the factor $f_1(z)$:

$$f_1 = z^{-2+\frac{2}{\nu}}. \tag{2.32}$$

In this case the equation (2.5) becomes

$$A_t'' + A_t' \left(\frac{cz}{2} - \frac{1}{z} \right) = 0, \tag{2.33}$$

and together with the boundary conditions

$$A_t(0) = \mu, \qquad A_t(z_h) = 0 \tag{2.34}$$

this gives

$$A_t(z) = \mu \frac{e^{-\frac{cz^2}{4}} - e^{-\frac{cz_h^2}{4}}}{1 - e^{-\frac{cz_h^2}{4}}}. \tag{2.35}$$

2.3.1 Blackening function

Using the solution (2.35) and f_1 given by (2.17), we rewrite equation (2.5) for the blackening function:

$$g'' + g' \left(\frac{3cz}{2} - \frac{1}{z} - \frac{2}{\nu z} \right) - \frac{\mu^2 c^2 \; z^{2+\frac{2}{\nu}} \; e^{-cz^2}}{4 \left(1 - e^{-\frac{cz_H^2}{4}} \right)^2} = 0. \tag{2.36}$$

Taking into account the boundary conditions (2.12), we get

$$\begin{aligned} g(z) = 1 &- \frac{\gamma(1+\frac{1}{\nu}; \frac{3}{4}cz^2)}{\gamma(1+\frac{1}{\nu}; \frac{3}{4}cz_h^2)} - \frac{\mu^2 e^{\frac{1}{2}cz_h^2}}{4c^{1/\nu}} \frac{\gamma(1+\frac{1}{\nu}; cz^2)}{(1 - e^{\frac{1}{4}cz_h^2})^2} \\ &+ \frac{\mu^2 e^{\frac{1}{2}cz_h^2}}{4c^{1/\nu}} \frac{\gamma(1+\frac{1}{\nu}; cz_h^2)}{(1 - e^{\frac{1}{4}cz_h^2})^2} \frac{\gamma\left(1+\frac{1}{\nu}; \frac{3}{4}cz^2\right)}{\gamma(1+\frac{1}{\nu}; \frac{3}{4}cz_h^2)}, \end{aligned} \tag{2.37}$$

where $\gamma(1+\frac{1}{\nu},x)$ is the incomplete gamma function.

There is no problem with solution in such a form for $c>0$, but for $c<0$ some ingredients of this presentation seem to fail. Indeed, $c^{1/\nu}$ is ill-defined for $c<0$. By this reason we rewrite the above formula as

$$g(z)=1-\frac{z^{2+\frac{2}{\nu}}}{z_h^{2+\frac{2}{\nu}}}\,\frac{\mathfrak{G}(\frac{3}{4}cz^2)}{\mathfrak{G}(\frac{3}{4}cz_h^2)}-\frac{\mu^2cz^{2+\frac{2}{\nu}}e^{\frac{cz_h^2}{2}}}{4\left(1-e^{\frac{cz_h^2}{4}}\right)^2}\,\mathfrak{G}(cz^2)+\frac{\mu^2cz^{2+\frac{2}{\nu}}e^{\frac{cz_h^2}{2}}}{4\left(1-e^{\frac{cz_h^2}{4}}\right)^2}\,\frac{\mathfrak{G}(\frac{3}{4}cz^2)}{\mathfrak{G}(\frac{3}{4}cz_h^2)}\,\mathfrak{G}(cz_h^2), \tag{2.38}$$

where

$$\mathfrak{G}(x)=x^{-1-\frac{1}{\nu}}\,\gamma\left(1+\frac{1}{\nu},x\right) \tag{2.39}$$

and the function $\mathfrak{G}(x)$ has the following expansion (see [56], p. 1377):

$$\mathfrak{G}(x)=\sum_{n=0}^{\infty}\frac{(-1)^n\,x^n}{n!(1+n+\frac{1}{\nu})}. \tag{2.40}$$

Taking into account the first two terms of the expansion (2.40), we get

$$g_{appr}(z)=1-\frac{z^{2+\frac{2}{\nu}}}{z_h^{2+\frac{2}{\nu}}}\left(\rho+Qz_h^2-Qz^2\right), \tag{2.41}$$

where

$$\rho=\frac{4(1+2\nu)-3cz^2(1+\nu)}{4(1+2\nu)-3cz_h^2(1+\nu)}, \tag{2.42}$$

$$Q=\frac{\mu^2c^2\nu\,z_h^{2+\frac{2}{\nu}}e^{\frac{cz_h^2}{2}}}{4\left(1-e^{\frac{cz_h^2}{4}}\right)^2\left(4(1+2\nu)-3cz_h^2(1+\nu)\right)}. \tag{2.43}$$

This expression can be recast into a form

$$g_{appr}(z)=1-z^{2+\frac{2}{\nu}}\left(\left(\frac{\rho}{z_h}\right)^{2+\frac{2}{\nu}}+\frac{Q}{z_h^{2/\nu}}\right)+Q\,\frac{z^{4+\frac{2}{\nu}}}{z_h^{2+\frac{2}{\nu}}}, \tag{2.44}$$

and after the redefinition $z_h=\tilde{z}_h\rho$, $Q=\tilde{Q}z_h^{2+\frac{2}{\nu}}$ it becomes

$$g_{appr}(z)=1-z^{2+\frac{2}{\nu}}\left(\frac{1}{\tilde{z}_h^{2+\frac{2}{\nu}}}+\tilde{Q}\rho^2\tilde{z}_h^2\right)+\tilde{Q}\,z^{4+\frac{2}{\nu}}. \tag{2.45}$$

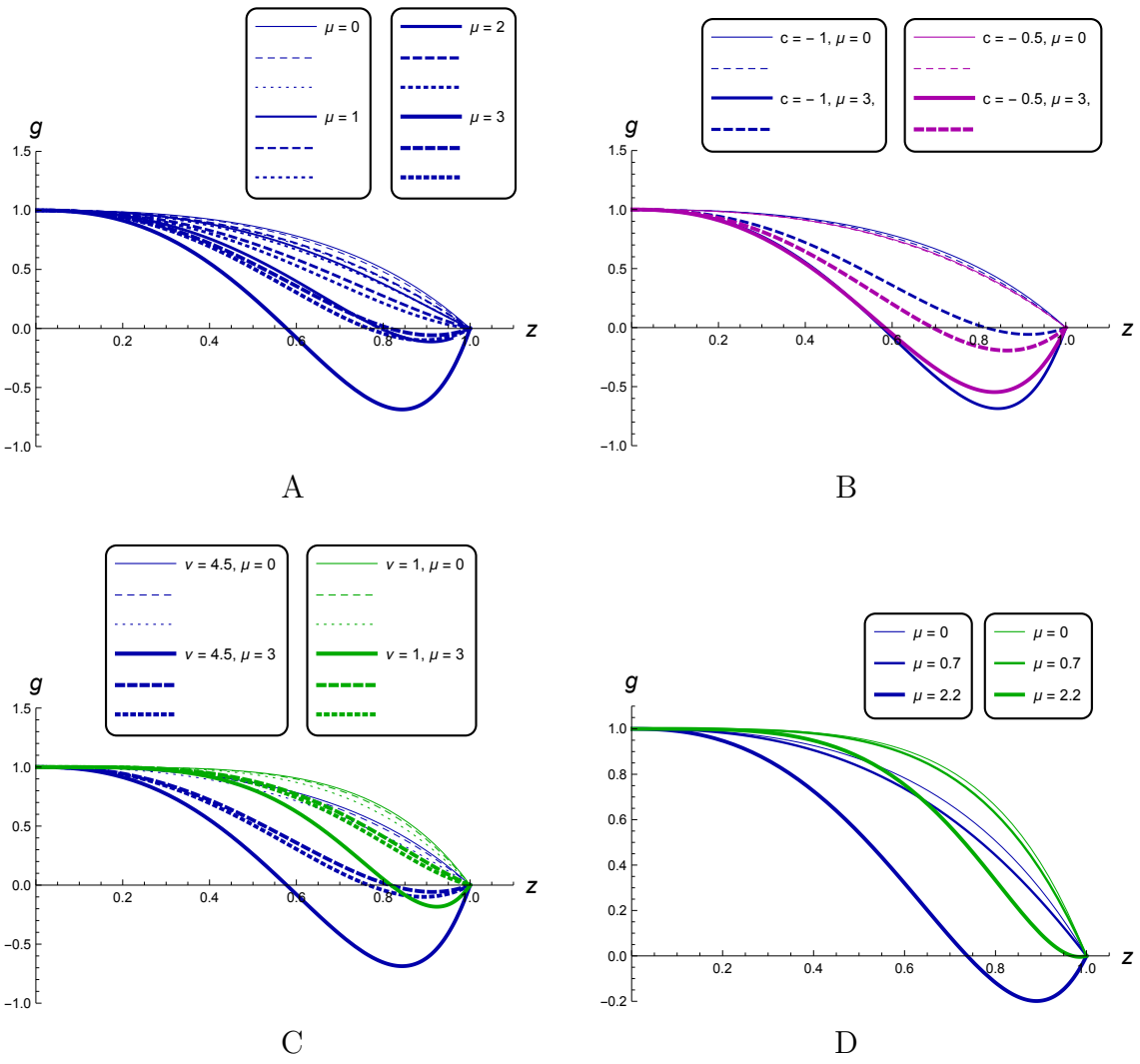


Figure 1. Blackening functions $g(z)$ (solid lines), $g_{approx}(z)$ (same thickness dashed lines) and $g_{approx,[2]}(z)$ (same thickness dotted lines) for $z_h = 1$, $\nu = 4.5$, $c = -1$ (blue lines), $\nu = 4.5$, $c = -0.5$ (magenta lines), $\nu = 1$, $c = -1$ (green lines) and different $\mu = 0, \ldots, 3$.

The blackening function used in [4]

$$g_{[2]}(z) = 1 - z^{2+\frac{2}{\nu}} \left(\frac{1}{z_h^{2+\frac{2}{\nu}}} + Q z_h^2 \right) z^{2+\frac{2}{\nu}} + Q z^{4+\frac{2}{\nu}} \tag{2.46}$$

is different by the factor ρ^2 in the second coefficient in front of $z^{2+\frac{2}{\nu}}$. Near the horizon this factor is approximately equal to 1:

$$\rho \approx 1 - \frac{6cz_h(1+\nu)}{4(1+2\nu) - 3cz_h^2(1+\nu)}\,(z-z_h) + \mathcal{O}((z-z_h)^2). \tag{2.47}$$

The behavior of the blackening function from the holographic coordinate z till horizon is depicted on Fig.1. The main feature is that the blackening function values decrease faster for larger chemical potential μ (Fig.1.A) and for smaller warp factor coefficient c (Fig.1.B). The difference between the approximations (2.45) and (2.46) and the exact expression (2.37) is irregular and depends on the model parameters (Fig.1.C). In the isotropic case the blackening function values are larger than in the anisotropic ones (Fig.1.C and D). For μ close to zero it is the desreasing function of z till the horizon, but for growing μ the local minimums and the second horizons small than the original ones appear. Changing the values of c almost does not influence on the horizon position.

2.3.2 Coupling function f_2

We can substitute the expression for the blackening function (2.38) into (2.7), take into account

$$g'(z) = -2\,\frac{z^{1+\frac{2}{\nu}}}{z_h^{2+\frac{2}{\nu}}}\,\frac{e^{-\frac{3cz^2}{4}}}{\mathfrak{G}(\frac{3}{4}cz_h^2)} - \frac{\mu^2 c\, z^{1+\frac{2}{\nu}}\, e^{-cz^2+\frac{cz_h^2}{2}}}{2\left(1-e^{\frac{cz_h^2}{4}}\right)^2}\left(1 - e^{\frac{cz^2}{4}}\,\frac{\mathfrak{G}(cz_h^2)}{\mathfrak{G}(\frac{3}{4}cz_h^2)}\right) \tag{2.48}$$

and get

$$f_2(z) = \frac{\nu-1}{q^2\nu^2}\, z^{-\frac{4}{\nu}} e^{\frac{cz^2}{2}}\left[4(1+\nu) - 3c\,\nu\, z^2 + 4\,\frac{z^{2+\frac{2}{\nu}}}{z_h^{2+\frac{2}{\nu}}}\left\{\frac{\nu\, e^{-\frac{3cz^2}{4}}}{\mathfrak{G}\left(\frac{3}{4}cz_h^2\right)} - (1+\nu)\,\frac{\mathfrak{G}\left(\frac{3}{4}cz^2\right)}{\mathfrak{G}\left(\frac{3}{4}cz_h^2\right)}\,\mathfrak{F}\right.\right.$$
$$\left.\left. + \frac{\mu^2 c\,\nu\, z_h^{2+\frac{2}{\nu}} e^{-cz^2+\frac{cz_h^2}{2}}}{4\left(1-e^{\frac{cz_h^2}{4}}\right)^2}\left(1 - e^{\frac{cz^2}{4}}\,\frac{\mathfrak{G}\left(cz_h^2\right)}{\mathfrak{G}\left(\frac{3}{4}cz_h^2\right)}\right)\right\} + 3c\,\nu\,\frac{z^{4+\frac{2}{\nu}}}{z_h^{2+\frac{2}{\nu}}}\,\frac{\mathfrak{G}\left(\frac{3}{4}cz^2\right)}{\mathfrak{G}\left(\frac{3}{4}cz_h^2\right)}\,\mathfrak{F}\right], \tag{2.49}$$

where

$$\mathfrak{F} = 1 - \frac{\mu^2 c\, z_h^{2+\frac{2}{\nu}} e^{\frac{cz_h^2}{2}}}{4\left(1-e^{\frac{cz_h^2}{4}}\right)^2}\left(\mathfrak{G}\left(cz_h^2\right) - \mathfrak{G}\left(cz^2\right)\,\frac{\mathfrak{G}\left(\frac{3}{4}cz_h^2\right)}{\mathfrak{G}\left(\frac{3}{4}cz^2\right)}\right). \tag{2.50}$$

At the horizon

$$f_2(z_h) = 4\,\frac{\nu-1}{q^2\nu}\, z^{-\frac{4}{\nu}}\left\{\frac{e^{-\frac{cz_h^2}{4}}}{\mathfrak{G}\left(\frac{3}{4}cz_h^2\right)} + \frac{\mu^2 c\, z_h^{2+\frac{2}{\nu}}}{4\left(1-e^{\frac{cz_h^2}{4}}\right)^2}\left(1 - e^{\frac{cz_h^2}{4}}\,\frac{\mathfrak{G}\left(cz_h^2\right)}{\mathfrak{G}\left(\frac{3}{4}cz_h^2\right)}\right)\right\}. \tag{2.51}$$

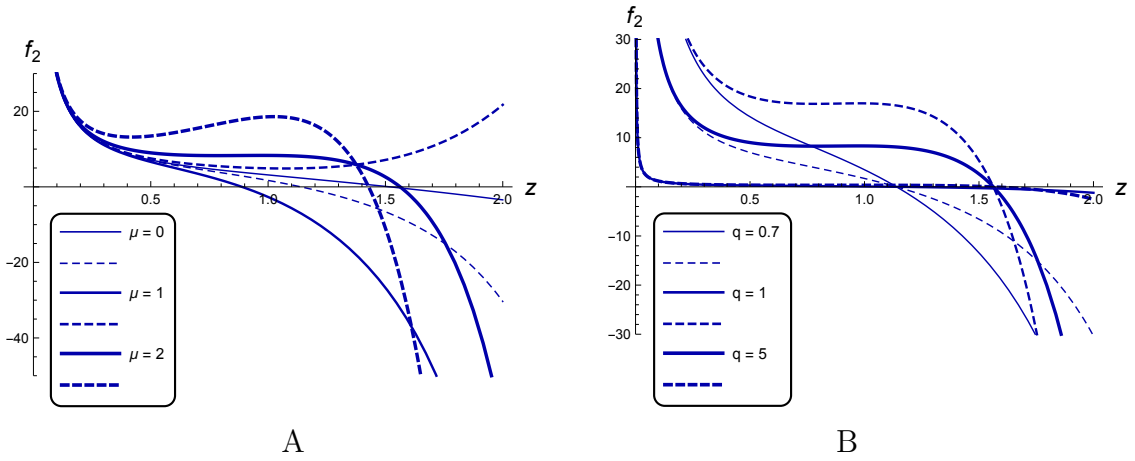


Figure 2. Coupling function $f_2(z)$ (solid lines) and $f_{2\ approx}$ (same thickness dashed lines) for $z_h = 1$, $\nu = 4.5$, $c = -1$, $q = 1$, $\mu = 0,\ 1,\ 5$ (A) and $\mu = 1$, $q = 0.7,\ 1,\ 5$ (B).

Using the first two terms of the expansion (2.40) on z and z_h

$$\mathfrak{G}(cz_{(h)}^2) = \frac{\nu}{\nu+1} - \frac{c\,\nu\,z_{(h)}^2}{2\nu+1}, \tag{2.52}$$

$$\mathfrak{G}\left(\frac{3}{4}\,cz_{(h)}^2\right) = \left(\frac{3}{4}\right)^{1+\frac{1}{\nu}}\left(\frac{\nu}{\nu+1} - \frac{3}{4}\,\frac{c\nu z_{(h)}^2}{2\nu+1}\right), \tag{2.53}$$

we have the following expansion of coupling factor f_2:

$$\begin{aligned} f_{2\ approx}(z) = {} & \frac{\nu-1}{q^2\nu^2}\,z^{-\frac{4}{\nu}}e^{\frac{cz^2}{2}}\Bigg[4(1+\nu) - 3c\nu z^2 \\ & + \frac{z^{2+\frac{2}{\nu}}}{z_h^{2+\frac{2}{\nu}}}\Bigg\{\frac{16(1+\nu)(1+2\nu)}{3cz_h^2(1+\nu)-4(1+2\nu)}\left(1 - \frac{4^{1+\frac{1}{\nu}}}{3^{1+\frac{1}{\nu}}}\,e^{-\frac{3cz^2}{4}}\right) \\ & - \frac{\mu^2 c\nu z_h^{2+\frac{2}{\nu}}e^{\frac{cz_h^2}{2}}}{\left(1-e^{\frac{cz_h^2}{4}}\right)^2}\left(1 - e^{-cz^2} - 4\,\frac{cz_h^2(1+\nu)-(1+2\nu)}{3cz_h^2(1+\nu)-4(1+2\nu)}\left(1 - \frac{4^{1+\frac{1}{\nu}}}{3^{1+\frac{1}{\nu}}}\,e^{-\frac{3cz^2}{4}}\right)\right)\Bigg\} \\ & - \frac{z^{4+\frac{2}{\nu}}}{z_h^{2+\frac{2}{\nu}}}\Bigg\{\frac{12c(1+3\nu(1+\nu))}{3cz_h^2(1+\nu)-4(1+2\nu)} + \frac{\mu^2c^2\nu z_h^{2+\frac{2}{\nu}}e^{\frac{cz_h^2}{2}}}{4\left(1-e^{\frac{cz_h^2}{4}}\right)^2}\,\frac{3c\nu z_h^2+4(1+2\nu)}{3cz_h^2(1+\nu)-4(1+2\nu)}\Bigg\} \\ & + \frac{z^{6+\frac{2}{\nu}}}{z_h^{2+\frac{2}{\nu}}}\,\frac{9c^2\nu(1+\nu)}{3cz_h^2(1+\nu)-4(1+2\nu)}\left(1 + \frac{\mu^2c\nu z_h^{2+\frac{2}{\nu}}e^{\frac{cz_h^2}{2}}}{12\left(1-e^{\frac{cz_h^2}{4}}\right)^2(1+\nu)}\right)\Bigg] \end{aligned} \tag{2.54}$$

and at the horizon

$$f_{2\ approx}(z_h) = \frac{1-\nu}{q^2\nu^2}\, z_h^{-\frac{4}{\nu}} e^{-\frac{cz_h^2}{4}} \left\{ \frac{4^{3+\frac{1}{\nu}}}{3^{1+\frac{1}{\nu}}} \frac{(1+\nu)(1+2\nu)}{3cz_h^2(1+\nu)-4(1+2\nu)} \right. \tag{2.55}$$
$$\left. - \frac{\mu^2 c\nu z_h^{2+\frac{2}{\nu}} e^{\frac{cz_h^2}{4}}}{\left(1-e^{\frac{cz_h^2}{4}}\right)^2} \left(1 - \frac{4^{2+\frac{1}{\nu}}}{3^{1+\frac{1}{\nu}}} \frac{cz_h^2(1+\nu)-(1+2\nu)}{3cz_h^2(1+\nu)-4(1+2\nu)}\, e^{\frac{cz^2}{4}}\right) \right\}.$$

If we substitute $g_{appr}(z)$ into f_2, the result coincides with (2.54).

2.3.3 Scalar Field

Substitution of (2.31) into (2.6) leads to

$$\phi' = \frac{1}{\nu z}\sqrt{\frac{3}{2}\,\nu^2 c^2 z^4 - 9\nu^2 c z^2 + 4\nu - 4}. \tag{2.56}$$

Here we should take into account, that the radicand in (2.56) shouldn't be negative. Therefore we have different cases of parameter c value.

- **$c < 0$**

For $c < 0$ this requirement is fullfiled without any restrictions and for the scalar field we have

$$\phi = \frac{1}{2\sqrt{2}\,\nu}\left\{ \sqrt{3c^2\nu^2 z^4 - 18c\,\nu^2 z^2 + 8\,(\nu-1)} - \sqrt{3c^2\nu^2 z_h^4 - 18c\,\nu^2 z_h^2 + 8\,(\nu-1)} \right. \tag{2.57}$$
$$+\ 2\sqrt{2\,(\nu-1)}\ln\left(\frac{z^2}{z_h^2}\right) - 3\sqrt{3}\,\nu\ln\left(\frac{\sqrt{3c^2\nu^2 z^4 - 18c\,\nu^2 z^2 + 8\,(\nu-1)} - \sqrt{3}\,\nu\,(3-cz^2)}{\sqrt{3c^2\nu^2 z_h^4 - 18c\,\nu^2 z_h^2 + 8\,(\nu-1)} - \sqrt{3}\,\nu\,(3-cz_h^2)}\right)$$
$$\left. -\ 2\sqrt{2\,(\nu-1)}\ln\left(\frac{9c\,\nu^2 z^2 - 8\,(\nu-1) - \sqrt{2\,(\nu-1)}\,\sqrt{3c^2\nu^2 z^4 - 18c\,\nu^2 z^2 + 8\,(\nu-1)}}{9c\,\nu^2 z_h^2 - 8\,(\nu-1) - \sqrt{2\,(\nu-1)}\,\sqrt{3c^2\nu^2 z_h^4 - 18c\,\nu^2 z_h^2 + 8\,(\nu-1)}}\right)\right\}.$$

For small z the scalar field can be approximated as

$$\phi \sim -\,k(z_h,\nu,c) + \frac{2\sqrt{\nu-1}}{\nu}\log\left(\frac{z}{z_h}\right) \tag{2.58}$$

and for large z

$$\phi \sim \frac{|c|}{2}\sqrt{\frac{3}{2}}\,z^2. \tag{2.59}$$

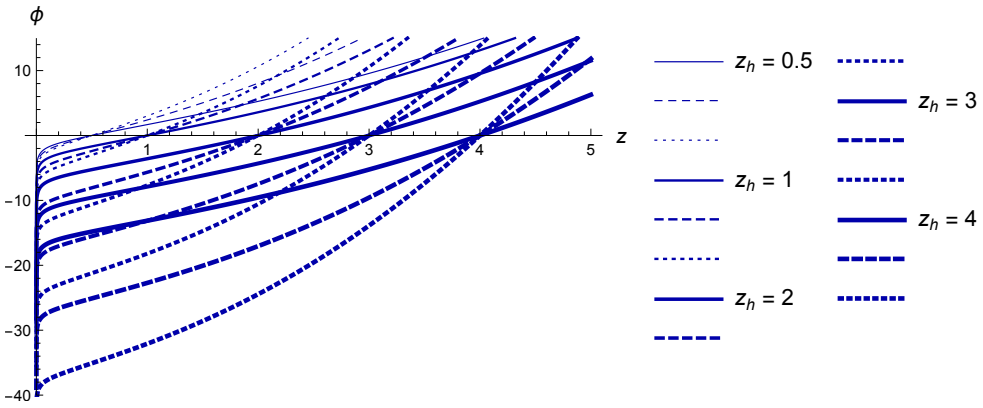


Figure 3. Scalar field $\phi(z)$ for $\nu = 4.5$, $c = -1$ (solid lines), $c = -2$ (dashed lines) and $c = -3$ (dotted lines) and different z_h.

- **c > 0**

For $c > 0$ expression (2.56) can be parametrized as

$$\phi' = \frac{c}{z}\sqrt{\frac{3}{2}\,(\alpha^2 - z^2)(\beta^2 - z^2)}, \tag{2.60}$$

where

$$\alpha^2\beta^2 = \frac{8(\nu-1)}{3\nu^2 c^2}, \qquad \alpha^2 + \beta^2 = \frac{6}{c}, \tag{2.61}$$

and

$$\alpha = \sqrt{\frac{3}{c} - \frac{1}{c}\sqrt{9 - \frac{8(\nu-1)}{3\nu^2}}}, \qquad \beta = \sqrt{\frac{3}{c} + \frac{1}{c}\sqrt{9 - \frac{8(\nu-1)}{3\nu^2}}}. \tag{2.62}$$

Note, that we can get a real solution only for

$$i) \quad \alpha^2 - z^2 > 0, \quad \beta^2 - z^2 > 0, \tag{2.63}$$

$$ii) \quad \alpha^2 - z^2 < 0, \quad \beta^2 - z^2 < 0. \tag{2.64}$$

Integrating (2.60) we obtain

$$\phi(z) = \sqrt{\frac{3}{8}}\,c\left\{\sqrt{(\alpha^2 - z^2)(\beta^2 - z^2)} - \sqrt{(\alpha^2 - z_h^2)(\beta^2 - z_h^2)} + \alpha\beta\ln\left(\frac{z^2}{z_h^2}\right)\right.$$
$$\left. - \frac{\alpha^2+\beta^2}{2}\ln\left(\frac{\sqrt{(\alpha^2 - z^2)(\beta^2 - z^2)} + z^2 - \frac{\alpha^2+\beta^2}{2}}{\sqrt{(\alpha^2 - z_h^2)(\beta^2 - z_h^2)} + z_h^2 - \frac{\alpha^2+\beta^2}{2}}\right)\right. \tag{2.65}$$

$$- \alpha\beta \ln \left(\frac{\alpha^2\beta^2 - \frac{\alpha^2+\beta^2}{2} z^2 + \alpha\beta\sqrt{(\alpha^2 - z^2)(\beta^2 - z^2)}}{\alpha^2\beta^2 - \frac{\alpha^2+\beta^2}{2} z_h^2 + \alpha\beta\sqrt{(\alpha^2 - z_h^2)(\beta^2 - z_h^2)}} \right) \Bigg\}$$

We see that the solution (B.21) becomes complex for $\alpha < z < \beta$. It leads to an instability region for the scalar field.

- **c = 0**

For $c = 0$ we get

$$\phi' = \frac{2\sqrt{\nu - 1}}{\nu z}, \tag{2.66}$$

$$\phi = \frac{2\sqrt{\nu - 1}}{\nu} \ln\left(\frac{z}{z_h}\right). \tag{2.67}$$

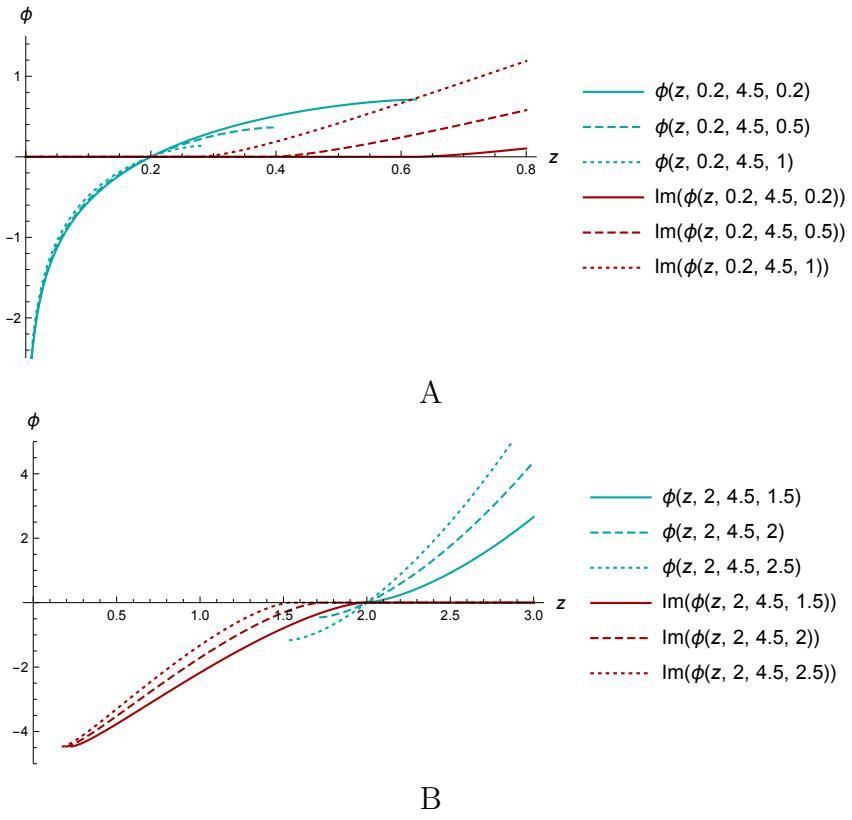


Figure 4. Scalar field $\phi(z, z_h, \nu, c)$ and its imaginary part for $\nu = 4.5$, different positive c, $z_h = 0.2$ (A) and $z_h = 2$ (B).

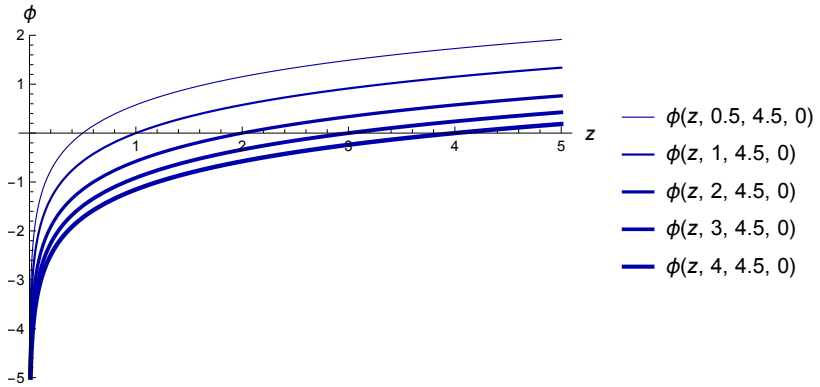


Figure 5. Scalar field $\phi(z,\, z_h,\, \nu,\, c)$ for $\nu = 4.5$, $c = 0$ and different z_h.

2.3.4 Scalar potential

From equation (2.8) we get the expression for the scalar potential V as a function of z:

$$
\begin{aligned}
V(z) = \frac{e^{-\frac{cz^2}{2}}}{8\nu^2}\Big\{ & -16\left(2\nu^2+3\nu+1\right) + 12c\,\nu\, z^2\,(2\nu+3) + 16\left(2\nu^2+3\nu+1\right) z^{2+\frac{2}{\nu}}\,\mathfrak{V} \\
& - 16\nu\,(2\nu+1)\,\frac{z^{2+\frac{2}{\nu}}}{z_h^{2+\frac{2}{\nu}}}\,e^{-cz^2}\left[\frac{e^{\frac{cz^2}{4}}}{\mathfrak{G}(\frac{3}{4}cz_h^2)} + \frac{\mu^2 c\, z_h^{2+\frac{2}{\nu}} e^{\frac{cz_h^2}{2}}}{4\left(1-e^{\frac{cz_h^2}{4}}\right)^2}\left(1 - e^{\frac{cz^2}{4}}\,\frac{\mathfrak{G}(cz_h^2)}{\mathfrak{G}(\frac{3}{4}cz_h^2)}\right)\right] \\
& - 18c^2\nu^2 z^4 - 12c\nu\,(2\nu+3)\,z^{4+\frac{2}{\nu}}\,\mathfrak{V} \\
& - \nu\,\frac{z^{4+\frac{2}{\nu}}}{z_h^{2+\frac{2}{\nu}}}\,e^{-cz^2}\left[\frac{-24c\,\nu\,e^{\frac{cz^2}{4}}}{\mathfrak{G}(\frac{3}{4}cz_h^2)} - \frac{5\mu^2c^2\nu\, z_h^{2+\frac{2}{\nu}} e^{\frac{cz_h^2}{2}}}{\left(1-e^{\frac{cz_h^2}{4}}\right)^2}\left(1 - \frac{6}{5}e^{\frac{cz^2}{4}}\,\frac{\mathfrak{G}(cz_h^2)}{\mathfrak{G}(\frac{3}{4}cz_h^2)}\right)\right] \\
& + 18c^2\nu^2 z^{6+\frac{2}{\nu}}\,\mathfrak{V}\Big\}\,,
\end{aligned}
\tag{2.68}
$$

where

$$
\mathfrak{V} = \frac{1}{z_h^{2+\frac{2}{\nu}}}\,\frac{\mathfrak{G}(\frac{3}{4}cz^2)}{\mathfrak{G}(\frac{3}{4}cz_h^2)} + \frac{\mu^2 c\, e^{\frac{cz_h^2}{2}}}{4\left(1-e^{\frac{cz_h^2}{4}}\right)^2}\left(\mathfrak{G}(cz^2) - \mathfrak{G}(cz_h^2)\,\frac{\mathfrak{G}(\frac{3}{4}cz^2)}{\mathfrak{G}(\frac{3}{4}cz_h^2)}\right). \tag{2.69}
$$

The dependence $V(\phi)$ can't be expressed explicitly due to nontrivial behavior of $\phi(z)$ (2.57), but it can be displayed graphically (Fig.6). For $c = -1$ it can be approximated by a sum of two exponents and a negative constant:

$$
V_{2EA}(\phi,\mu,\nu) = V_0(\nu) - C_7(\mu,\nu)e^{K_1(\nu)\phi} + C_8(\mu,\nu)e^{K_2(\nu)\phi}. \tag{2.70}
$$

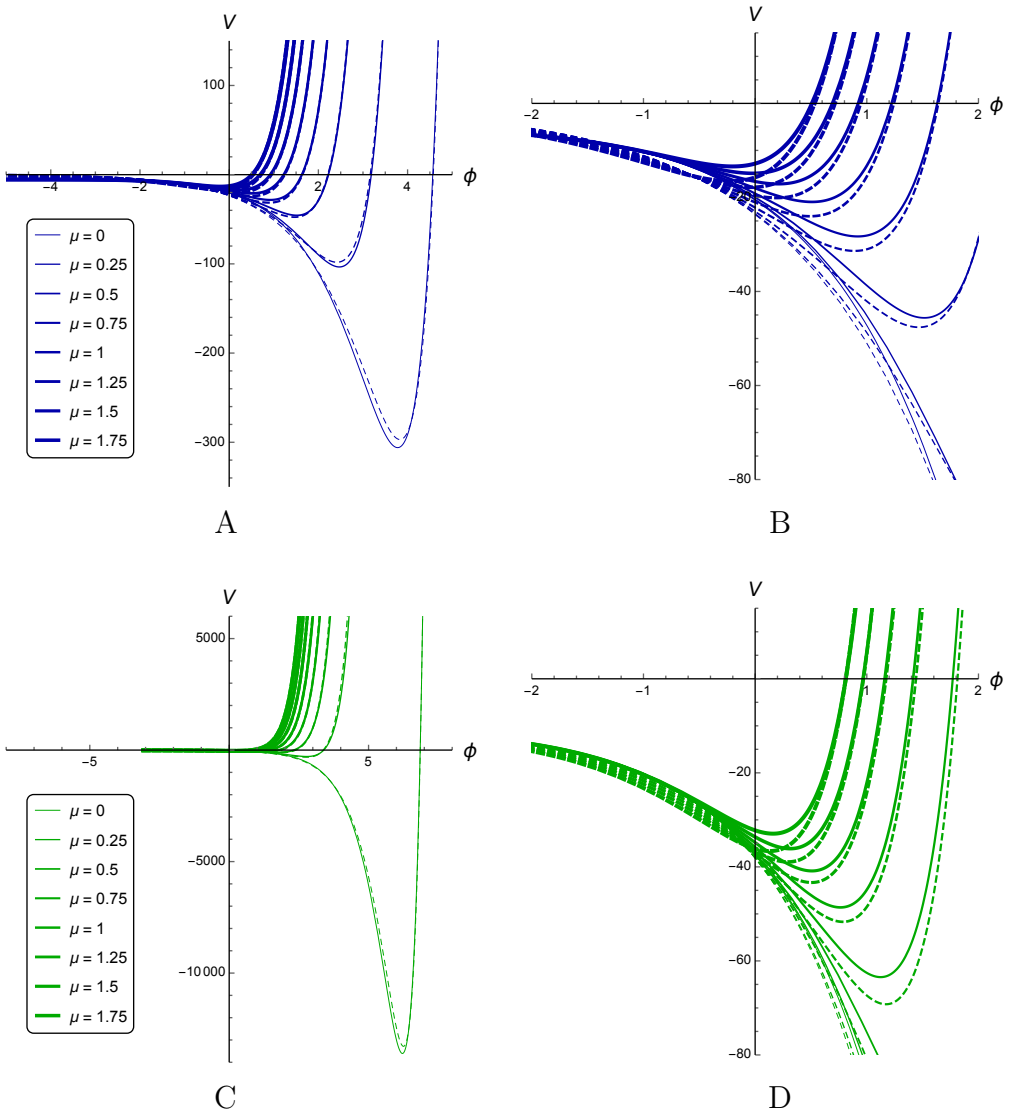


Figure 6. Scalar field potential $V(\phi)$ (solid lines) and its approximation (dashed lines) as a sum of two exponents and a constant for $z_h = 1$, $c = -1$ and different μ in anisotropic, $\nu = 4.5$, (A) and isotropic (C) cases. The right plots (B) and (D) are zoom of the corresponding left ones.

The best fit is given by

$$V_0(4.5) = -0.5778, \quad K_1(4.5) = 0.7897, \quad K_2(4.5) = 2.0995 \tag{2.71}$$

with the coefficients depending on the chemical potential μ (Fig.6.A and B):

$$C_7(\mu, 4.5) = 23.0779 + 2.4236\mu^2, \quad C_8(\mu, 4.5) = 0.0575 + 4.9919\mu^2. \tag{2.72}$$

In isotropic case (Fig.6.C and D) the approximation constants are:

$$V_0(1) = -10.8689, \quad K_1(1) = 1.0852, \quad K_2(1) = 2.4103, \tag{2.73}$$

$$C_7(\mu, 1) = 27.2825 + 4.3749\mu^2, \quad C_8(\mu, 1) = 0.0031 + 5.03093\mu^2. \tag{2.74}$$

Note, that in [57] an explicit isotropic solution for the dilaton potential as a sum of two exponents and zero chemical potential has been constructed. It would be interesting to generalize this construction to the anisotropic and non-zero chemical potential cases.

The behavior of $V(\phi)$ for positive warp factor coefficient is quite different. Let us recall that for $c > 0$ the scalar field ϕ becomes complex under horizon (Fig.7). The function $V(\mathrm{Re}(\phi))$ doesn't display visible dependence on chemical potential (Fig.8.A) and the function $V(|\phi|)$ stops to depend on μ rather soon (Fig.8.B).

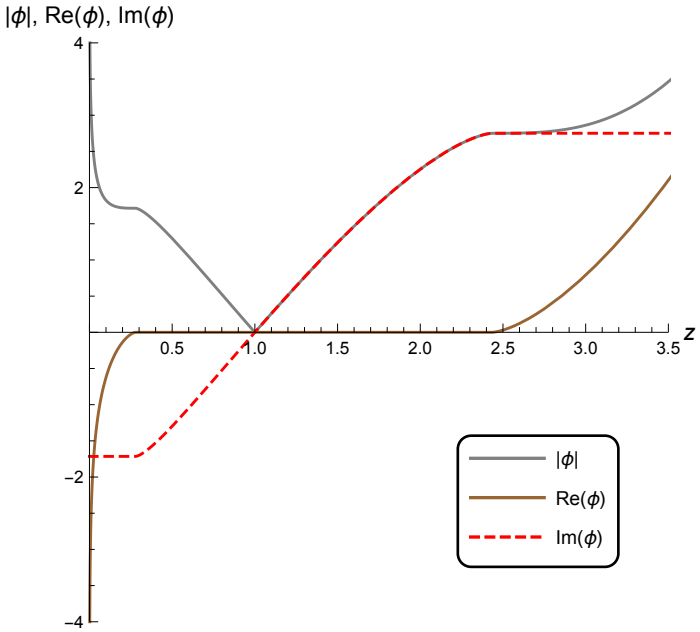
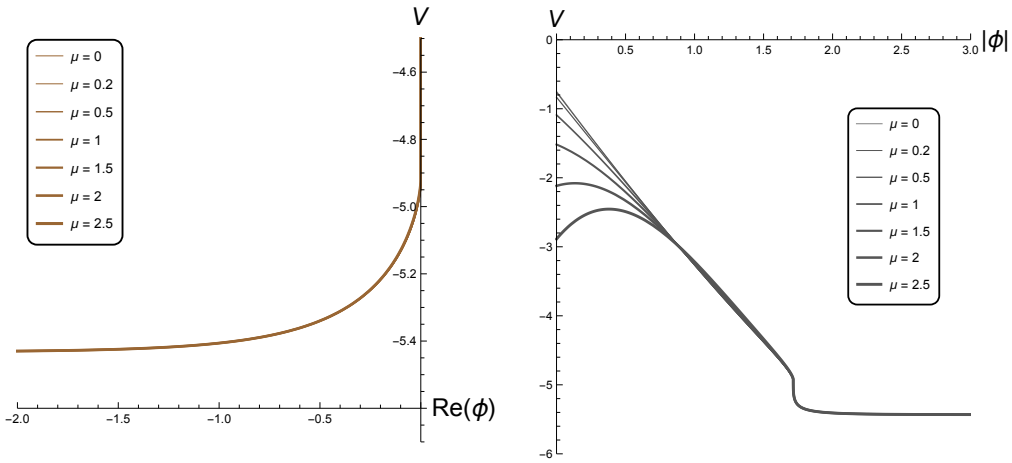


Figure 7. Module, real and imaginary parts of the scalar field ϕ for $\nu = 4.5$, $z_h = 1$, $c = 1$.



A B

Figure 8. Scalar potential $V\big(\mathrm{Re}(\phi)\big)$ (A) and $V(|\phi|)$ (B) for $\nu = 4.5$, $z_h = 1$, $c = 1$ and different μ under horizon, i.e. $0 < z < 1$.

2.4 Scalar invariants

For completeness we present here the dependence of the scalar invariants R, $R^2 = R_{\mu\nu}R^{\mu\nu}$ and $K = R_{\mu\nu\rho\sigma}R^{\mu\nu\rho\sigma}$ on the parameter μ for the unit horizon and negative warp factor coefficient c. All the invariants are smooth inside the black hole and start to diverge for $z > z_h$ (Fig.9, 10). In isotropic case it happens earlier, means for smaller z, than is anisotropic one. Thus the horizons of the blackening function, depicted on Fig.1, are regular.

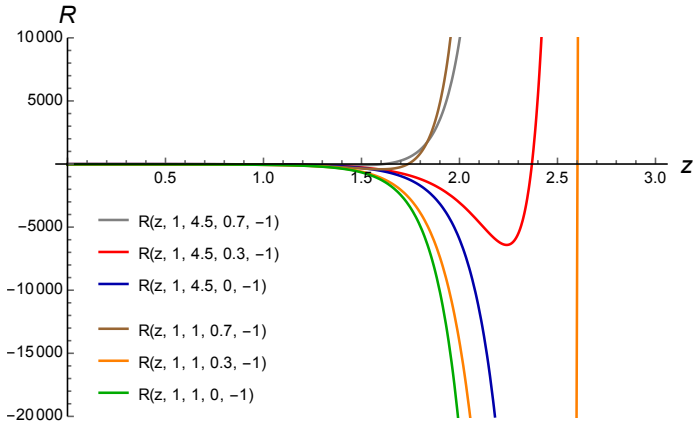


Figure 9. Ricci scalar $R(z)$ for $z_h = 1$, $c = -1$ in isotropic, $\nu = 1$, and anisotropic, $\nu = 4.5$, cases for different μ.

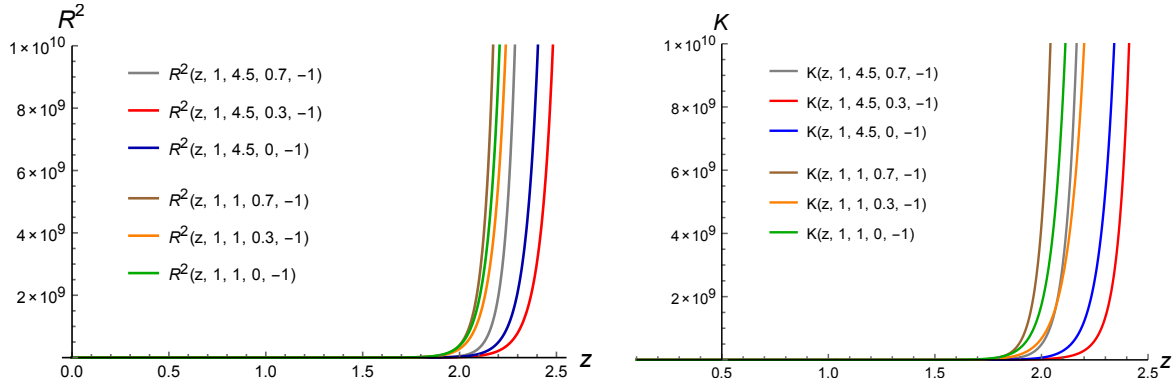


Figure 10. Ricci $R^2(z)$ and Riemann $K(z)$ invariants for $z_h = 1$, $c = -1$ in isotropic, $\nu = 1$, and anisotropic, $\nu = 4.5$, cases for different μ.

2.5 RG flow

Our background is an anisotropic analog of the background used in the improved holographic QCD model [22]. The holographic coordinate z corresponds to the 4D RG scale. According to holographic dictionary one identifies the 4D energy scale E with the metric scalar factor, i.e. $E = E_0\, L\, \sqrt{b(z)}/z \equiv E_0 L B(z)$, in what follows we put $E_0 L = 1$. The running 't Hooft coupling λ_t is identified with the string coupling $\lambda = e^{\phi}$ up to a factor, $\lambda = \kappa\lambda_t$. In Fig.11.A we show the dependence of coupling constant on the energy parameter for isotropic and anisotpopic cases. We see that the running coupling constant decreases from the IR region to the UV region. This behavior reproduces our expectations of the running coupling view in a nonperturbative QCD. Note, that the anisotropic case does not differ much from the isotropic one. The difference becomes more essential for small z_h.

The β-function in terms of the background is defined as [5, 58]

$$\beta(\lambda) = \frac{d\lambda}{d\log E} = \lambda\,\frac{d\phi}{d\log B}, \qquad B = \frac{\sqrt{b(z)}}{z}. \tag{2.75}$$

Introducing the function X, related with the β-function as

$$X(\phi) = \frac{\beta(\lambda)}{3\lambda}, \tag{2.76}$$

the function Y, related with the blackening function as

$$Y(\phi) = \frac{1}{4}\frac{g'}{g}\frac{B}{B'}, \tag{2.77}$$

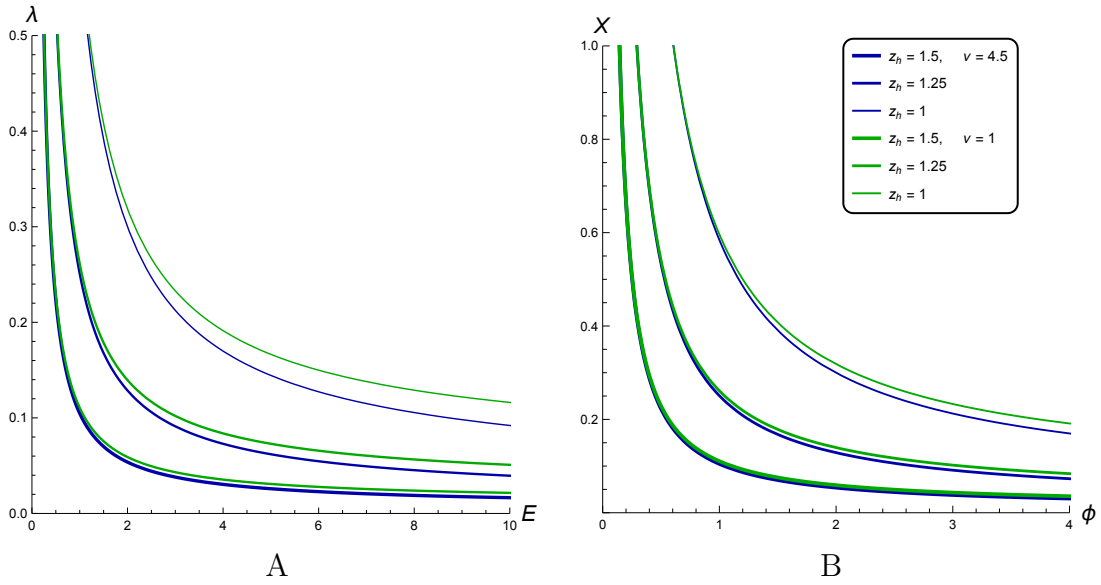


Figure 11. The running coupling as function of the energy scale (A) and the RG flow (B) in isotropic and anisotropic $\nu = 4.5$ case; the plot legends are the same for both panels.

and the function H, related with the vector field provided by non-zero chemical potential as

$$H(\phi) = \frac{A_t'}{B}, \tag{2.78}$$

one can check that in the isotropic case due to E.O.M. these quantities satisfy the first order differential equations

$$\frac{dX}{d\phi} = -\frac{4}{3}\left(1 - \frac{3}{8}X^2 + Y\right)\left(1 + \frac{1}{X}\,\frac{2\partial_\phi V - H^2\,\partial_\phi f_1}{2V + H^2 f_1}\right), \tag{2.79}$$

$$\frac{dY}{d\phi} = -\frac{4Y}{3X}\left(1 - \frac{3}{8}X^2 + Y\right)\left(1 + \frac{3}{2Y}\,\frac{H^2 f_1}{2V + H^2 f_1}\right), \tag{2.80}$$

$$\frac{dH}{d\phi} = -\left(\frac{1}{X} + \frac{\partial_\phi f_1}{f_1}\right)H, \tag{2.81}$$

where $\partial_\phi = \partial/\partial\phi$. The anisotropic case is more subtle and will be the subject of a forthcoming paper.

Fig.12 shows the X-flow in the anisotropic case for $\nu = 4.5$ and different z_h in the (ϕ, X)- and in the (λ, X)-planes. The function $X(\phi)$ decreases starting from a constant value up to a local minimum as the argument grows and is shifted to the right for larger

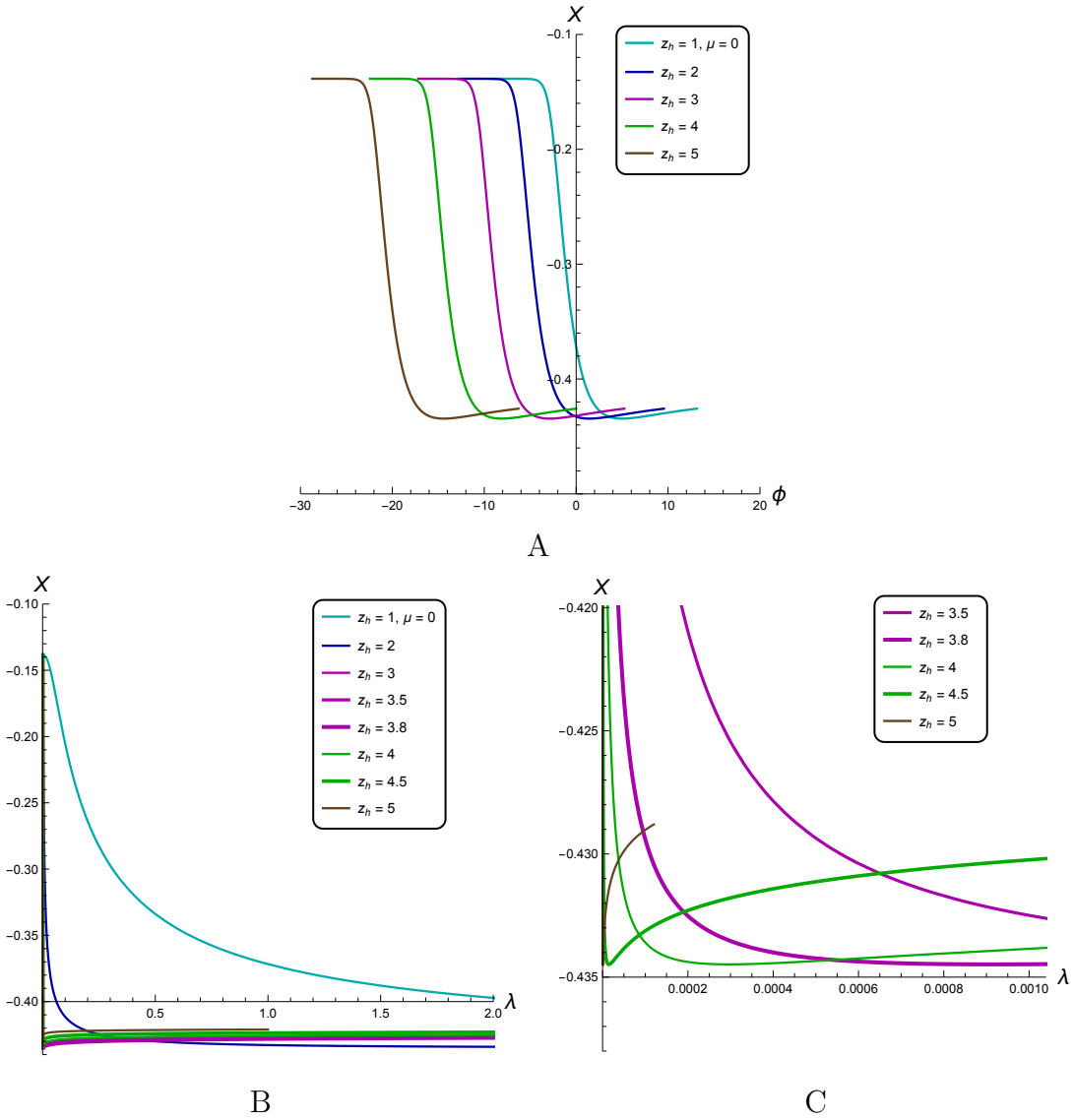


Figure 12. The RG flows for anisotropic case $\nu = 4.5$ and different z_h in the (ϕ, X)-plane (A), in the (λ, X)-plane (B) and in a small part of (B) near the origin (C).

horizon. The function $X(\lambda)$ for $z_h < 4$ smoothly decreases with increasing λ and for $z_h > 4$ the dependence is more complicated.

In Fig.13 the behavior of functions $\beta(\lambda)$ in anisotropic, $\nu = 4.5$, (Fig.13.A) and isotropic (Fig.13.C) cases and the corresponding potentials $V(\phi)$ (Fig.13.B and D) for the same horizon values are shown. We see, that for both cases $\beta(\lambda) < 0$ in an agreement with the asymptotical freedom. For larger z_h both functions display more non-linearity and decrease faster with the argument grow. This tendency is peculiar

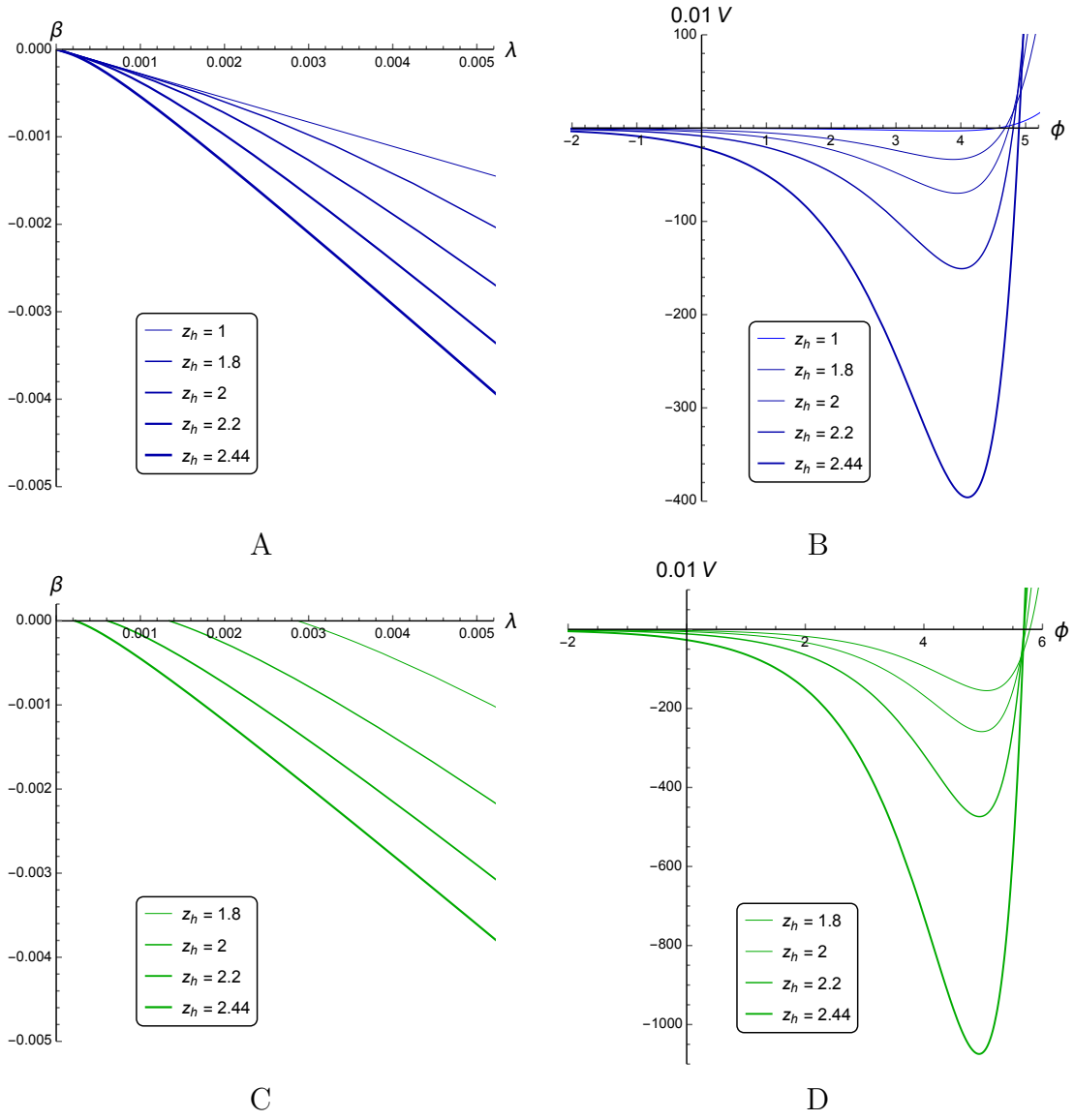


Figure 13. The function $\beta(\lambda)$ in anisotropic, $\nu = 4.5$, (A) and isotropic, $\nu = 1$, (C) cases near small λ; scalar potentials $V(\phi)$ for $\mu = 0$ in anisotropic, $\nu = 4.5$, (B) and isotropic, $\nu = 1$, (D) cases.

either for the isotropic or the anisotropic case. The only special difference is the non-zero value of $\beta(0)$ for $\nu = 1$. We expect that changing the form of $P(z)$ we can, as in the isotropic case [5, 40, 58], to recover the first orders expression of the perturbative β-function.

In Fig.14 we show the dependence of the β-function on H for the isotropic and anisotropic ($\nu = 4.5$) cases. We see that β is the increasing function of H, approxi-

mately linear for large negative argument values and displaying its non-linearity near zero. The function values are visibly larger for larger chemical potential, while the anisotropy does not change this picture much.

In Fig.15 the Y-flow is shown for anisotropic case with zero and non-zero chemical potential. The function grows rapidly and this growth does not essentially depend on the size of the horizon.

In Fig.16 we display the RG flows in the (X, Y)-plane for anisotropic case $\nu = 4.5$ and zero and non-zero chemical potential. The X and Y have the inverse ratio dependence and does not change much for different z_h.

Fig.17 shows the RG flows in the (X, Y, H)-space. We see that our anisotropy essentially changes the character of the flow.

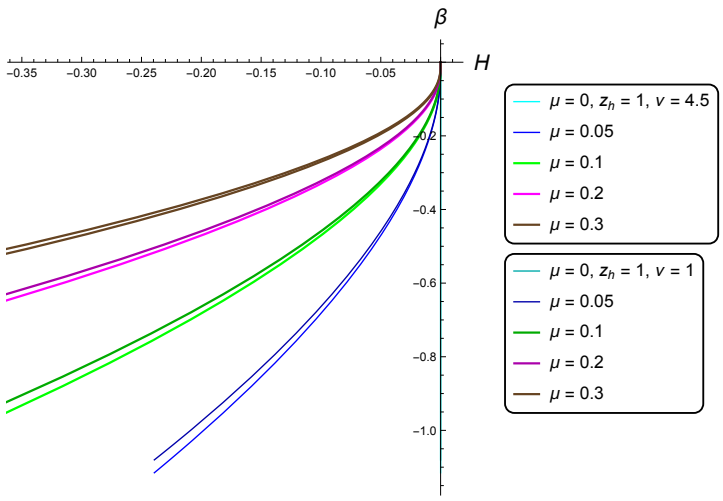


Figure 14. The function $\beta(H)$ in isotropic and anisotropic $\nu = 4.5$ cases.

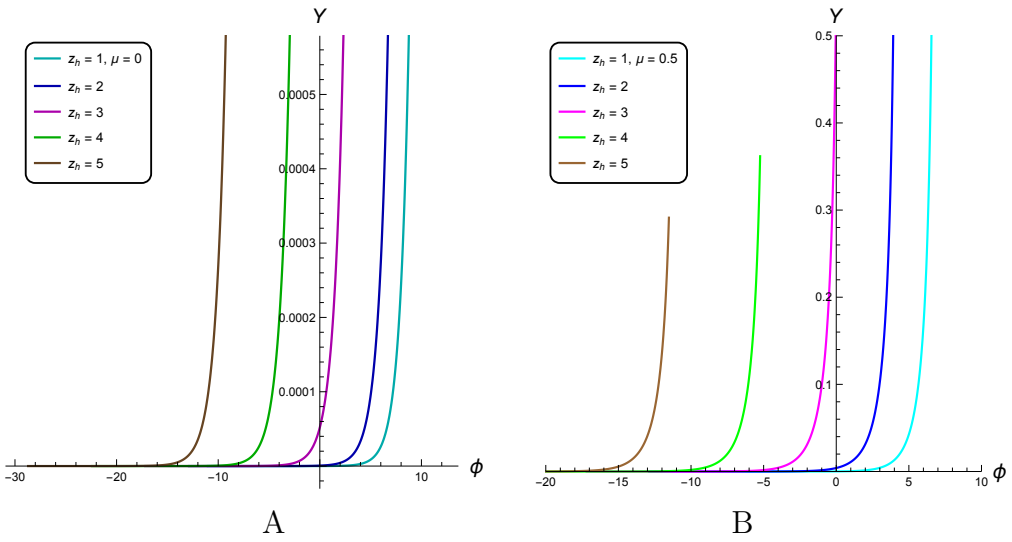


Figure 15. Y flows in anisotropic case $\nu = 4.5$ for different z_h, $\mu = 0$ (A) and $\mu = 0.5$ (B).

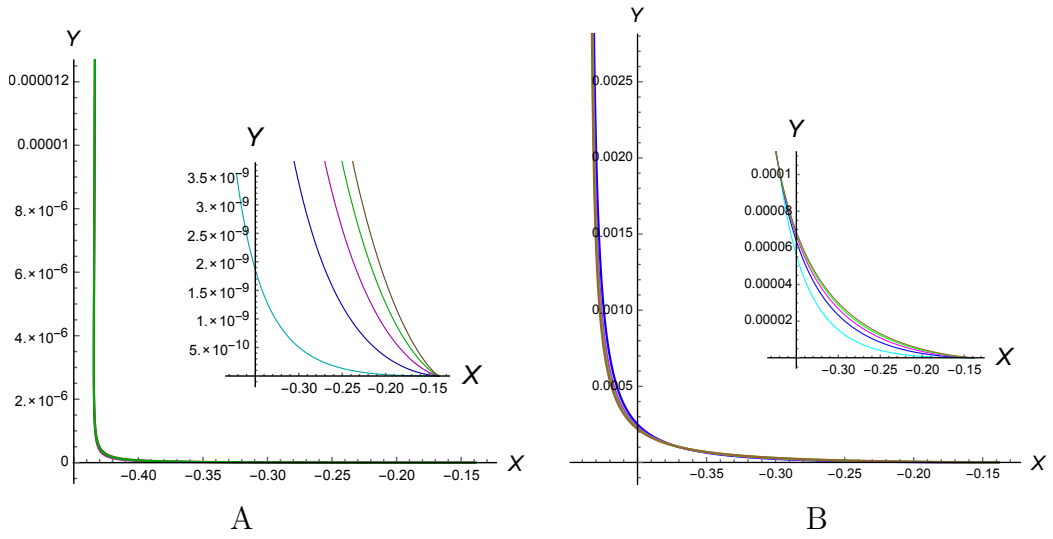


Figure 16. RG flows in the (X, Y)-plane in anisotropic case $\nu = 4.5$ for $\mu = 0$ (A) and $\mu = 0.5$ (B); the plot legends are the same as in Fig.15.

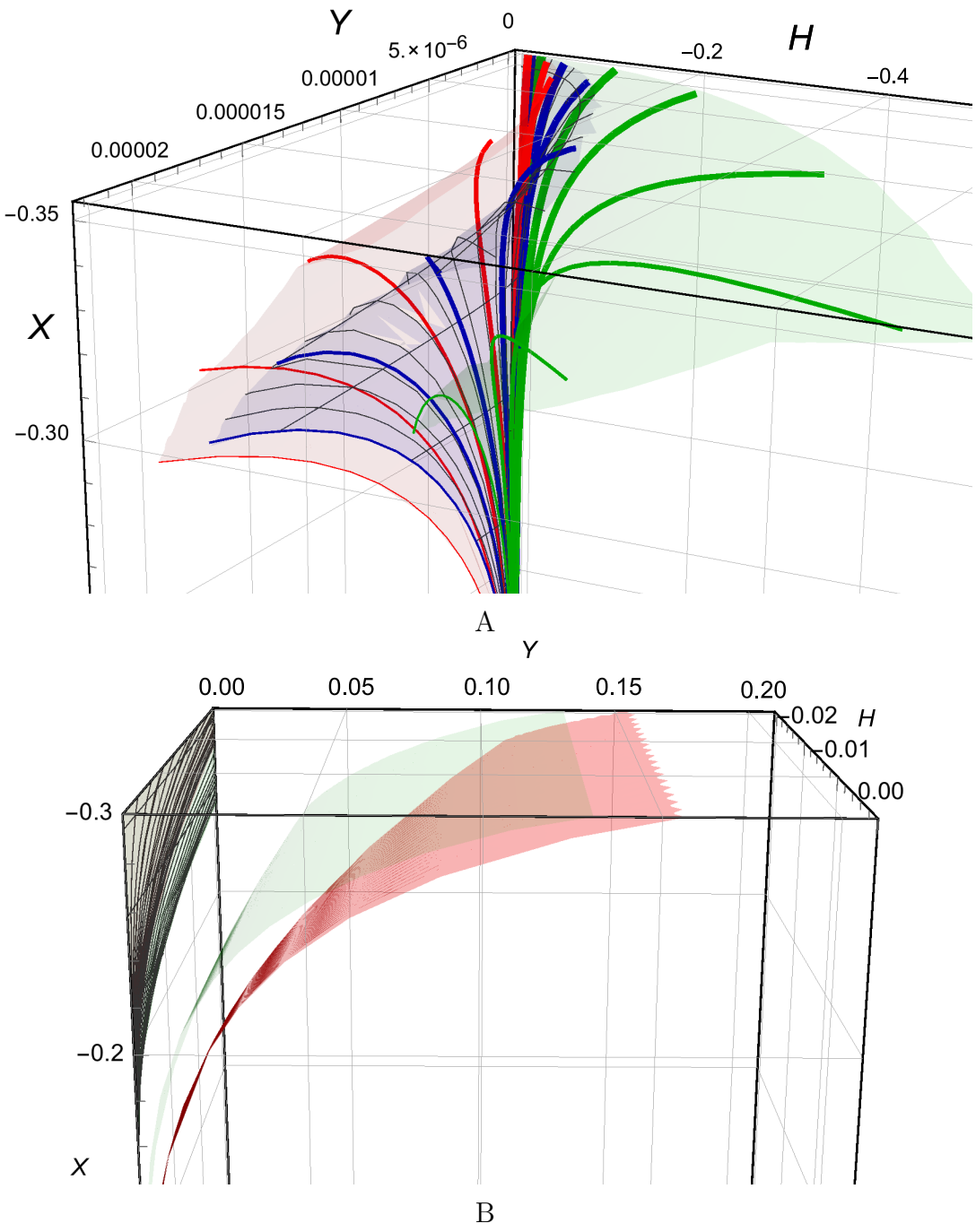


Figure 17. RG flows in the (X, Y, H)-space in anisotropic case $\nu = 4.5$ for $z_h = 2$ (light red), $z_h = 1.5$ (light blue) and $z_h = 1$ (lightgreen) (A); RG flows in the (X, Y, H)-space in anisotropic, $\nu = 4.5$, (meshed lines) and isotropic cases (not meshed lines) for $z_h = 1$ (lightgreen) and $z_h = 2$ (lightred) (B).

3 Thermodynamics of the background

3.1 Temperature

Calculating the derivative of the blackening function (2.48) at the horizon we get the temperature

$$T(z_h,\mu,c,\nu)=\frac{g'(z_h)}{4\pi}=\frac{e^{-\frac{3cz_h^2}{4}}}{2\pi z_h}\left|\frac{1}{\mathfrak{G}(\frac{3}{4}cz_h^2)}+\frac{\mu^2 cz_h^{2+\frac{2}{\nu}}e^{\frac{cz_h^2}{4}}}{4\left(1-e^{\frac{cz_h^2}{4}}\right)^2}\left(1-e^{\frac{cz_h^2}{4}}\frac{\mathfrak{G}(cz_h^2)}{\mathfrak{G}(\frac{3}{4}cz_h^2)}\right)\right| \tag{3.1}$$

Here the dependence on ν is caused by the function $\mathfrak{G}$ (2.39) in the right-hand side of (3.1). In particular, for the zero chemical potential, $\mu=0$,

$$T(z_h,c,\nu)\equiv T(z_h,0,c,\nu)=\frac{e^{-\frac{3cz_h^2}{4}}}{2\pi z_h\mathfrak{G}(\frac{3}{4}cz_h^2)}. \tag{3.2}$$

For $c=0$ it reproduces the result from [33]:

$$T(z_h,0,\nu)=\lim_{c\to 0}\frac{e^{-\frac{3cz_h^2}{4}}}{2\pi z_h\mathfrak{G}(\frac{3}{4}cz_h^2)}=\frac{1}{2\pi z_h}\frac{\nu+1}{\nu}. \tag{3.3}$$

From (3.1) we get the dependence of temperature on z_h, μ, c and ν. In Fig.18.A and Fig.18.B we present the dependence of T on z_h for different μ and fixed $c=-1$ for isotropic (Fig.18.A) and anisotropic (Fig.18.B) cases, respectively. In Fig.18.C we compare the plots, presented in Fig.18.A and Fig.18.B. Plot in Fig.18.D is a zoom of Fig.18.B. In Fig.19 we present the dependence of temperature on z_h for different $\mu=0$ and $c<0$, and in Fig.20 the dependence of temperature on μ keeping $z_h=1$ for different $c<0$ is shown. Fig.21 displays contour plots for the temperature dependence on the horizon position and chemical potential for the isotropic (A) and anisotropic (B) cases at fixed $c=-1$.

These plots show the following behavior of the temperature:

- For $\mu=0$ (dashed lines) there is one extremal point (minimum) for the temperature as a function of the horizon position; we denote the corresponding horizon z_h as $z_{h,min}(0)=z_{h,min}(0,c,\nu)$, and we get the following picture:
  - for $0<z_h<z_{h,min}(0)$ (large black holes) the temperature drops as z_h grows and for $z_{h,min}(0)<z_h$ (small black holes) the temperature increases with the growth of z_h;

- the minimal isotropic horizon $z_{min}^{(iso)}(c) \equiv z_{h,min}(0,c,1)$ is larger than the minimal anisotropic horizon $z_{min}^{(\nu)}(c) \equiv z_{min}(0,c,\nu)$, i.e. $z_{min}^{(iso)}(c) > z_{min}^{(\nu)}(c)$ and the corresponding critical temperature $T_{min}(0)$ is higher for the isotropic case, i.e. $T(z_{min}^{(iso)}(c),c,1) \equiv T_{min}^{(iso)} > T_{min}^{(\nu)} \equiv T(z_{min}^{(\nu)}(c),c,\nu)$; one can read these inequalities from the plot in Fig.18.C and D;
- for negative c with decreasing $|c|$ the temperature $T_{min}^{(iso)}$ (the brown dashed line) is below the green one and its minimum is shifted to the right from the minimum of the green one (Fig.19.A); $T_{min}^{(\nu)}$ (the cyan dashed line) is below the blue one and its minimum is shifted to the right from that of the blue one Fig.18.B);
- for $c = -1$ the values of the minimal horizons $z_{min}(\nu)$ are $z_{min}^{(iso)} = 1.547$ and $z_{min}^{(4.5)} = 1.168$ for the isotropic and anisotropic cases; the corresponding temperatures are $T_{min}^{(iso)} = 0.355$ and $T_{min}^{(4.5)} = 0.245$ (Fig.19.A and B).

- For $0 < \mu < \mu_{cr}$ there are two extremal points $z_{h,min}(\mu) = z_{h,min}(\mu,c,\nu)$ and $z_{h,max} = z_{h,max}(\mu,c,\nu)$; corresponding $T_{min}(\mu)$ and $T_{max}(\mu)$ are shown in Fig.18:
  - for $0 < z < z_{h,min}$ the temperature drops with the growth of z_h;
  - for $z_{h,min} < z < z_{h,max}$ the temperature increases with the growth of z_h;
  - for $z_{h,max} < z < z_{h_0}$ the temperature decreases again with the growth of z_h; here z_{h_0} is the position of the new horizon, $T(z_{h_0}) = 0$, $z_{h_0} = z_{h_0}(\mu,c,\nu)$;
  - μ_{cr}, $z_{h,min}$ and $z_{h,max}$ depend on the warp factor coefficient c and the anisotropic parameter ν;
  - the anisotropy increases the size of the new horizon, $z_{h_0}(\mu,c,1) < z_{h_0}(\mu,c,\nu)$.

- For $\mu = \mu_{cr}$ (dotted lines in Fig.18) there is no extremal point, but there is an inflection point $(z_{h,cr}, T_{cr})$, $z_{h,cr} = z_{h,cr}(\mu_{cr})$, $T_{cr} = T_{cr}(\mu_{cr})$, therefore
  - for all values of z_h with its growth the temperature decreases;
  - the temperature becomes equal to zero at a new horizon.

- For $\mu > \mu_{cr}$ increasing z_h we decrease the temperature and there is a point $z_{h_0} = z_{h_0}(\mu,c,\nu)$ where $T(z_{h_0}) = 0$, i.e. a new horizon appears;
  - for negative c with the growth of $|c|$ the values of $z_{h_0}(\mu,\nu)(c)$ decrease, $z_{h_0}(\mu,\nu)(c_1) < z_{h_0}(\mu,\nu)(c_2)$ for $|c_1| > |c_2|$ and all $\nu \geq 1$ (Fig.19).

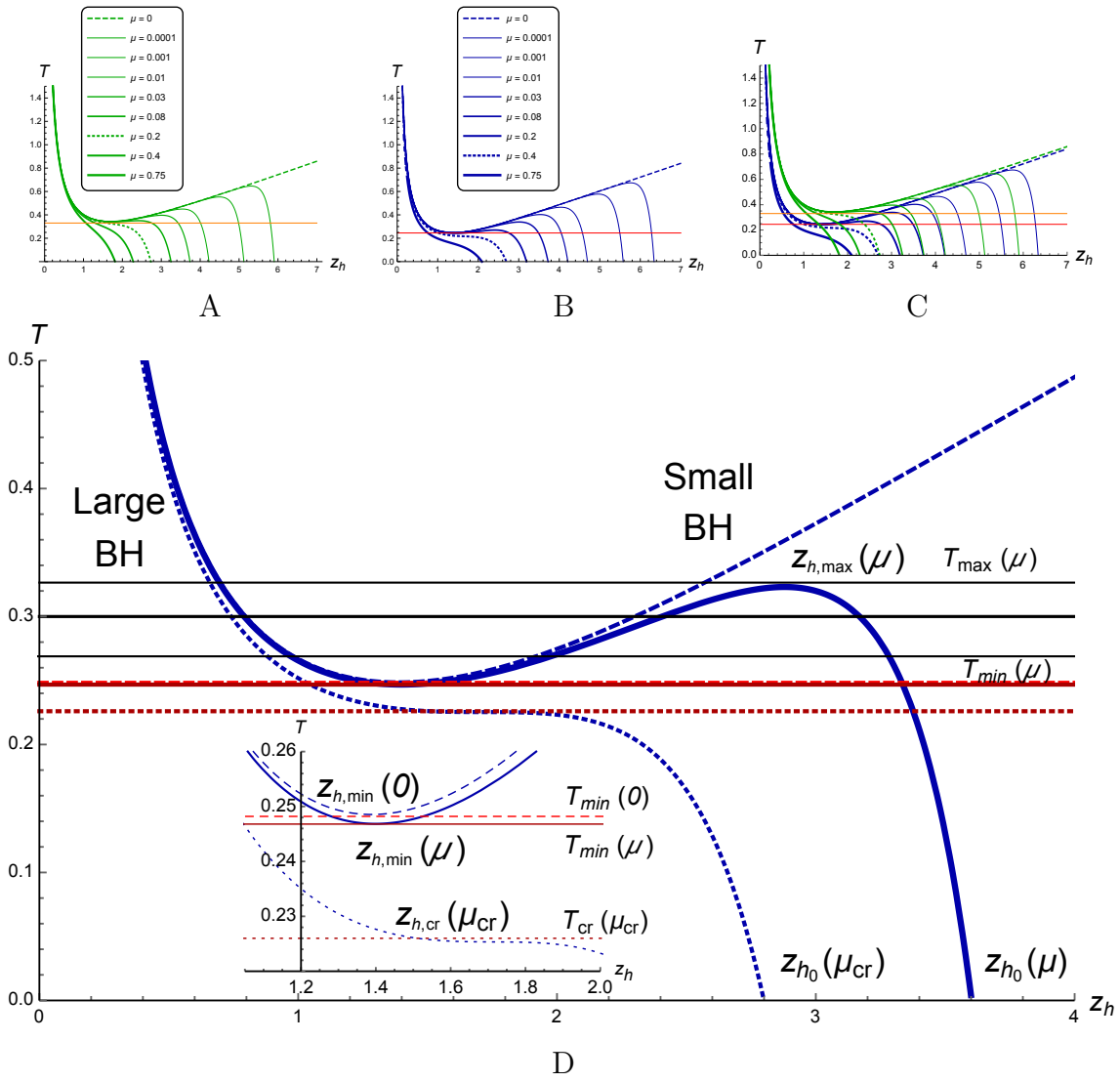


Figure 18. The dependence of temperature $T(z_h, \mu, c, \nu)$ on z_h for $c = -1$ and different μ for isotropic (A) and anisotropic, $\nu = 4.5$, (B) cases, their comparison with the same line labels (C); anisotropic case for $c = -1$ and different μ in details (D); the horizontal orange and red lines show locations of the global minima in isotropic and anisotropic cases, respectively.

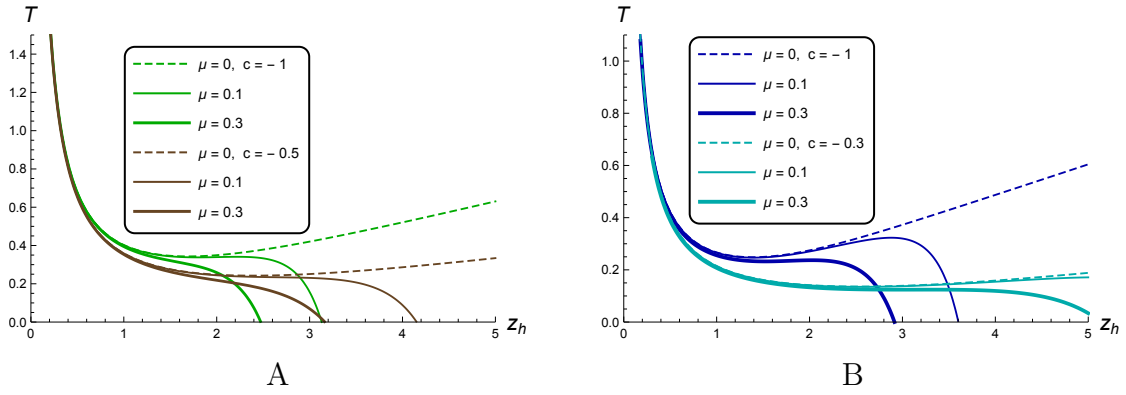


Figure 19. File: **Termo-mu-c-zh-original.nb+**. The dependence of temperature $T(z_h, \mu, c, \nu)$ on z_h for different c and μ in isotropic (A) and anisotropic, $\nu = 4.5$, (B) cases.

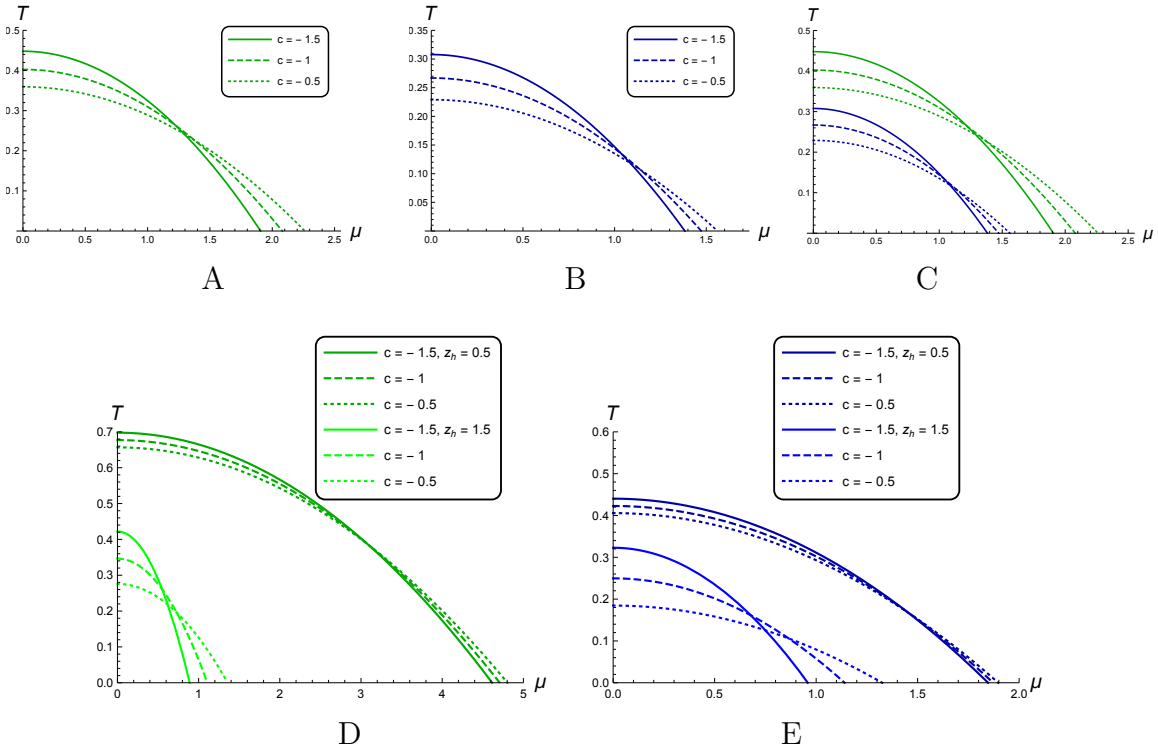


Figure 20. The dependence of temperature $T(z_h, \mu, c, \nu)$ on μ for $z_h = 1$ and different c in isotropic (A) and anisotropic, $\nu = 4.5$, (B) cases, their the comparison with the same line labels (C); for small black holes with $z_h = 1.5$ and large black holes with $z_h = 0.5$ and different c in the isotropic (D) and anisotropic, $\nu = 4.5$, (E) cases.

We can also investigate the behavior of $T(\mu)$ using expression (3.1) and taking some fixed values of the horizon. In Fig.20 we plot the curves for different negative values

of the warp factor coefficient c in isotropic (A) and anisotropic (B) cases for $z_h = 1$. In Fig.20.C we compare these cases plotting them together. Fig.20.D and E display $T(\mu)$ for large black holes with $z_h = 0.5$ and small black holes with $z_h = 1.5$. The function $T(\mu)$ decreases faster for smaller c. The isotropic case curves lie higher than the anisotropic ones and reach zero temperature at larger chemical potential values (Fig.20.C). For smaller horizons we have the same picture (Fig.20.D and E).

To summarize, note that the Van der Waals type of the temperature-horizon dependence $T(z_h)$ observed in [45, 46] for isotropic case, also takes place in the anisotropic one (see Fig.21). In both cases this behavior becomes more pronounced with decreasing of negative c, see Fig.19. The approximate solution considered in [35] does not inherit this property.

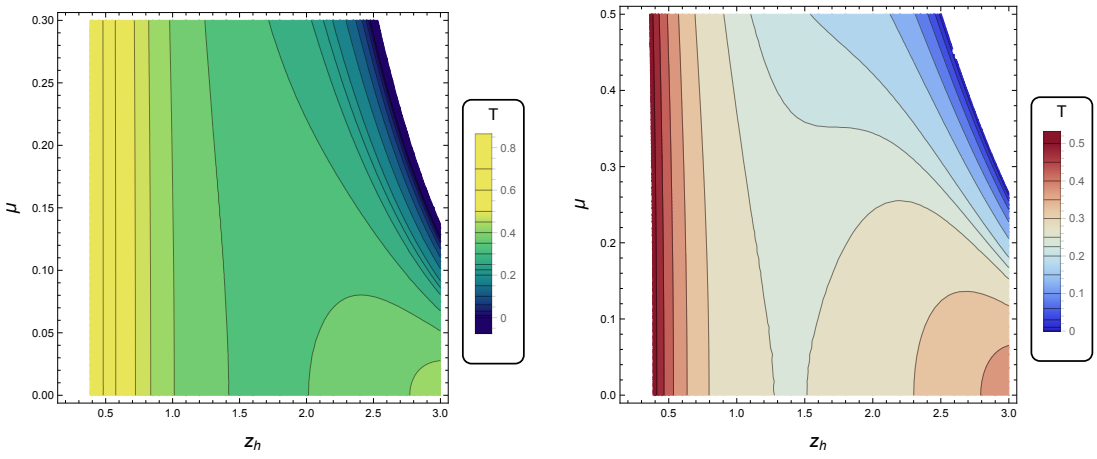


Figure 21. Contour lines of the temperature $T = T(z_h, \mu, c, \nu)$ for $c = -1$ in the isotropic (A) and anisotropic $\nu = 4.5$ (B) cases.

3.2 Entropy

The entropy is given by formula

$$s(z_h, c, \nu) = \frac{e^{\frac{3}{4}cz_h^2}}{4}\, z_h^{-\frac{(\nu+2)}{\nu}} \tag{3.4}$$

and is plotted in Fig.22.

Fig.22.A shows that the entropy is a monotonously decreasing function of the horizon z_h both for the isotropic and the anisotropic cases, in other words the entropy values are bigger for larger black holes, whose horizons are smaller. As we see from Fig.22.B, the velocity of the entropy decreasing depends on parameters c and ν. It is interesting to note that absolute value of this velocity for the same c is bigger in the isotropic case for large black holes and is smaller for small black holes. More precisely, for $c = -1$

$$s'_{z_h}(z_h, -1, 1) < s'_{z_h}(z_h, -1, 4.5) < 0 \quad \text{for} \quad z_h < 1.248, \tag{3.5}$$

$$s'_{z_h}(z_h, -1, 4.5) < s'_{z_h}(z_h, -1, 1) < 0 \quad \text{for} \quad z_h > 1.248 \tag{3.6}$$

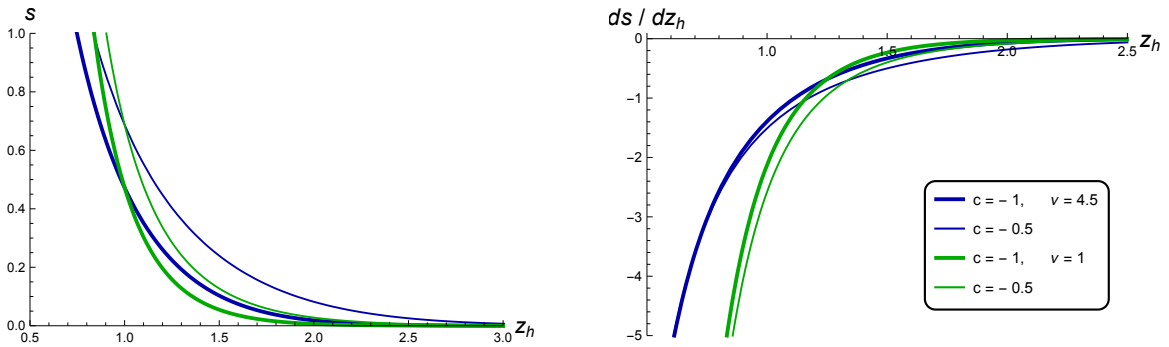
and for $c = -0.5$

$$s'_{z_h}(z_h, -0.5, 1) < s'_{z_h}(z_h, -0.5, 4.5) < 0 \quad \text{for} \quad z_h < 1.331, \tag{3.7}$$

$$s'_{z_h}(z_h, -0.5, 4.5) < s'_{z_h}(z_h, -0.5, 1) < 0 \quad \text{for} \quad z_h > 1.331. \tag{3.8}$$

Here $s'_{z_h}(z_h, c, \nu) = \partial s(z_h, c, \nu)/\partial z_h$.

In Fig.23 we present the entropy dependence on temperature T for $\mu = 0$ and different c for isotropic (green lines) and anisotropic (blue lines) cases. The plots in



A B

Figure 22. The black hole entropy $s(z_h)$ for $\mu = 0$ and different c in isotropic (green lines) and anisotropic (blue lines) (A) cases; the velocity of the entropy decreasing $\partial s(z_h)/\partial z_h$ (B); the plot legends are the same for both panels.

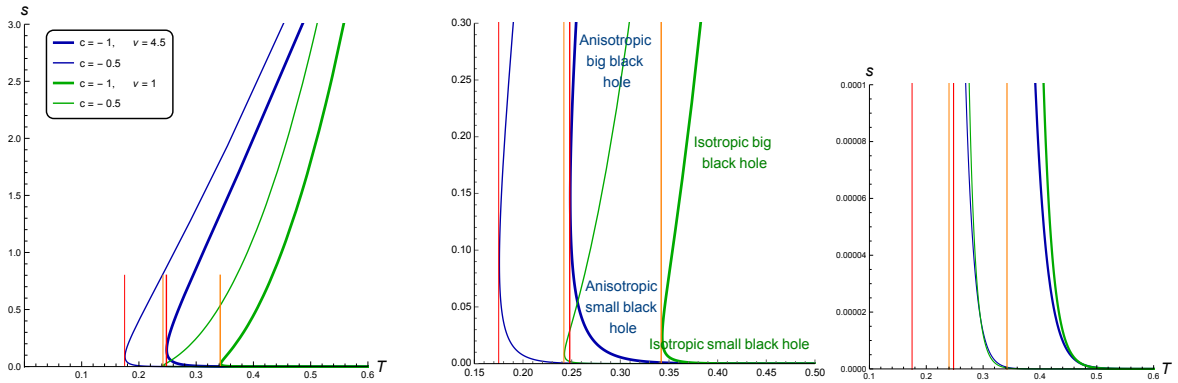


Figure 23. The black hole entropy $s(T)$ for $\mu = 0$ and different c in isotropic (green lines) and anisotropic (blue lines) cases (A); regions located near the minimum temperatures $T_{min}(c, \nu)$ with an increased scale on the right (B); the red vertical lines indicate $T_{min}(c, 4.5)$ and the orange ones indicate $T_{min}(c, 1)$ for $c = -0.5$ and $c = -1$.

Fig.23 show that in both cases there are minimal temperatures for which the black holes exist. The minimal temperature in the isotropic case is higher then in the anisotropic one for the same value of $c < 0$, $T_{min}(c, 4.5) < T_{min}(c, 1)$, that agrees with the plots in Fig.18. In both cases the entropy is a double-valued function and has a large black holes branches and a small black holes one. For the small black holes the entropy increases with decreasing T thus leading to the negativity of the specific heat $c_v = Tds/dT$. Therefore small black holes are thermodynamically unstable, whereas entropy of the large black holes grows while temperature increases and therefore large black holes are thermodynamically stable.

In Fig.24 we present the entropy dependence on temperature T for $c = -1$ and different $\mu \geq 0$ for isotropic (green lines) and anisotropic (blue lines) cases. The plots in Fig.24 show that in both cases for fixed μ, $0 \leq \mu \leq \mu_{cr}(c, \nu)$, there are minimal $T_{min}(\mu, \nu)$ and maximal $T_{max}(\mu, \nu)$ temperatures, between which the entropy is a multivalued function of T with three branches. We see well only two braches in Fig.24.A, to see the third one has to draw the picture Fig.24.B for small values of $s(T)$. The schematic picture of three branches is presented in Fig.24.C. When we decrease the temperature, the entropy decreases along the first branch ($T_{min}(\mu, \nu) < T < \infty$). Then the entropy decreases along the second branch with an increase of temperature from $T_{min}(\mu, \nu)$ to $T_{max}(\mu, \nu)$, i.e. here the black holes are unstable. Finally the entropy increases along the third branch with an increase of temperature for $0 \leq T < T_{max}(\mu, \nu)$, see also Fig.18.D. In plots Fig.25.A and Fig.25.B we show the unstable second branches as well as the transition of the three-branch solution to the unified one-branch solutions

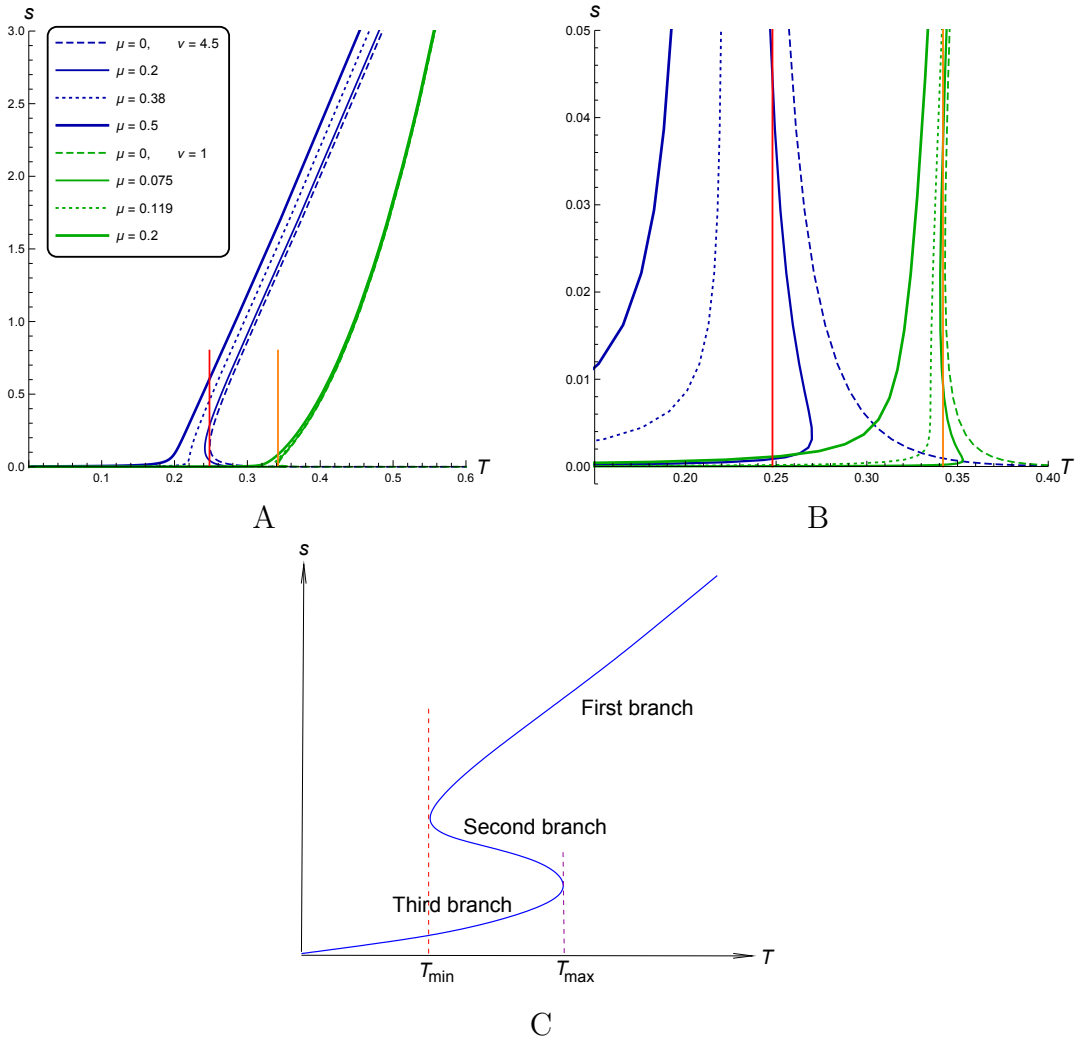


Figure 24. The black hole entropy $s(T)$ for different μ and $c = -1$ in isotropic (green lines) and anisotropic case (blue lines) (A); a region of (A), located near the minimum temperatures $T_{min}(c, \nu)$, in increased scale (B), where the red vertical line indicates $T_{min}(-1, 4.5) = 0.245$ and the orange one indicates $T_{min}(-1, 1) = 0.355$ for $\mu = 0$; the schematic view of $s(T)$ three-branches behavior (C).

at $\mu = \mu_{cr}(-1, \nu)$ (dotted green and blue lines for the isotropic and anisotropic cases). The entropy dependence on the temperature at unified branches corresponding to $\mu \geq \mu_{cr}(c, \nu)$ is presented in plots Fig.25 by lines for $\mu \geq 0.119$ in isotropic case and $\mu \geq 0.3$ in anisotropic case.

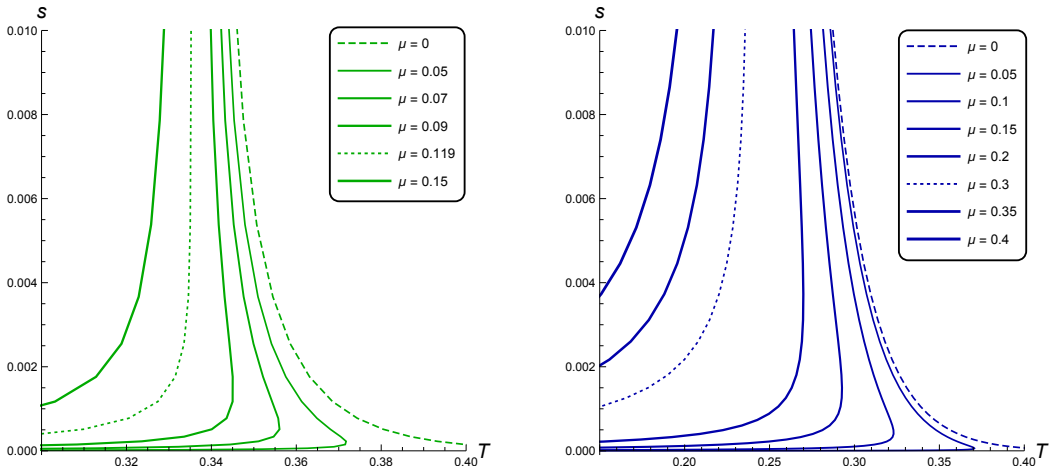


Figure 25. Unstable second branches of $s(T)$ in isotropic (A) and anisotropic case (B) cases for $c = -1$ and different μ.

3.3 Free energy

To study transitions between different branches in more detail it is reasonable to consider the free energy behavior of the corresponding solutions. The free energy for a given chemical potential and fixed volume is related to the entropy as

$$dF = -s\, dT \tag{3.9}$$

and can be found by integration of (3.9) that gives

$$F(z_h, c, \nu) = \int s\, dT = \int_{z_h}^{\infty} s(z_h, c, \nu)\, T'(z_h, c, \nu)\, dz_h. \tag{3.10}$$

The dependence of the free energy on the horizon position z_h is presented in Fig.26, the dependence on T is presented in Fig.27 and Fig.28. In Fig.26.A, which corresponds to $\mu = 0$, we can see that the free energy as the function of z_h is equal to zero at $z_h = z_{h,HP}(0, c, \nu)$, and at this point the Hawking-Page phase transition takes place. The value $z_{h,HP}(0, c, \nu)$ depends on c and ν, and $z_{h,HP}(0, c_1, \nu) < z_{h,HP}(0, c_2, \nu)$ for $c_1 < c_2 < 0$. For the anisotropic background the Hawking-Page horizon is less than for the isotropic one with the same $c < 0$. In particular,

$$1.138 = z_{h,HP}(0, -1, 4.5) < z_{h,HP}(0, -1, 1) = 1.505. \tag{3.11}$$

Note that the position of horizon, where the temperature gets its local minimum, exceed the position of the Hawking-Page horizon $z_{h,HP}(0, -1, \nu) < z_{h,min}(0, -1, \nu)$.

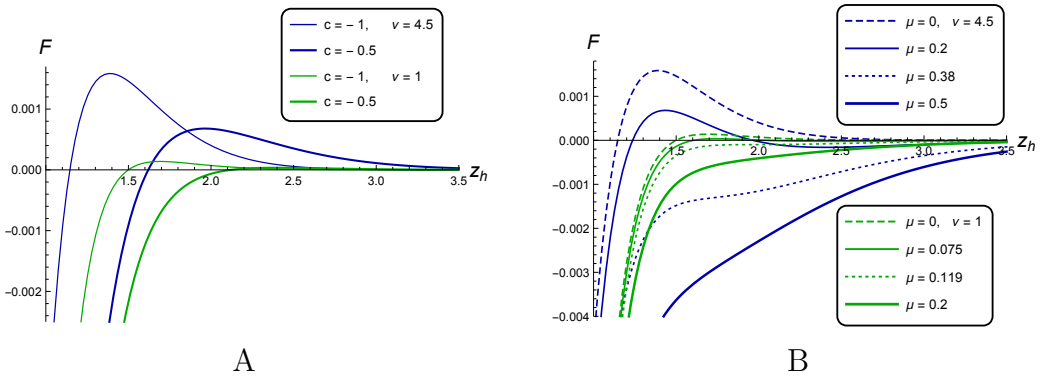


Figure 26. The black hole free energy $F(z_h)$ in isotropic (green lines) and anisotropic (blue lines) cases for different c, $\mu = 0$ (A) and different $\mu \geq 0$, $c = -1$ (B). The intersections with the horizontal axis give the values of the Hawking-Page horizons $z_{h,HP}(\mu, c, \nu)$.

As we can see from the plots in Fig.26.B, for $0 < \mu < \mu_{cr,HP}(c, \nu)$ the free energy as the function of the horizon position keeps the same behavior as for $\mu = 0$. At $\mu = \mu_{cr,HP}(c, \nu)$ the free energy becomes non-positive and for $\mu > \mu_{cr,HP}(c, \nu)$ the Hawking-Page horizon disappears. But for the chemical potential values in the interval $\mu_{cr,HP}(c, \nu) < \mu < \mu_{cr}(c, \nu)$, the free energy still is double-valued what causes the black hole to black hole phase transition (see below).

In Fig.27 and Fig.28 we show the behavior of the free energy as function of the temperature. At $\mu = 0$, as we can see in Fig.27.B and Fig.28.D, the free energy plots intersect the horizontal axis at $T_{HP}(c, \nu)$, where the Hawking-Page phase transitions take place, $T_{HP}(0, -1, 1) = 0.347$ and $T_{HP}(0, -1, 4.5) = 0.256$. At T_{HP} black holes dissolve to thermal gas states with $F_{gas} = 0$. We note that $T_{HP}(0, -1, 4.5) < T_{HP}(0, -1, 1)$, and comparing to $T_{min}(0, -1, 4.5) = 0.255$ and $T_{min}(0, -1, 1) = 0.345$ we conclude that in both isotropic and anisotropic cases,

$$0.347 = T_{HP}(0, -1, 1) > T_{min}(0, -1, 1) = 0.345 \tag{3.12}$$

$$0.256 = T_{HP}(0, -1, 4.5) > T_{min}(0, -1, 4.5) = 0.255. \tag{3.13}$$

From Fig.26 we see that for zero chemical potential the free energy increases with z_h growth for large black holes, i.e. for $z_h < z_{h_{cr}}(c, \nu)$, and decreases for small black holes.

For $0 < \mu < \mu_{cr}(c, \nu)$ the dependence of the free energy from the temperature looks like the swallow-tailed shape both in isotropic and anisotropic cases. When we decrease the temperature from very large values up to $T_{min}(\mu)$ ($T_{min}(\mu) = T_{min}(\mu, c, \nu)$, see Fig.18), the free energy riches its maximum value, then goes down to its local minimum at $T_{max}(c, \nu)$ and turns back to increase. It intersects itself at $T = T_{BB}(\mu)$,

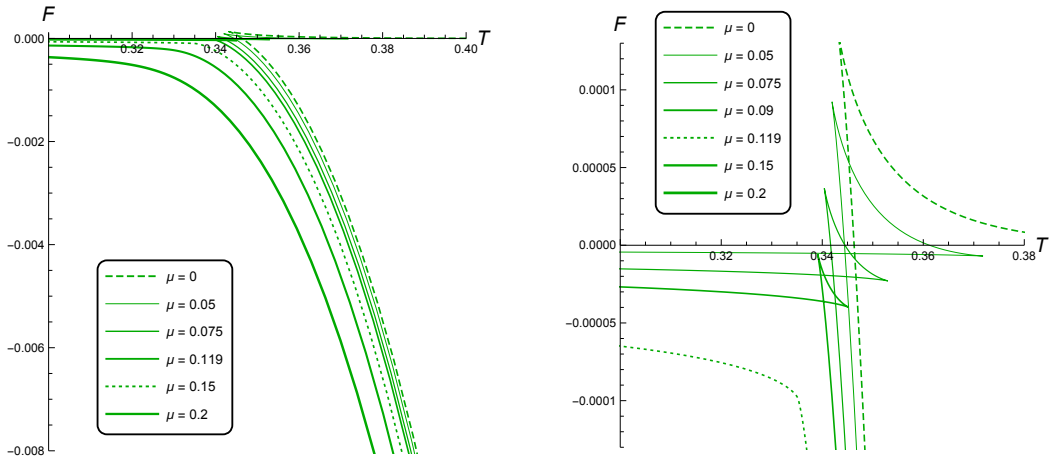


Figure 27. The black hole free energy $F(T)$ for $c = -1$ and different μ in isotropic case (A) and its zoom near $F = 0$ (B).

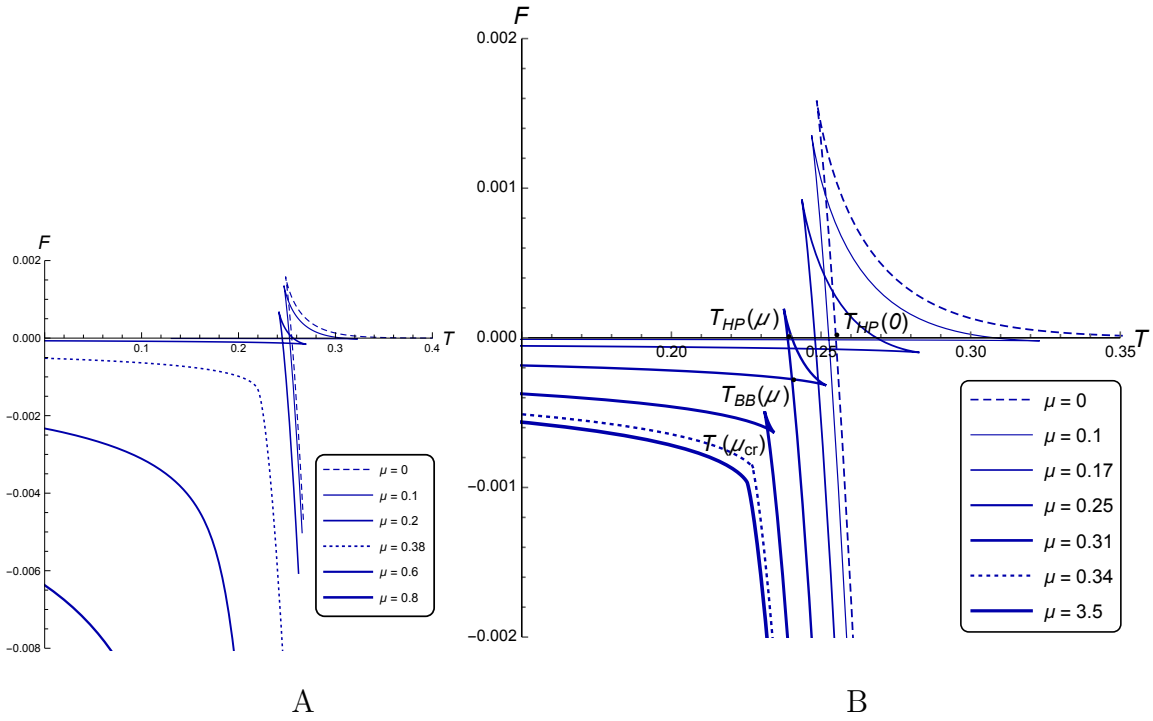


Figure 28. The black hole free energy $F(T)$ for $c = -1$ and different μ in anisotropic case, $\nu = 4.5$, (A) and its zoom near $F = 0$ (B).

where a large black hole transits to a small one. Since both free energy values at $T = T_{BB}$ are equal and negative, meanwhile the free energy of the thermal gas is zero, the system undergoes the phase transition not to a thermal gaz, but to small black hole background. When we increase the chemical potential μ from zero to μ_{cr}, the loop of the swallow-tailed shape shrinks to disappear at $\mu = \mu_{cr}(c, \nu)$. For $\mu > \mu_{cr}(c, \nu)$, the curve of the free energy increases smoothly from higher to lower values of temperature.

It is interesting to compare the phase diagrams corresponding to isotropic and anisotropic backgrounds, see Fig.29. We see that the first order phase transitions start at $(0, T_{HP}(0, 1))$ and $(0, T_{HP}(0, 4.5))$, so that $T_{HP}(0, 4.5) < T_{HP}(0, 1)$ and the transition lines describing transitions from large black holes to small ones stop at points $(\mu_{cr}^{(iso)}, T_{cr}^{(iso)})$ and $(\mu_{cr}^{(aniso)}, T_{cr}^{(aniso)})$, herewith $\mu_{cr}^{(iso)} < \mu_{cr}^{(aniso)}$ and $T_{cr}^{(iso)} > T_{cr}^{(aniso)}$.

It is also important for us to know the position of the large black holes to small black holes transition points at (z_h, T)-plane, see Fig.30. In these plots the horizontal arrows show transitions from the large black holes to small black holes for the anisotropic $\nu = 4.5$ and isotropic cases. The shaded by these arrow areas define the instability zones.

Fig.31 summarizes our discussion of the phase transitions of our black hole isotropic and anisotropic backgrounds. In the next section we put probe strings in these backgrounds to find out information about the confinement/deconfinement phase transition.

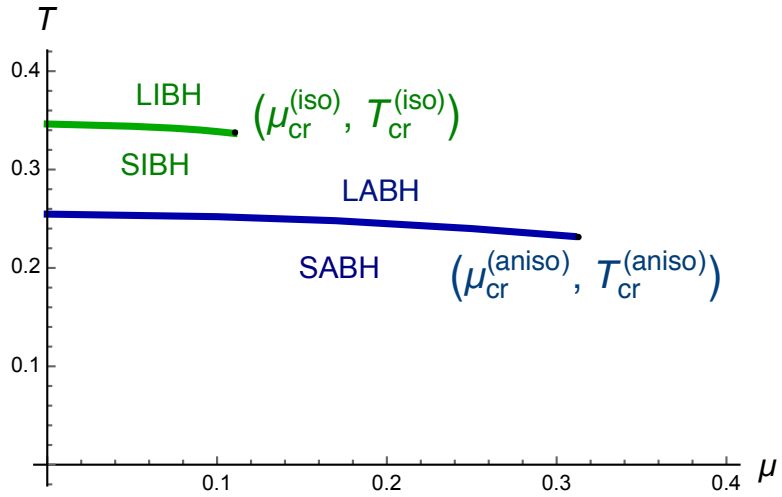


Figure 29. The phase diagrams in the (T, μ)-plane for the isotropic background (green line) and for anisotropic $\nu = 4.5$ background (blue line). LIBH and SIBH (LABH and SABH) indicate the regions of small and large isotropic (anisotropic) black holes.

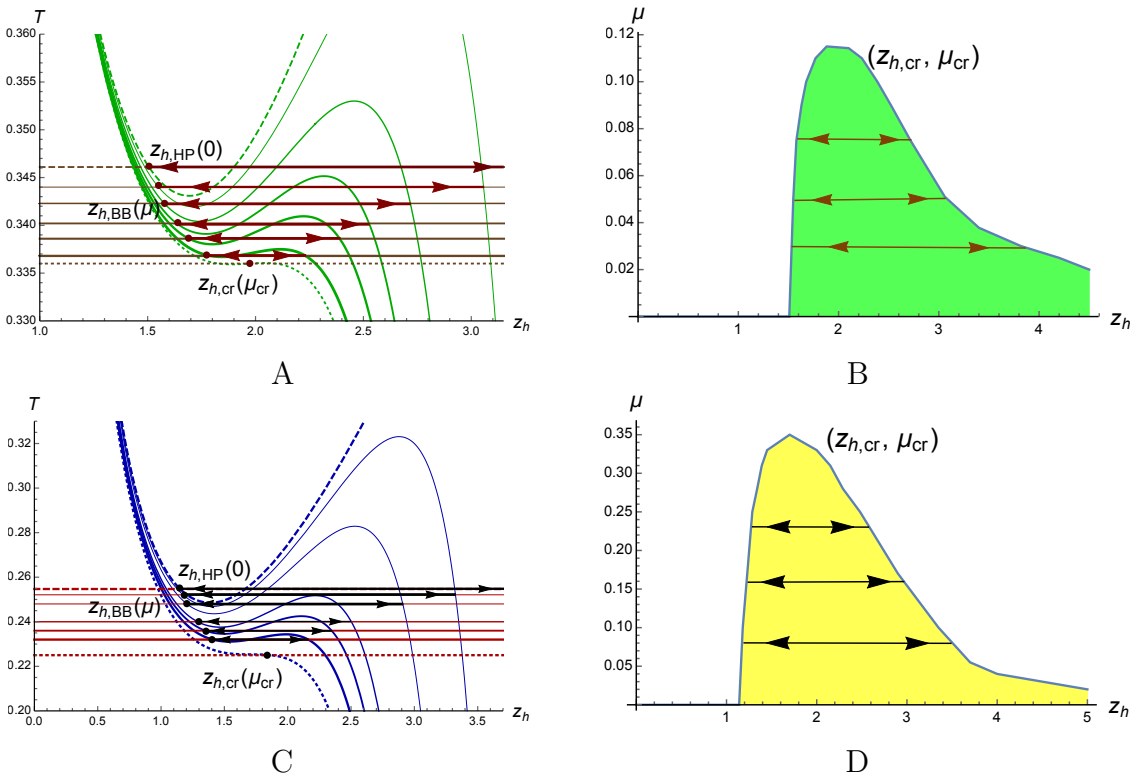


Figure 30. The arrows show transitions large/small black holes for the isotropic (A) and anisotropic $\nu = 4.5$ (C) cases in the (z_h, T)-plane; the large/small holes transitions in the (z_h, μ)-plane are shown by arrows for isotropic (B) and anisotropic (D) cases.

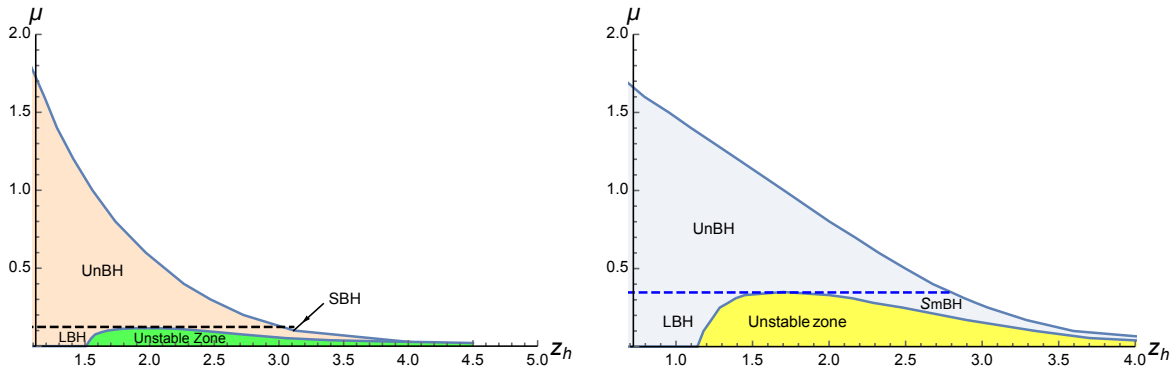


Figure 31. Stability zones at the (z_h, μ)-plane of the blackhole isotropic (A) and anisotropic (B) backgrounds. Here SBH indicates the regions of small black holes, LBH indicates the regions of large black holes, and UnBH indicates the regions of parameters where is no separation on the small and large black holes.

4 Confinement-deconfinement phase transition

4.1 Equation for the dynamical wall

To guarantee the confinement-deconfinement phase transition one has to check the existence of the dynamical wall (DW). The dynamical wall position z_{DW} is defined by the *minimal* extremal point of the effective potential, that depends on the orientation [35] and is related to the warp factor power $P(z)$ and the scalar field ϕ:

$$\mathcal{V}_x = \frac{e^{P(z)+\sqrt{\frac{2}{3}}\phi(z)}}{z^2}\sqrt{g(z)}, \tag{4.1}$$

$$\mathcal{V}_y = \frac{e^{P(z)+\sqrt{\frac{2}{3}}\phi(z)}}{z^{1/\nu+1}}\sqrt{g(z)}. \tag{4.2}$$

Here the subscribte indexes show the orientation of the Wilson loop. Therefore the dynamical wall position is given by equations:

$$\mathcal{V}'_x(z_{DWx}) = 0 \Rightarrow P'(z) + \sqrt{\frac{2}{3}}\,\phi'(z) - \frac{2}{z} + \frac{g'(z)}{2g(z)}\Big|_{z=z_{DWx}} = 0, \tag{4.3}$$

$$\mathcal{V}'_y(z_{DWy}) = 0 \Rightarrow P'(z) + \sqrt{\frac{2}{3}}\,\phi'(z) - \frac{\nu+1}{\nu z} + \frac{g'(z)}{2g(z)}\Big|_{z=z_{DWy}} = 0. \tag{4.4}$$

For zero temperature we have

$$P'(z)+\sqrt{\frac{2}{3}}\,\phi'(z)-\frac{2}{z}\Big|_{z=z_{DWx}}=0, \tag{4.5}$$

$$P'(z)+\sqrt{\frac{2}{3}}\,\phi'(z)-\frac{\nu+1}{\nu z}\Big|_{z=z_{DWy}}=0. \tag{4.6}$$

Substituting $\phi'(z)$ from (2.6) we get the following equations for the positions of the dynamical wall corresponding to x- and y-directions of the quark orientations:

$$\left[P'(z)+\sqrt{\frac{2}{3}}\sqrt{-3P''(z)+\frac{3}{2}P'^2(z)-\frac{6}{z}P'(z)+\frac{4}{z^2}\frac{\nu-1}{\nu^2}}-\frac{2}{z}\right]\Bigg|_{z=z_{DWx}}=0,$$

$$\left[P'(z)+\sqrt{\frac{2}{3}}\sqrt{-3P''(z)+\frac{3}{2}P'^2(\xi)-\frac{6}{z}P'(\xi)+\frac{4}{z^2}\frac{\nu-1}{\nu^2}}-\frac{\nu+1}{\nu z}\right]\Bigg|_{z=z_{DWy}}=0.$$

4.2 $P(z)=cz^2/2$

We take the simplest case (2.31) again. Therefore we choose the expression with positive sign in (2.56), and equations (4.3) and (4.4) become:

$$\mathcal{DW}_x\equiv cz+\frac{1}{\nu z}\sqrt{\frac{2}{3}}\sqrt{3c\,\nu^2z^2\left(\frac{cz^2}{2}-3\right)+4\nu-4}-\frac{2}{z}+\frac{g'}{2g}\Big|_{z=z_{DWx}}=0, \tag{4.7}$$

$$\mathcal{DW}_y\equiv cz+\frac{1}{\nu z}\sqrt{\frac{2}{3}}\sqrt{3c\,\nu^2z^2\left(\frac{cz^2}{2}-3\right)+4\nu-4}-\frac{\nu+1}{\nu z}+\frac{g'}{2g}\Big|_{z=z_{DWy}}=0. \tag{4.8}$$

Note that in both equations there is also a dependence of the corresponding blackening functions on ν. The phase transition from confinement to deconfinement occurs when the corresponding equations loss solutions.

To see the dependence of the dynamical wall position on the parameters of the metric, it is useful to study the details of dependence of the different terms defined $\mathcal{DW}_x$, $\mathcal{DW}_y$ and $\mathcal{DW}_{iso}$ on these parameters. Here $\mathcal{DW}_{iso}$ denotes the left-hand side of the equation, similar to (4.8), in the isotropic case.

4.2.1 Zero temperature

Let us first consider the case of the zero temperature, i.e. $g = 1$. In this case we deal with equations

$$z = z_{DWx}: \quad \sigma(z,\nu,c) = \frac{2}{z} \quad or \quad \sigma_x(z,\nu,c) = 0, \tag{4.9}$$

$$z = z_{DWy}: \quad \sigma(z,\nu,c) = \frac{\nu+1}{\nu z} \quad or \quad \sigma_y(z,\nu,c) = 0, \tag{4.10}$$

where

$$\sigma(z,c,\nu) \equiv cz + \frac{1}{\nu z}\sqrt{\frac{2}{3}}\sqrt{3c\,\nu^2 z^2\left(\frac{cz^2}{2}-3\right)+4\nu-4}. \tag{4.11}$$

We also use notations:

$$\sigma_x(z,c,\nu) \equiv cz + \frac{1}{\nu z}\sqrt{\frac{2}{3}}\sqrt{3c\,\nu^2 z^2\left(\frac{cz^2}{2}-3\right)+4\nu-4}-\frac{2}{z}, \tag{4.12}$$

$$\sigma_y(z,c,\nu) \equiv cz + \frac{1}{\nu z}\sqrt{\frac{2}{3}}\sqrt{3c\,\nu^2 z^2\left(\frac{cz^2}{2}-3\right)+4\nu-4}-\frac{\nu+1}{\nu z}. \tag{4.13}$$

Behavior of $\sigma_x(z,c,\nu)$ and $\sigma_y(z,c,\nu)$ as functions of z are shown in Fig.32. The positions of the dynamical walls are defined by the intersections of the solid blue and magenta lines representing $\sigma_x(z,c,\nu)$ and $\sigma_y(z,c,\nu)$ with the horizontal line $\sigma = 0$.

To show that the presence of the dilaton field supports the appearance of the DW, we display parts of the expressions $\sigma_x(z,c,\nu)$ and $\sigma_y(z,c,\nu)$ without the square roots, that are originated from the dilaton fields, by the dashed lines in Fig.32.B and C. We see that these dashed lines never intersect horizontal axis, therefore in these cases there are no DW solutions.

Solutions to equations (4.9) and (4.10) can also be represented as the boundary between positive and negative values of functions $\sigma_x(z,c,\nu)$ and $\sigma_y(z,c,\nu)$. Taking $\nu = 1$ provides us with the isotropic case result (Fig.32.D). We see that the critical $c = c_{cr}$, above which there are no solutions in all cases, is $c_{cr} = 0$. For $c > 0$ our consideration is not valued, since the scalar field becomes complex.

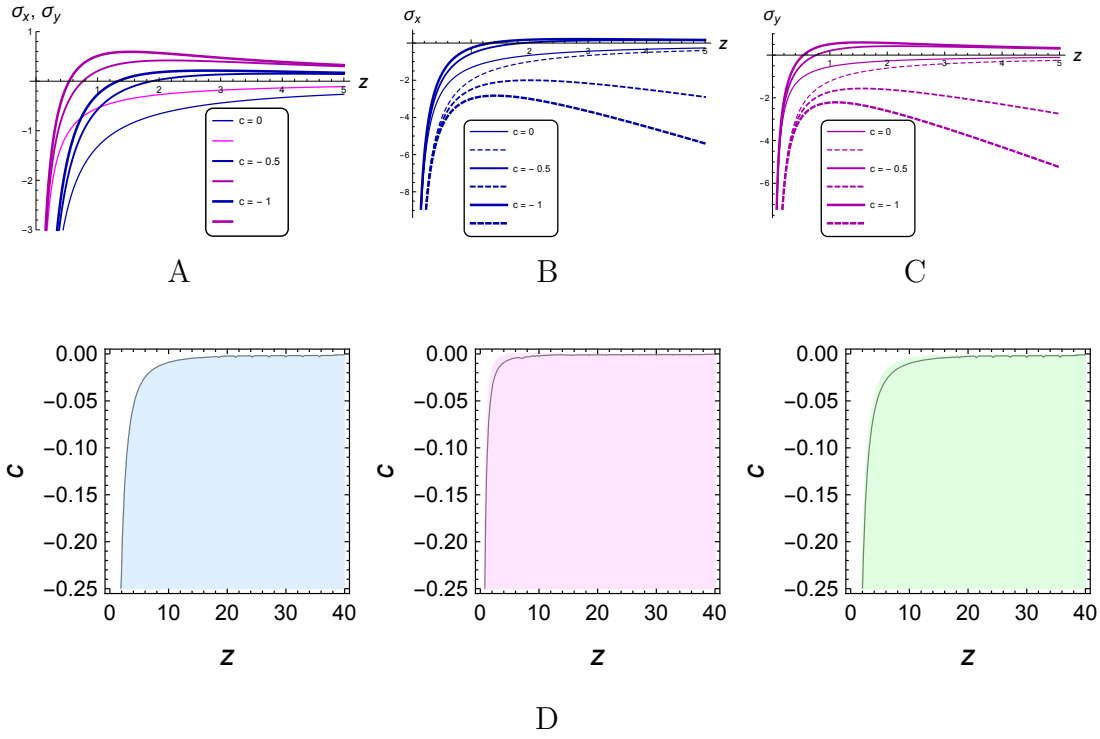


Figure 32. Functions $\sigma_x(z, c, \nu)$ (blue lines) and $\sigma_y(z, c, \nu)$ (magenta lines) for different c with dilaton contributions (solid lines) and without them (dashed lines) together (A) and separately (B, C); solutions to (4.9) (boundary of blue and white areas), to (4.10) (boundary of magenta and white areas) and for the isotropic case (boundary of green and white areas) (D).

4.2.2 Non-zero temperature, zero chemical potential

Let us take the nontrivial blackening function. The blackening function modifies the DW equations. It is convenient to present these equations in the form

$$z = z_{DWx}: \quad \Sigma(z, z_h, \nu, c) = \frac{2}{z}, \tag{4.14}$$

$$z = z_{DWy}: \quad \Sigma(z, z_h, \nu, c) = \frac{\nu + 1}{\nu z}, \tag{4.15}$$

where

$$\Sigma(z, z_h, c, \nu) \equiv \sigma(z, c, \nu) + G(z, z_h, c, \nu). \tag{4.16}$$

Function $\sigma(z, \nu, c)$ is given by (4.11) and

$$G(z, z_h, c, \nu) \equiv \frac{g'}{2g}. \tag{4.17}$$

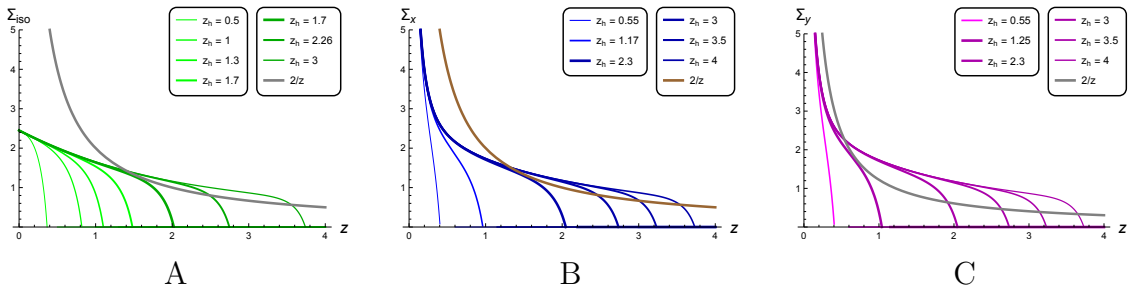


Figure 33. A) Dynamical walls' positions in isotropic case are given by the intersections of green lines representing $\Sigma_{iso}(z)$ and the grey line representing $2/z$; B) dynamical walls' positions, corresponding to the Wilson loop W_x in the anisotropic case $\nu = 4.5$, are given by intersections of blue lines representing $\Sigma(z)$ and the brown line representing $2/z$; C) dynamical walls' positions, corresponding to the Wilson loop W_y in the anisotropic case $\nu = 4.5$ are given by the intersections of magenta lines representing $\Sigma(z)$ and the grey line representing $(\nu+1)/(\nu z)$. Here we vary z_h and c. In all cases to get the DW position we take the minimal intersection point.

We find the solutions of equations (4.14) and (4.15) numerically. To visualize the location of these solutions we plot $\Sigma(z, z_h, c, \nu)$ as a function of z for different values of parameters z_h, ν, c and find its intersection with $2/z$ for the Wilson loop W_x and with $(\nu+1)/(\nu z)$ for the Wilson loop W_y in Fig.33. If there are two intersection points, we take the minimal one and we call it the minimal intersection point. In all cases to get the corresponding DW position we take the minimal intersection point. From Fig.33.A we see that for $z_h > z_{h,cr}$ the dynamical wall always appears, as there are intersections of the grey and dark green lines. At the critical horizon (the thick dark green line) there is a touch of these two lines and for $z < z_{h,cr}$ (lighter green lines) there is no intersection at all, therefore confinement disappears.

The light blue curves in Fig.33.B do not cross the grey line and for these cases there are no dynamical dynamical walls. The dark blue lines cross the brown one and for the corresponding temperature there is the quark confinement, meanwhile the thick dark blue line just touches the grey line and at this temperature the phase transition occurs. The similar picture can be seen at Fig.33.C, corresponding to different orientation of quark pairs.

Therefore the dynamical wall always appears for $z_h > z_{h,cr}$. The particular values of $z_{h,cr}$ are different for isotropic (A) and anisotropic (B, C) cases and depend on the quark orientations. This appearance/disappearance of dynamical walls corresponds to confinement and deconfinement phases. The phase transition between these two regimes occurs at $z = z_{h,cr}$.

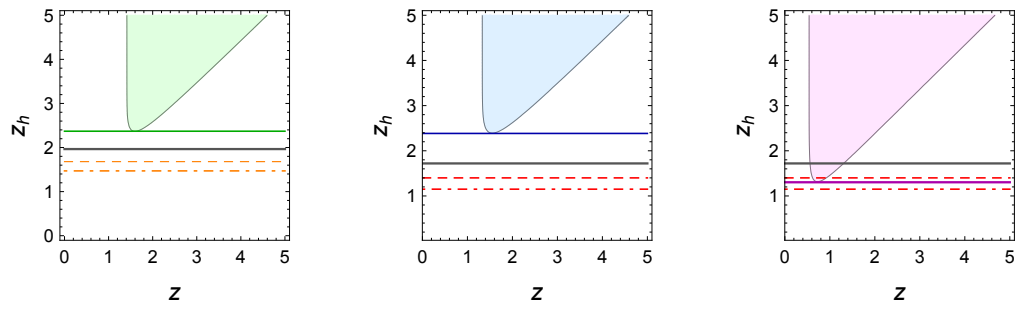


Figure 34. A) Dynamical walls' positions in isotropic case are located on the left part of the boundary of the green and white areas. We see that for given $z_h > 2.304$ there are two solutions and for $z_h = 2.304$ there is only one $z_{DWiso} = 1.455$. B) Dynamical walls' positions corresponding to the Wilson loop W_x are located on the left part of the boundary of the blue and white ares. We see that for given $z_h > 2.376$ there are two solutions and for $z_h = 2.376$ only one $z_{DWx} = 1.503$. C) Dynamical walls' positions corresponding to the Wilson loop W_y are located on the left part of the boundary of the magenta and white ares. We see that for given $z_h > 1.326$ there are two solutions and for $z_h = 1.326$ only one $z_{DWiso} = 0.6871$. Here $\nu = 4.5$ and $c = -1$. Dashed orange and red lines show positions of the critical $z_{h,min}(0)$ in the corresponding isotropic and anisotropic backgrounds, and point-dashed lines show positions of the horizons $z_{h,HP}(0)$, where the HP transitions take place at zero chemical potential in the isotropic and anisotropic cases. The dark grey lines show $z_{h,cr} = z_{h,cr}(\mu_{cr})$ the value of the horison at the inflection points. These plots show that all dynamical walls appear below the corresponding horizons, i.e. $z_{DW}(z_h, \nu) < z_h$ and these horizons z_h are larger than $z_{h,min}(0)$ and $z_{h,cr}$ for the isotropic case and for W_x case, but they can be smaller than $z_{h,min}(0)$ and $z_{h,cr}$ in the anisotropic W_y case. The positions of minimal z_h admitted the DW, $z_{h,DW}$ are indicated by dark green, dark blue and dark magenta lines.

In Fig.34 solutions to equations (4.14), (4.15) are located on the boundary of the colored and white areas. Since to find the dynamical walls' positions we have to take the minimal solutions, the dynamical walls' positions are located on the left parts of boundaries between the colored and white areas.

4.2.3 Non-zero chemical potential

We can also study how these plots look for non-zero chemical potential. The positions of the dynamical walls for non-zero temperature and non-zero chemical potential in isotropic and anisotropic cases are presented in Fig.35.A and Fig.35.B correspondingly.

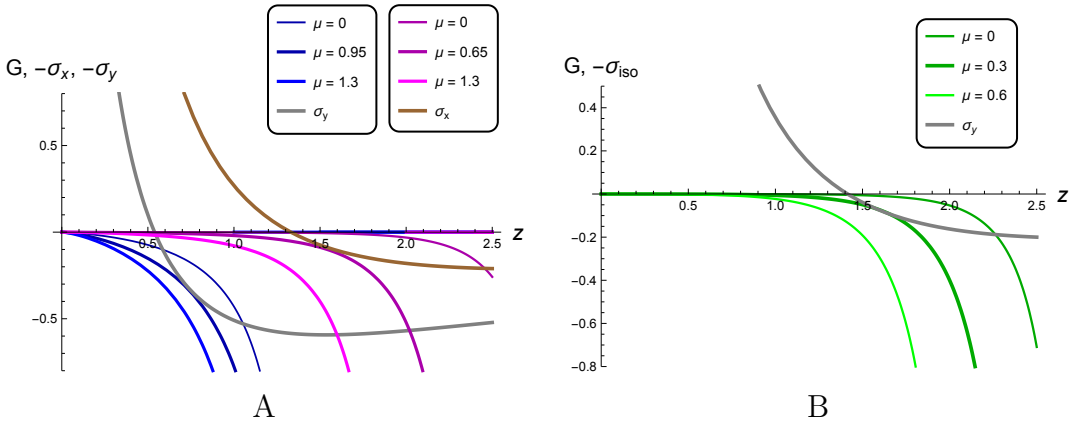


Figure 35. The positions of the dynamical dynamical walls $G = -\sigma_x$ for $z_h = 1.5$ and $G = -\sigma_y$ for $z_h = 3$ in anisotropic $\nu = 4.5$ (A) and isotropic $G = -\sigma_{iso}(z)$ (B) cases, $c = -1$.

It is convenient to write equations (4.9) and (4.10) in the form

$$z = z_{DWx}: \qquad \Sigma(z, z_h, \mu, c, \nu) = \frac{2}{z}, \tag{4.18}$$

$$z = z_{DWy}: \qquad \Sigma(z, z_h, \mu, c, \nu) = \frac{\nu + 1}{\nu z}, \tag{4.19}$$

where

$$\Sigma(z, z_h, \mu, c, \nu) \equiv \sigma(z, c, \nu) + G(z, z_h, \mu, c, \nu), \tag{4.20}$$

$$G(z, z_h, \mu, c, \nu) \equiv \frac{g'}{2g} \tag{4.21}$$

and $\sigma(z, c, \nu)$ is defined by (4.11).

The light blue and dark blue curves in Fig.35.A represent the function $G(z, z_h, \mu, c, \nu)$ for $\nu = 4.5$, $c = -1$, $z_h = 1.5$ and different μ. The light magenta and dark magenta lines correspond to $G(z, z_h, \mu, c, \nu)$ for the same set of parameters and $z_h = 3$. The thick lines, that touch σ_x (grey line) and σ_y (brown line), depict the critical values of chemical potential μ. Thus the presence and the particular position of the horizon modifies the position of dynamical walls as compare with the zero temperature case ($g = 1$) presented in Fig.32. Anisotropy also influences on the dynamical walls' position. This can be seen from comparing of Fig.35.A and Fig.35.B, where the isotropic case is pictured.

To find the phase transition line we have to determine $\mu(z_h, c, \nu, W_i)$, here W_i indicates the orientation of the Wilson line, W_x or W_y, for given z_h such that for any $\mu > \mu(z_h, c, \nu, W_i)$ there is no real solution of equations (4.18) and (4.19). To find these

points, it is convenient to draw the contour plots for functions $\mathcal{DW}_x$ and $\mathcal{DW}_y$ near zero. They are presented in Fig.36 and Fig.37 correspondingly. For comparison we present in Fig.38 the contour plots for $\mathcal{DW}_{iso}$ near 0.

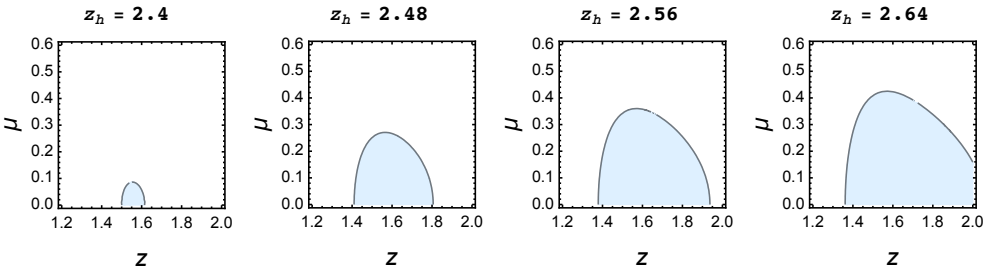


Figure 36. Contour plots for $\mathcal{DW}_x$ near zero for different z_h (labels above).

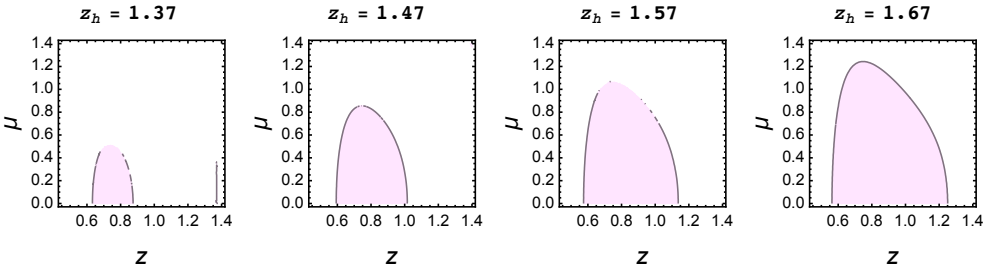


Figure 37. Contour plots for $\mathcal{DW}_y$ near zero for different z_h (labels above).

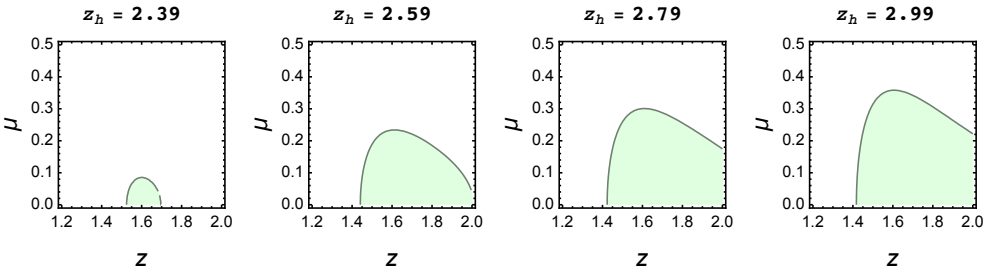


Figure 38. Contour plots for $\mathcal{DW}_{iso}$ near zero value.

4.2.4 The dynamical wall position

All previous considerations can be summarized in contour plots. Namely, we can draw the contours for the locations of the effective potentials' derivatives $\mathcal{V}'_{xy} = 0$ in the (z, z_h)-plane, keeping $c = -1$ and considering two cases $\nu = 1$ (Fig.39) and $\nu = 4.5$

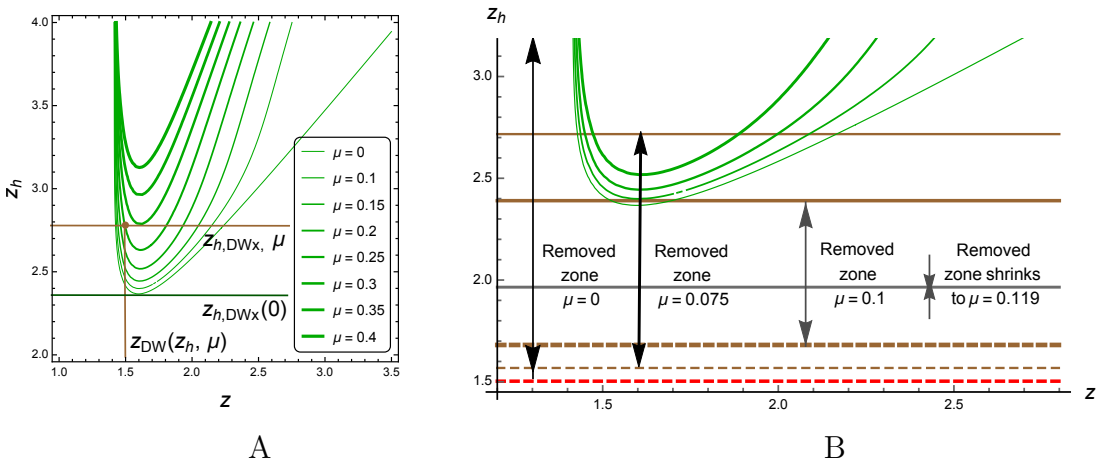


Figure 39. A) The location of extreme points of the effective potential in the isotropic case $\nu = 1$, $c = -1$ for different z_h and μ are shown by green lines with different thickness, depending on the values of the chemical potential. Dynamical walls' positions are located on the left parts of these curves. B) Locations of instability zones corresponding to different μ are shown by the black lines with arrows.

(Fig.40). Different contours correspond to different values of μ. Dynamical walls' positions correspond to the minimal z for fixed horizon z_h and chemical potential μ (Fig.39.A). The positions of the dynamical walls in the anisotropic case differ for longitudinal x and transversal $y_{1,2}$ quark pair orientation (Fig.40.A and C, correspondingly). Transversal case is characterized by smaller values of z_h and minimal z for the same chemical potential μ.

On Fig.39.B and Fig.40.B and D the instability regions of the background for $\mu = 0$ are indicated by black arrows. For fixed $0 < \mu < \mu_{cr}$ they are shown as domains between corresponding brown solid and dashed lines of the same thickness. The thick magenta line on Fig.40.D shows the value of z_h, at which the transition between large and small black holes disappears and the "removed zone" shrinks to $z_{h,cr}$ for the curve $\mu = \mu_{cr}$. For isotropic case $\mu_{cr}^{(iso)} = 0.119$ and for anisotropic one at $\mu_{cr}^{(anis)} = 0.34$ and it happens at $z_h = z_{h,cr}^{(iso)} = 1.97$ and at $z_h = z_{h,cr}^{(aniso)} = 1.70$ in the isotropic and anisotropic cases, respectively. Note, the line $z_h = z_{h,cr}^{(iso)}$ is below $z_{h,DW}^{(iso)}$, the value of horizon for which the DW can appear in the isotropic case. In the anisotropic case the line $z_h = z_{h,cr}^{(aniso)}$ is below values of $z_{h,DWx}$, for which the DW for W_x can appear, $z_{h,cr}^{(aniso)} < z_{h,DWx}$, but above the values of horizons, for which the DW can appear for W_y, i.e. $z_{h,cr}^{(aniso)} > z_{h,DWy}$ (see Fig.41 and discussion below).

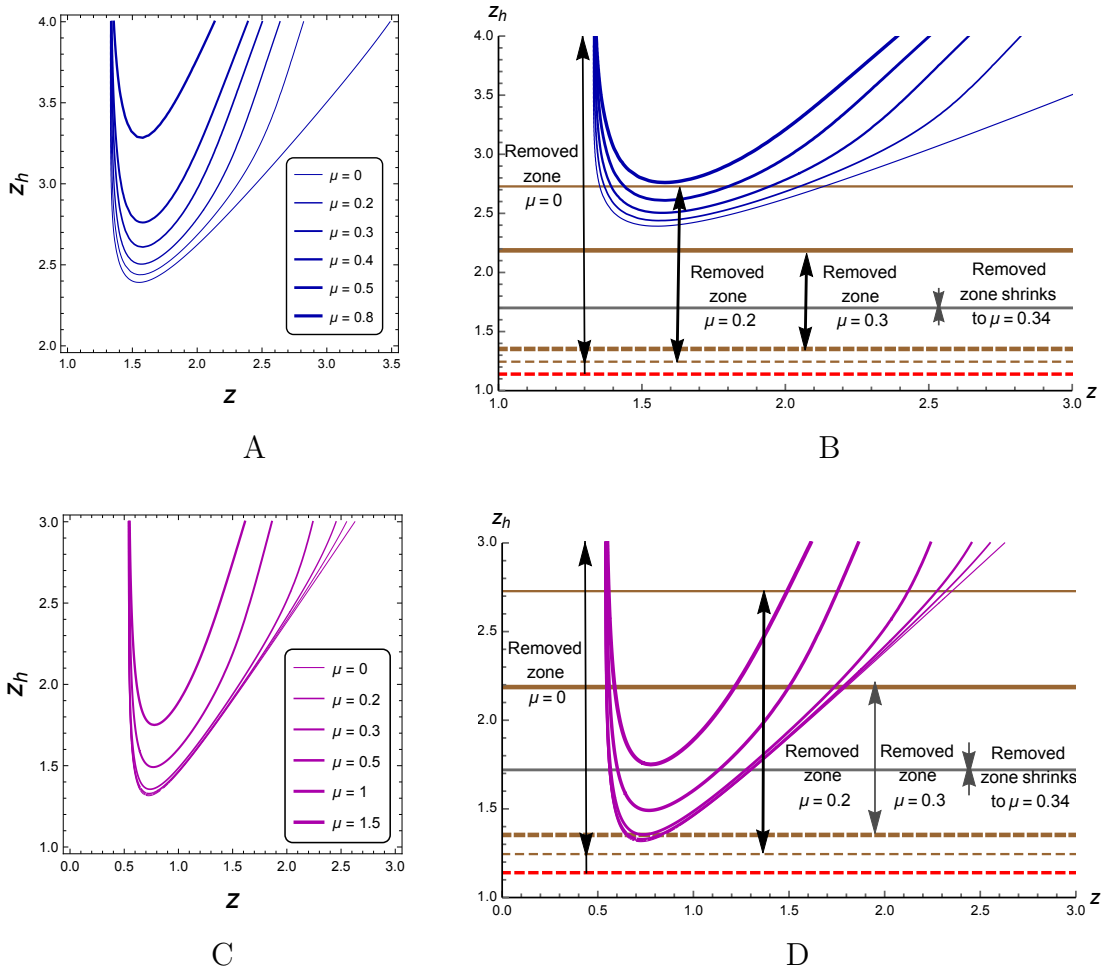


Figure 40. The location of extreme points of effective potential in the anisotropic case $\nu = 4.5$, $c = -1$ for different z_h, μ and different orientations of quark pairs are shown by lines of different thickness depending on the values of the chemical potential, and colors, for the Wilson longitudinal line W_x (A and B) with dark blue and for the Wilson transverse line W_y with dark purple lines (B and D). B) and D). The location of the instability zones corresponding to different μ is shown by black lines with arrows.

4.2.5 Phase transition lines and critical points

Confinement/deconfinement phase transition for the isotropic case $\nu = 1$ is shown on Fig.42. Note that for zero chemical potential the Hawking-Page temperature is less than the temperature of the confinement/deconfinement transition temperatute, $T_{HP}(0) < T_{CD}(0)$. The temperature of the black hole to black hole transition $T_{BB}(\mu)$ is less than the temperature of the confinement/deconfinement transition $T_{CD}(\mu)$ for $0 < \mu < \mu_b^{(iso)}$, i.e. $T_{BB}(\mu) < T_{CD}(\mu)$, and $T_{BB}(\mu) > T_{CD}(\mu)$ for $\mu_b^{(iso)} < \mu < \mu_{cr}^{(iso)}$ (let us remind that

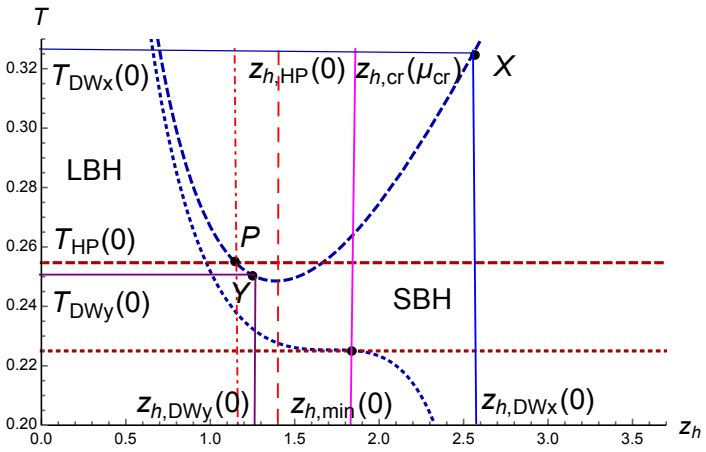


Figure 41. The plot explains the difference between phase diagrams for Wilson lines W_x and W_y for $\nu = 4.5$. The coordinates of points X,Y and P are $(z_{h,DWx}(0), T_{DWx}(0))$, $(z_{h,HP}(0), T_{HP}(0))$ and $(z_{h,DWx}(0), T_{DWx}(0))$. We see that P is in the SBH region, and X in the LBH region. The red dashed and point-dashed lines, and the magenta line are the same as at Fig.34.

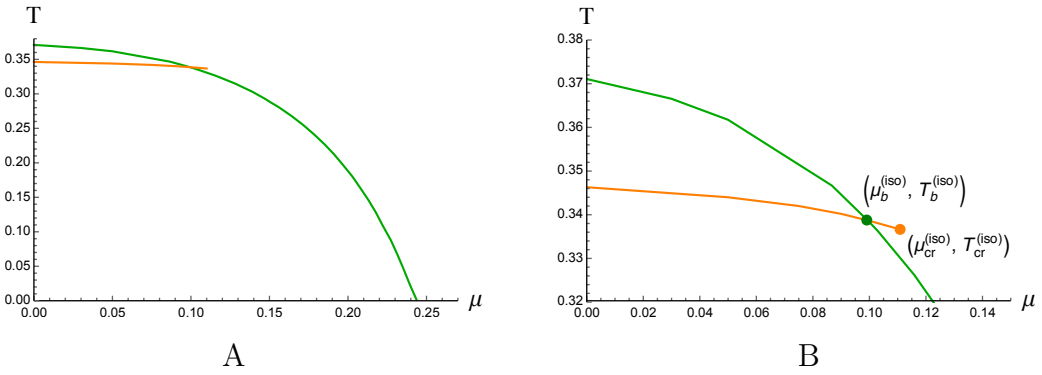


Figure 42. Confinement-deconfinement phase transition in the isotropic case, $\nu = 1$, $c = -1$ for the Wilson line W_{iso} (green) and the background (orange) (A). Plot (B) is a zoom of (A) near the intersection point $(\mu_b^{(iso)}, T_b^{(iso)})$ and critical point $(\mu_{cr}^{(iso)}, T_{cr}^{(iso)})$.

the background transition line stops at $(\mu_{cr}^{(iso)}, T_{cr}^{(iso)})$). Therefore, the phase transition line for $0 < \mu < \mu_b^{(iso)}$ is determined by the background transition line (the orange lines at Fig.42) and for $\mu \geq \mu_b^{(iso)}$ by the isotropic confinement/deconfinement transition line (the green lines at Fig.42). This is in agreement with results of the previous studies [46] and refs. therein, where it has been argued that the transition for $\mu < \mu_b^{(iso)}$ is the first-order phase transition (FOPT) and for $\mu > \mu_b^{(iso)}$ is a smooth one.

The plots in Fig.41 explain the difference between phase diagrams of Wilson lines

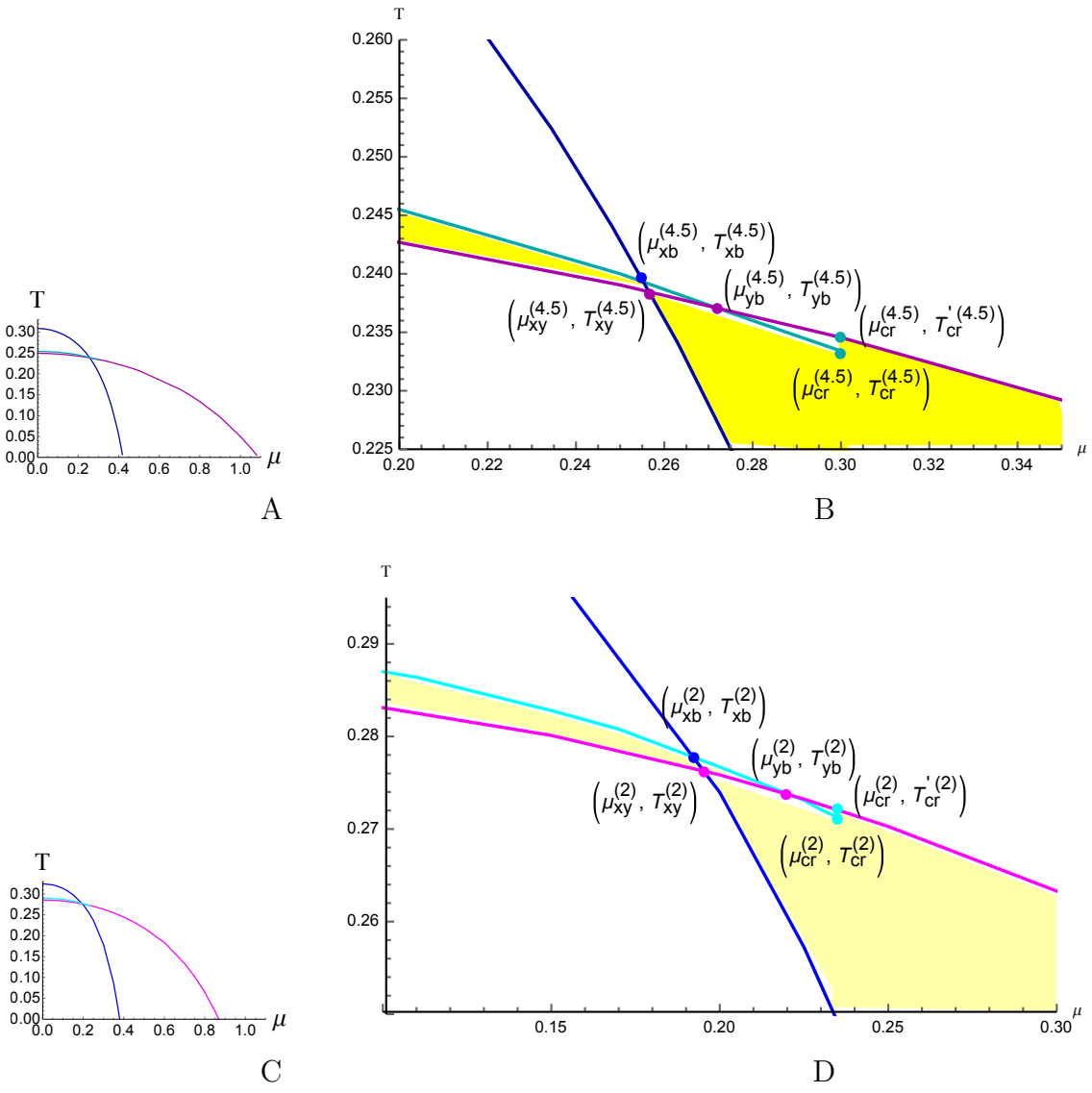


Figure 43. Confinement-deconfinement phase transition in the anisotropic case, $\nu = 4.5$, $c = -1$, for the Wilson line W_x (blue), the Wilson line W_y (magenta) and the background (cyan) (A). Plot (B) is a zoom of (A) near the critical points (μ_{xb}, T_{xb}), (μ_{yb}, T_{yb}) and FOPT $(\mu_b, T_b) \to (\mu_b, T_b')$. Plots (C) and (D) are the analogues of (A) and (B) for $\nu = 2$.

W_x and W_y for $\nu = 4.5$. In this plot we see that for $\mu = 0$ the minimal value of the horizon $z_{h,DWx}$, for which the DW can appears for W_x, corresponds to small black hole, meanwhile the same horizon for W_y, $z_{h,DWy}$, corresponds to large black hole. By this reason we have

$$T_{DWy}(0) < T_{HP}(0) < T_{DWx}(0). \tag{4.22}$$

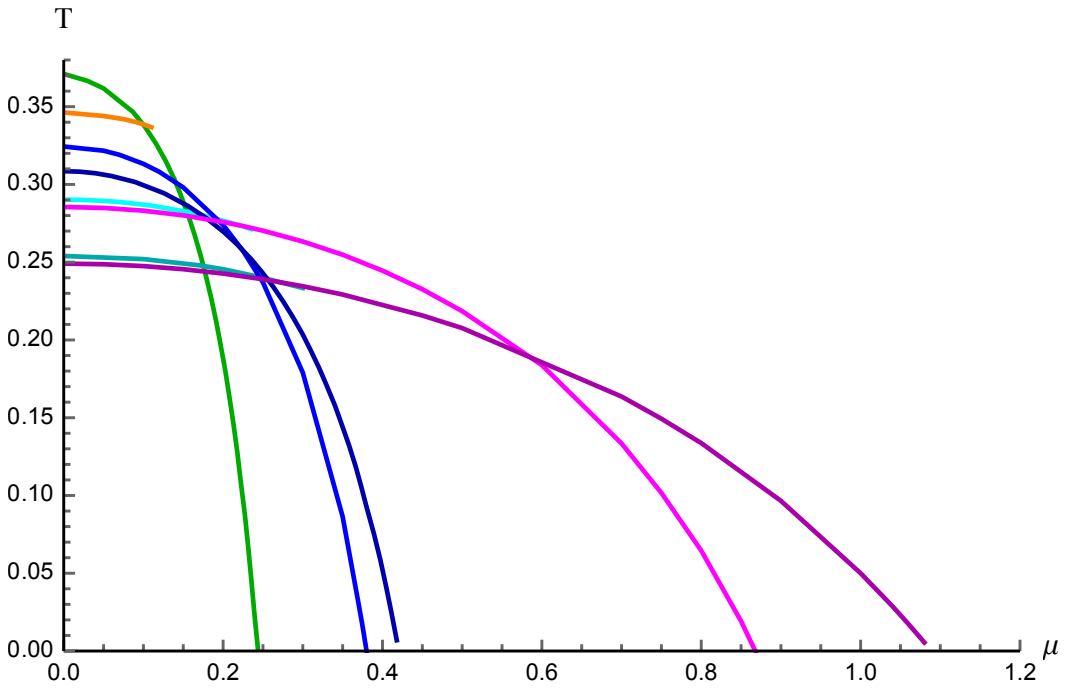


Figure 44. Confinement-deconfinement phase transitions of Wilson lines W_{iso} for $\nu = 1$ (green), W_x and W_y for $\nu = 2$ (blue and magenta) and $\nu = 4.5$ (dark blue and dark magenta); the background transition lines for $\nu = 1$ (orange), $\nu = 2$ (cyan) and $\nu = 4.5$ (dark cyan).

Explicit numerical calculations show that

$$T_{CDy}(\mu) < T_{BB}(\mu) < T_{CDx}(\mu) \quad \text{for} \quad 0 < \mu < \mu_{xb}. \tag{4.23}$$

The confinement/deconfinement transition for the anisotropic case $\nu = 4.5$ is shown on Fig.43.A and B. The phase diagram for the longitudinal Wilson line W_x is depicted by the blue lines, for transversal lines W_y by the magenta lines and for the anisotropic background by the cyan lines. Wilson lines can also have arbitrary orientations, that corresponds to a modification of blue and magenta lines to some intermediate configuration.

The case $\nu = 2$ can be considered as intermediate between the isotropic one and our main case $\nu = 4.5$ (Fig.43.C and D). Fig.44 combines all the three cases $\nu = 1, 2, 4.5$ thus showing isotropization.

5 Conclusion and discussion

We have considered 5-dimensional Einstein-dilaton-two-Maxwell-scalar system. We have found anisotropic solutions for this system by using the potential reconstruction method, i.e. choosing the corresponding dilaton and Maxwell potentials for the given background. This method has been used for isotropic cases in [45, 46, 49] and refs therein.

Our anisotropic background is the deformed AdS_5 that has the UV boundary with two suppressed transversal coordinates and the IR boundary with the suppressed time and longitudinal coordinates. One can say that in this background two different 3-dimensional reductions, one in the UV domain and the other in the IR domain, are realized. The UV reduction is realized by the suppression of the original transversal coordinates, meanwhile the IR reduction is obtained by the suppression of the longitudinal and temporal coordinates. For the corresponding isotropic solution there is no 3-dim reduction neither in UV nor in IR regions.

In our calculations the warped factor is chosen in such a way that the explicit analytical calculations can be performed. This solution can be generalized to provide a more realistic model. In this case, similar to the isotropic case, the solution can be given only in terms of quadratures. We solved the equations of motion to obtain a family of the black hole solutions by modifying the initial potential corresponding to zero temperature. In this construction the special boundary conditions for the dilaton field are chosen, namely we have required that the dilaton field is zero at the horizon.

We have also studied the thermodynamical properties of the constructed black hole background and found the large/small black hole phase transitions at the temperature magenta $T_{BB}(\mu)$. This result is presented in Fig.29. At $\mu = 0$ and for $T < T_{HP}(0)$, the black hole dissolves to thermal gas which is thermodynamically stable for $T < T_{HP}(0)$. When the system cools down with the chemical potential less than the critical value μ_{cr}, the background undergoes the phase transition from a large to a small black hole. This is a generalization of the corresponding effect in the isotropic case [45, 46, 50–52]. We have found that $T_{BB}^{(aniso)}(\mu) < T_{BB}^{(iso)}(\mu)$ and the value of the critical chemical potential, value up to which this phase transition exists, is bigger in the anisotropic case as the compare to the isotropic one, $\mu_{cr}^{(\nu)} > \mu_{cr}^{(iso)}$, see Fig.44. Also, we have found that the point $(\mu_{cr}^{(\nu)}, T_{cr}^{(\nu)})$ for $\nu \to 1$ goes smoothly to $(\mu_{cr}^{(iso)}, T_{cr}^{(iso)})$.

We have studied the behavior of the temporal Wilson loops in the constructed background. For this purpose we have considered open strings in these backgrounds and identified the two ends of an open string as a quark and antiquark pair in the dual holographic QCD. As in the isotropic case, the equations of motion for this open string support two configurations – U-shape and straight-shape of the open strings.

The U-shape for large distances between quarks provides the quark confinement and is realized in the presence of the dynamical wall (DW). We have found the domains in the (z_h, μ) planes, where the DW can appear for the longitudinal and transversal orientation of the temporal Wilson loops. In these regions the open strings cannot exceed the DW, even the separation of the quark and antiquark goes to infinite and the quark confinement takes place. We have found that the phase diagram depends on the orientation, cf.[35]. Taking into account the instability zones of the anisotropic background, we have found more complicated confinement/deconfinement phase diagrams for different oriented temporal Wilson loops and the details are the following:

- In the case of the longitudinal orientation, W_{Tx}, parts of regions near zero values of the chemical potential, $\mu < \mu_{xb}$, enter to the instability regions of our background, where the small black holes collapse to large ones. Here the horizon suddenly blows up to pass the critical value $z_{h,DWx}(\mu)$ (see Fig.18 and Fig.40, at the last plots these jumps are indicated by the arrows), so that the confinement phase transforms to the deconfinement one by a phase transition. While the chemical potential is greater than the critical value $\mu > \mu_{xb}$, the black hole horizon grows gradually and continuously passes the critical horizon, corresponding to (μ_{cr}, T_{cr}), so that the confinement phase transforms to the deconfinement phase smoothly. In other words, the confinement-deconfinement line is determined by the probe string behavior itself. It is worth to notice that the similar situation takes place in the isotropic case.

- In the case of the transversal orientation, W_y, situation is more interesting. It happens, that the background phase transition line for small μ, $\mu < \mu_{yb}$, is located above the phase transition line for the Wilson line, and for small μ we have a smooth confinement-deconfinement phase transition. For $\mu_{yb} < \mu < \mu_{cr}$ we fall in the zone of instability of the background and the first order phase transition takes place.

As to the future investigations, the following natural questions to static and non-static properties of our model are worth noting. As to static properties, it is natural to

- investigate the opportunity to fix our holographic QCD model by a suitable choice of the function $P(z)$ in (2.16), so that in the isotropic limit it would fit the Cornell potential known by lattice QCD; it would be interesting to perform calculations on an anisotropic lattice and compare these future results with our model;

- consider more general anisotropic backgrounds and derive the corresponding anisotropic RG flows;
- study the Regge spectrum for mesons, adding the probe gauge fields to the backgrounds; we expect that similarly to the isotropic case, the gauge potential can be fixed requiring the linear Regge spectrum for mesons;
- consider estimations for direct photons;
- evaluate transport coefficients and their dependence on the anisotropy.

As to the thermalization processes, which are the main motivations of our considered of the anisotropic background, we suppose to reexamine

- the shock wave collisions in the anisotropic background with the warped factor;
- thermalization times for 2-point correlators; for the no-dilaton case this question has been addressed in [31, 34];
- time dependence of the transport coefficients, for the no-dilaton model see [35].

In this paper we have studied a particular anisotropic model specified by the anisotropy parameter ν and in all plots we take $\nu = 4.5$, since just this case reproduces the total multiplicity dependence on energy, $\mathcal{M} \sim s^{0.155}$. It would be interesting to find isotropization of our solution and it is natural to expect that in this case the both phase transition lines, the large/small black hole transition and the string confinement/deconfinement transition, will smoothly move to their isotropic parters. We leave these matters to future works.

Acknowledgments

This work was presented at the Helmholtz International Summer School "Hadron Structure and Hadronic Matter, and Lattice QCD", 20.08.2017-2.09.2017, BLTP JINR, Dubna, Russia, the 9th mathematical physics meeting: "Summer School and Conference on Modern Mathematical Physics", 18.09.2017-23.09.2017, Belgrade, "IV Russian-Spanish Congress Particle and Nuclear Physics at all Scales and Cosmology", 4.09.2017-8.09,2017, Dubna.

Appendix

A Equations of motion

$$
\begin{aligned}
00: \quad & b'' - \frac{(b')^2}{2b} + b'\left(\frac{g'}{2g} - \frac{2}{\nu z}\right) + \frac{2b}{z^2}\left(\frac{1}{3} + \frac{2}{3\nu} + \frac{1}{\nu^2}\right) - \frac{bg'}{3zg}\left(1 + \frac{2}{\nu}\right) + \frac{b}{6}(\phi')^2 + \frac{b^2 V}{3z^2 g} + \\
& + \frac{z^2 f_1 (A_t')^2}{6g} + \frac{q^2 z^{-2+\frac{4}{\nu}} f_2}{6g} = 0, \\
11: \quad & g'' + \frac{3gb''}{b} - \frac{3g(b')^2}{2b^2} - \frac{6gb'}{b\nu z} - g'\left(\frac{2}{z} + \frac{4}{\nu z} - \frac{3b'}{b}\right) + \frac{2g}{z^2}\left(1 + \frac{2}{\nu} + \frac{3}{\nu^2}\right) + \frac{g}{2}(\phi')^2 + \frac{bV}{z^2} + \\
& - \frac{z^2 f_1 (A_t')^2}{2b} + \frac{q^2 z^{-2+\frac{4}{\nu}} f_2}{2b} = 0, \\
22: \quad & g'' + \frac{3gb''}{b} - \frac{3g(b')^2}{2b^2} - 3\,\frac{gb'}{zb}\left(1 + \frac{1}{\nu}\right) - g'\left(\frac{4}{z} + \frac{2}{\nu z} - \frac{3b'}{b}\right) + \frac{2g}{z^2}\left(3 + \frac{2}{\nu} + \frac{1}{\nu^2}\right) + \frac{g}{2}(\phi')^2 + \\
& + \frac{bV}{z^2} - \frac{z^2 f_1 (A_t')^2}{2b} - \frac{q^2 z^{-2+\frac{4}{\nu}} f_2}{2b} = 0, \\
44: \quad & - \frac{6(b')^2}{b^2} + \frac{12b'}{zb}\left(1 + \frac{1}{\nu}\right) + \frac{g'}{g}\left(\frac{2}{z} + \frac{4}{\nu z} - \frac{3b'}{b}\right) - \frac{4}{z^2}\left(1 + \frac{4}{\nu} + \frac{1}{\nu^2}\right) + (\phi')^2 - \frac{2bV}{z^2 g} - \\
& - \frac{z^2 f_1 (A_t')^2}{bg} - \frac{q^2 z^{-2+\frac{4}{\nu}} f_2}{bg} = 0,
\end{aligned}
\tag{A.1}
$$

where $' = \partial/\partial z$.

These equations can be transformed to the following equations

$$
g'' + g'\left(\frac{3b'}{2b} - \frac{1}{z} - \frac{2}{\nu z}\right) - \frac{z^2}{b}\, f_1 (A_t')^2 = 0, \tag{A.2}
$$

$$
2g'\left(1 - \frac{1}{\nu}\right) + g\left(1 - \frac{1}{\nu}\right)\left(\frac{3b'}{b} - \frac{4}{z} - \frac{4}{\nu z}\right) + \frac{q^2 z^{-1+\frac{4}{\nu}} f_2}{b} = 0, \tag{A.3}
$$

$$
b'' - \frac{3(b')^2}{2b} + \frac{2b'}{z} - \frac{4b}{3\nu z^2}\left(1 - \frac{1}{\nu}\right) + \frac{b}{3}(\phi')^2 = 0, \tag{A.4}
$$

$$
\frac{b''}{b} + \frac{(b')^2}{2b^2} + \frac{3b'}{b}\left(\frac{g'}{2g} - \frac{1}{z} - \frac{1}{\nu z}\right) - \frac{g'}{3zg}\frac{5\nu + 4}{\nu} + \frac{4(2\nu^2 + 3\nu + 1)}{3z^2\nu^2} + \frac{g''}{3g} + \frac{2bV}{3z^2 g} = 0. \tag{A.5}
$$

Substituting expressions for g'' from (A.2) and b'' from (A.4) into (A.5) we get the expression for V without g'' and b''

$$V = -\frac{z^4 A_t'^2 f_1}{2b^2} - \frac{3z^2 b' g'}{2b^2} - \frac{3z^2 g b'^2}{b^3} + \frac{9zgb'}{2\nu b^2} + \frac{15zgb'}{2b^2} + \frac{zg'}{\nu b} + \frac{2zg'}{b} + \frac{z^2 g\phi'^2}{2b} - \frac{8g}{\nu b} - \frac{4g}{b}, \tag{A.6}$$

that is nothing but the constraint equation.

One can check explicitly, that from eqs. (A.2)–(A.4) and (A.6) follows the field equation for the scalar field (2.9). Indeed, differentiating (A.6) we get

$$\begin{aligned}
&\frac{b}{z^2 g}\frac{\partial V}{\partial \phi} = \frac{1}{2\nu z^2 b^3 g\phi'} \\
&\Big\{2zbb'\left(\nu z^3 A_t'^2 f_1 - 3g\left(2\nu z b'' + (7\nu+3)b'\right)\right) - \\
&- b^2\Big[z(\nu z(z^2 A_t'^2\phi' f_1' + 3b''g') + b'(3\nu z g'' + (-5\nu-7)g')) + \\
&+ 2\nu z^3 A_t' f_1(\phi)\left(zA_t'' + 2A_t'\right) + g\left(b'\left(-23\nu + \nu z^2\phi'^2 - 25\right) - 3(5\nu+3)zb''\right)\Big] + \\
&+ 18\nu z^2 g b'^3 + b^3\left[2z\left((2\nu+1)g'' + \nu g\phi'\left(z\phi'' + \phi'\right)\right) + g'\left(-4\nu + \nu z^2\phi'^2 - 14\right)\right]\Big\}.
\end{aligned} \tag{A.7}$$

Substituting in the R.H.S. of (A.7) g'' and b'' from (A.2) and (A.4), respectively, we get the following expression for $\frac{\partial V}{\partial \phi}$ without g'' and b'':

$$\begin{aligned}
&\frac{b}{z^2 g}\frac{\partial V}{\partial \phi} = \frac{1}{4\nu^3 z^3 b^2 g\phi'}\Big\{2\nu zb\Big[\nu z\left(\nu z^3 A_t'^2\phi' f_1' + 2(\nu-1)b'g'\right) + \\
&+ 2(\nu-1)\nu z^3 A_t'^2 f_1 + gb'\left(-7\nu^2 - 9\nu + 3\nu^2 z^2\phi\prime\, 2 + 16\right)\Big] + 9(\nu-1)\nu^2 z^2 g b'^2 + \\
&+ 2b^2\Big[2\nu z g'\left(-4\nu + \nu^2 z^2\phi\prime\, 2 + 4\right) + g\left(4\left(5\nu^2 - 2\nu - 3\right) + 2\nu^3 z^3\phi'\phi'' - 3(\nu+1)\nu^2 z^2\phi\prime\, 2\right)\Big]\Big\}.
\end{aligned} \tag{A.8}$$

In a similar way we get the expression for f_2' without g'' and b''. Indeed, we differentiate (A.3) and obtain

$$\begin{aligned}
\frac{q^2 z^{\frac{4}{\nu}-2}}{2bg}\frac{\partial f_2}{\partial \phi} = \frac{q^2 z^{\frac{4}{\nu}-2} f_2'}{2bg\phi'} = &-\frac{(\nu-1)}{2\nu^3 z^3 bg\phi'}\Big\{\nu z\left(5\nu z b'g' - g\left[(\nu+16)b' - 3\nu z b''\right)\right] + \\
&+ 2b\left[\nu z\left(\nu z g'' - (\nu+6)g'\right) + 8(\nu+1)g\right]\Big\}.
\end{aligned} \tag{A.9}$$

Then we substitute there (A.2) and (A.4) and get

$$\begin{aligned}
&\frac{q^2 z^{\frac{4}{\nu}-2}}{2bg}\frac{\partial f_2}{\partial \phi} = \frac{(\nu-1)}{4\nu^3 z^3 b^2 g\phi'}\Big\{2\nu zb\left(b'\left((7\nu+16)g - 2\nu z g'\right) - 2\nu z^3 A_t\prime\, 2 f_1(\phi)\right) - \\
&- 9\nu^2 z^2 g b'^2 + 2b^2\left(8\nu z g' + g\left(-20\nu + \nu^2 z^2\phi'^2 - 12\right)\right)\Big\}.
\end{aligned} \tag{A.10}$$

From (A.8) and (A.10) we get

$$\frac{q^2 z^{-2+\frac{4}{\nu}}}{8bg}\frac{\partial f_2}{\partial\phi}+\frac{b}{z^2 g}\frac{\partial V}{\partial\phi}=\phi''+\phi'\left(\frac{g'}{g}+\frac{3b'}{2b}-\frac{\nu+2}{\nu z}\right)+\frac{z^2(A_t')^2}{2bg}\frac{\partial f_1}{\partial\phi}. \tag{A.11}$$

This is nothing but E.O.M. for the scalar field.

B Simplest solutions to system (2.5)–(2.10)

B.1 Solutions for anisotropic metric $\nu \neq 1$ and $c = 0$, $A_t \neq 0$

The system (2.5)–(2.10) for anisotropic metric $\nu \neq 1$ and $b(z) = 1$, $A_t \neq 0$ has the form

$$g''+g'\left(-\frac{1}{z}-\frac{2}{\nu z}\right)-z^2\, f_1 A_t'^2=0, \tag{B.1}$$

$$-\frac{4}{\nu z^2}\left(1-\frac{1}{\nu}\right)+\phi'^2=0, \tag{B.2}$$

$$2g'\left(1-\frac{1}{\nu}\right)+g\left(1-\frac{1}{\nu}\right)\left(-\frac{4}{z}-\frac{4}{\nu z}\right)+q^2 z^{-1+\frac{4}{\nu}} f_2=0, \tag{B.3}$$

$$-V-\frac{z^4}{2}A_t'^2 f_1+\frac{zg'}{\nu}+2zg'+\frac{z^2 g\,\phi'^2}{2}-\frac{8g}{\nu}-4g=0. \tag{B.4}$$

Substituting ϕ'^2 from (B.2) into (B.4) we get

$$-V-\frac{z^4}{2}A_t'^2 f_1+\frac{zg'}{\nu}+2zg'-\frac{2g}{\nu^2}-\frac{6g}{\nu}-4g=0. \tag{B.5}$$

The variation of the action (2.1) over scalar field ϕ and components $A_\mu^{(1)}$ of the first Maxwell fields' leads to the following EOM:

$$\phi''+\phi'\left(\frac{g'}{g}-\frac{\nu+2}{\nu z}\right)+\frac{z^2 A_t'^2}{2g}\frac{\partial f_1}{\partial\phi}-\frac{q^2 z^{-2+\frac{4}{\nu}}}{2g}\frac{\partial f_2}{\partial\phi}-\frac{b}{z^2 g}\frac{\partial V}{\partial\phi}=0, \tag{B.6}$$

$$A_t''+A_t'\left(\frac{f_1'}{f_1}-\frac{2-\nu}{\nu z}\right)=0. \tag{B.7}$$

The last equation (B.7) gives

$$\log A_t'=-\log f_1+\frac{2-\nu}{\nu}\log z+\log C_1 \Rightarrow A_t'=C_1\frac{z^{\frac{2-\nu}{\nu}}}{f_1}. \tag{B.8}$$

If we take f_1 as in (2.17) we get

$$A_t' = C_1 \frac{z^{\frac{2-\nu}{\nu}}}{z^{-2+\frac{2}{\nu}}} = C_1 z, \tag{B.9}$$

$$A_t(z) = \frac{C_1}{2} z^2 + C_2. \tag{B.10}$$

Taking into account

$$A_t(0) = C_2 = \mu, \tag{B.11}$$

$$A_t(z_h) = \frac{C_1}{2} z_h^2 + \mu = 0, \tag{B.12}$$

we get

$$A_t(z) = \mu\ (1 - z^2/z_h^2). \tag{B.13}$$

Substituting this to the blacking function equation (B.1) we get

$$g'' + g' \left(-\frac{1}{z} - \frac{2}{\nu z} \right) - 4\mu^2 \frac{z^{2+\frac{2}{\nu}}}{z_h^4} = 0. \tag{B.14}$$

From (B.2) we get for the scalar field

$$\phi' = \pm \sqrt{\frac{4}{\nu z^2} \left(1 - \frac{1}{\nu} \right)} = \frac{2}{\nu\, z} \sqrt{\nu - 1} \tag{B.15}$$

and

$$\phi = \frac{2}{\nu} \sqrt{\nu - 1}\ \log z + C_5. \tag{B.16}$$

From (B.3) we get f_2

$$f_2 = -\, q^2 z^{-1+\frac{4}{\nu}} \left[2g' \left(1 - \frac{1}{\nu} \right) + g \left(1 - \frac{1}{\nu} \right) \left(-\frac{4}{z} - \frac{4}{\nu z} \right) \right] = \tag{B.17}$$

and from (B.4) we get

$$V = -\, \frac{z^4}{2} A_t'^2 f_1 + \frac{z g'}{\nu} + 2 z g' + \frac{z^2 g \phi'^2}{2} - \frac{8g}{\nu} - 4g = \tag{B.18}$$

B.2 Solutions for anisotropic metric $\nu \neq 1$ and $c = 0$, $A_t = 0$

From the previous consideration it is easy to reproduce the solution has been found in [33].

From (2.5) we find

$$g(z) = 1 - \frac{z^{2+\frac{2}{\nu}}}{z_h^{2+\frac{2}{\nu}}}, \tag{B.19}$$

Second, we substitute (B.19) into (2.6) and get

$$f_2(z) = \frac{4z^{-4/\nu}}{q^2} \frac{(\nu-1)(1+3\nu+2\nu^2)}{\nu^2\ (1+2\nu)}, \tag{B.20}$$

Then we solve (**??**):

$$\phi(z) = C_5 \pm 2\ \frac{\sqrt{\nu-1}}{\nu}\ \log(z), \tag{B.21}$$

Finally, we have to find V from (2.8) and check the scalar equation (2.9). Substituting (B.19) into (2.8) we obtain

$$V(z) = -\ 2\ \frac{(1+\nu)(1+2\nu)}{\nu^2}. \tag{B.22}$$

Hence we get the solution given by (B.19), (B.20), (B.21) and (B.22), that coincides with [33].

B.3 Vacuum solutions

Without black brane, i.e. for $g = 1$ the EOM (2.5)–(2.10) transform to:

$$\frac{z^2}{b} f_1 A_t'^2 = 0, \tag{B.23}$$

$$b'' - \frac{3(b')^2}{2b} + \frac{2b'}{z} - \frac{4b}{3\nu z^2}\left(1 - \frac{1}{\nu}\right) + \frac{b}{3}(\phi')^2 = 0, \tag{B.24}$$

$$\left(1 - \frac{1}{\nu}\right)\left(\frac{3b'}{b} - \frac{4}{z} - \frac{4}{\nu z}\right) + \frac{q^2 z^{-1+\frac{4}{\nu}}}{b} f_2 = 0, \tag{B.25}$$

$$-V - \frac{z^4}{2b^2} A_t'^2 f_1 - \frac{3z^2 b'^2}{b^3} + \frac{9zb'}{2\nu b^2} + \frac{15zb'}{2b^2} + \frac{z^2\phi'^2}{2b} - \frac{8}{\nu b} - \frac{4}{b} = 0, \tag{B.26}$$

$$\phi'' + \phi'\left(\frac{3b'}{2b} - \frac{\nu+2}{\nu z}\right) + \frac{z^2 A_t'^2}{2b}\frac{\partial f_1}{\partial \phi} - \frac{q^2 z^{-2+\frac{4}{\nu}}}{2b}\frac{\partial f_2}{\partial \phi} - \frac{b}{z^2}\frac{\partial V}{\partial \phi} = 0, \tag{B.27}$$

$$A_t'' + A_t'\left(\frac{b'}{2b} + \frac{f_1'}{f_1} - \frac{2-\nu}{\nu z}\right) = 0. \tag{B.28}$$

For $b = e^{\frac{cz^2}{2}}$:

$$z^2\, e^{-\frac{cz^2}{2}} f_1 A_t'^2 = 0, \tag{B.29}$$

$$\frac{c^2 z^2}{2} - 3c + \frac{4}{3}\frac{\nu-1}{\nu^2 z^2} - \frac{(\phi')^2}{3} = 0, \tag{B.30}$$

$$\left(1-\frac{1}{\nu}\right)\left(3cz - \frac{4(\nu+1)}{\nu z}\right) + z^{-1+\frac{4}{\nu}}\, e^{-\frac{cz^2}{2}} f_2\, q^2 = 0, \tag{B.31}$$

$$\frac{3c^2 z^2}{2} - c\left(2+\frac{3}{\nu}\right) + \frac{4}{3z^2}\left(2+\frac{3}{\nu}+\frac{1}{\nu^2}\right) + \frac{2e^{\frac{cz^2}{2}}}{3z^2} V = 0, \tag{B.32}$$

$$\phi'' + \phi'\left(\frac{3cz}{2} - \frac{\nu+2}{\nu z}\right) + \frac{z^2\, e^{-\frac{cz^2}{2}}}{2}\frac{\partial f_1}{\partial \phi} A_t'^2 - \frac{z^{-2+\frac{4}{\nu}}\, e^{-\frac{cz^2}{2}}}{2}\frac{\partial f_2}{\partial \phi}\, q^2 - $$

$$- \frac{e^{\frac{cz^2}{2}}}{z^2}\frac{\partial V}{\partial \phi} = 0, \tag{B.33}$$

$$A_t'' + A_t'\left(\frac{cz}{2} - \frac{2-\nu}{\nu z} + \frac{f_1'}{f_1}\right) = 0 \tag{B.34}$$

The system (B.29)–(B.34) has the solution:

$$A_t = \mu, \tag{B.35}$$

$$f_2 = z^{-\frac{4}{\nu}}\, \frac{1-\nu}{\nu^2 q^2}\left(3cz^2 - 4(\nu+1)\right) e^{\frac{cz^2}{2}}, \tag{B.36}$$

$$\phi = \frac{1}{2\sqrt{2}\,\nu}\Bigg\{ \sqrt{3c^2\nu^2 z^4 - 18c\,\nu^2 z^2 + 8\,(\nu-1)} - \sqrt{3c^2\nu^2 z_*^4 - 18c\,\nu^2 z_*^2 + 8\,(\nu-1)} + \tag{B.37}$$

$$+\ 2\sqrt{2\,(\nu-1)}\ln\left(\frac{z^2}{z_*^2}\right) - 3\sqrt{3}\,\nu\ln\left(\frac{\sqrt{3c^2\nu^2 z^4 - 18c\,\nu^2 z^2 + 8\,(\nu-1)} - \sqrt{3}\,\nu\,(3-cz^2)}{\sqrt{3c^2\nu^2 z_*^4 - 18c\,\nu^2 z_*^2 + 8\,(\nu-1)} - \sqrt{3}\,\nu\,(3-cz_*^2)}\right) -$$

$$-\ 2\sqrt{2\,(\nu-1)}\ln\left(\frac{9c\,\nu^2 z^2 - 8\,(\nu-1) - \sqrt{2\,(\nu-1)}\,\sqrt{3c^2\nu^2 z^4 - 18c\,\nu^2 z^2 + 8\,(\nu-1)}}{9c\,\nu^2 z_*^2 - 8\,(\nu-1) - \sqrt{2\,(\nu-1)}\,\sqrt{3c^2\nu^2 z_*^4 - 18c\,\nu^2 z_*^2 + 8\,(\nu-1)}}\right)\Bigg\},$$

$$V = -\frac{1}{4}\left[9c^2 z^4 - 6cz^2\left(2+\frac{3}{\nu}\right) + 8\left(2+\frac{3}{\nu}+\frac{1}{\nu^2}\right)\right] e^{-\frac{cz^2}{2}}. \tag{B.38}$$

The particular form of factor f_1 doesn't matter as it is coupled with the constant function A_t, so all the terms containing f_1 also include $A_t' \equiv 0$. The scalar field ϕ isn't influenced by the assumption $g = 1$ and coincides with (2.57). The only difference is that z_h loses its sense as without the black brane there is no horizon any more. Therefore we should replace z_h by some z_*, whose main property is $\phi(z_*) = 0$.

If we substitute (B.36)–(B.38) into the equation (B.33) its left-hand side disappears proving that the system (B.29)–(B.34) still remains a self-consistent one.

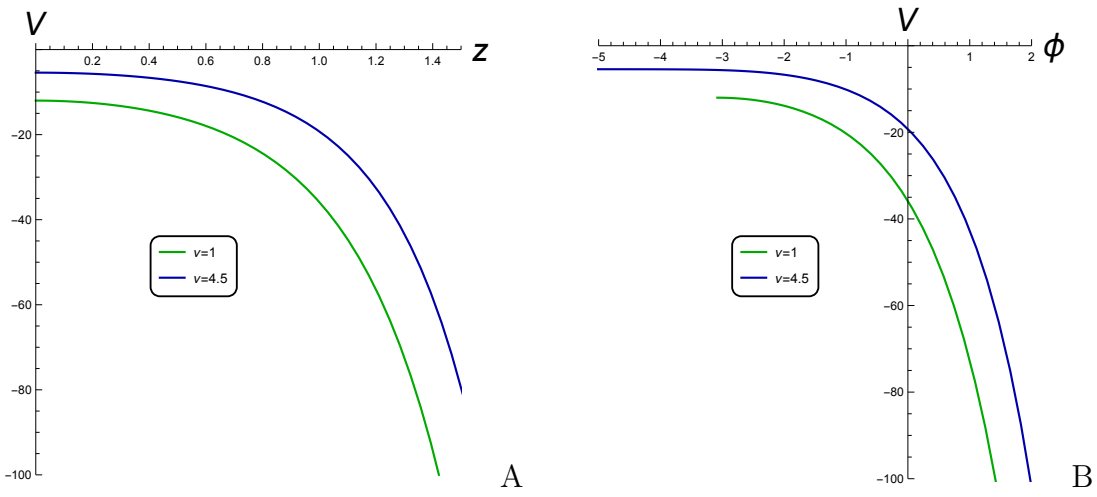


Figure 45. Dilaton potentials that support vacuum solutions corresponding to isotropic and anisotropic cases $\nu = 4.5$ with $c = -1$ and initial conditions $\phi(1) = 0$ as function of z A) and ϕ B).

References

[1] H. T. Ding, F. Karsch and S. Mukherjee, "Thermodynamics of strong-interaction matter from Lattice QCD", Int. J. Mod. Phys. E **24**, 1530007 (2015) [arXiv:1504.05274 [hep-lat]].

[2] M. A. Stephanov, "QCD phase diagram and the critical point", Prog. Theor. Phys. Suppl. **153**, 139-156 (2004) [hep-ph/0402115].

[3] J. Casalderrey-Solana, H. Liu, D. Mateos, K. Rajagopal and U. A. Wiedemann, *Gauge/String Duality, Hot QCD and Heavy Ion Collisions*, (Cambridge University Press, 2014) [arXiv:1101.0618 [hep-th]].

[4] I. Ya. Aref'eva, "Holographic approach to quark-gluon plasma in heavy ion collisions", Phys. Usp. **57**, 527 (2014).

[5] O. DeWolfe, S. S. Gubser, C. Rosen and D. Teaney, "Heavy ions and string theory", Prog. Part. Nucl. Phys. **75**, 86 (2014).

[6] M. Strickland, "Thermalization and isotropization in heavy-ion collisions", *Pramana* **84**, 671 (2015).

[7] I. Ya. Aref'eva and A. A. Golubtsova, "Shock waves in Lifshitz-like spacetimes", JHEP **1504**, 011 (2015) [arXiv:1410.4595 [hep-th]].

[8] J. Adam *et al.* [ALICE Collab.], "Centrality dependence of the charged-particle multiplicity density at midrapidity in Pb-Pb collisions at $\sqrt{s_{\rm NN}} = 5.02$ TeV", Phys. Rev. Lett. **116**, 222302 (2016) [arXiv:1512.06104 [nucl-ex]].

[9] S. S. Gubser, S. S. Pufu and A. Yarom, "Entropy production in collisions of gravitational shock waves and of heavy ions", Phys. Rev. D **78**, 066014 (2008) [arXiv:0805.1551 [hep-th]].

[10] S. S. Gubser, S. S. Pufu and A. Yarom, "Off-center collisions in AdS(5) with applications to multiplicity estimates in heavy-ion collisions", JHEP **0911**, 050 (2009) [arXiv:0902.4062 [hep-th]].

[11] L. Alvarez-Gaume, C. Gomez, A. Sabio Vera, A. Tavanfar, M. A. Vazquez-Mozo et al., "Critical formation of trapped surfaces in the collision of gravitational shock waves", JHEP **0902**, 009 (2009) [arXiv:0811.3969 [hep-th]].

[12] S. Lin and E. Shuryak, "Grazing Collisions of Gravitational Shock Waves and Entropy Production in Heavy Ion Collision", Phys. Rev. D **79**, 124015 (2009) [arXiv:0902.1508 [hep-th]].

[13] J. L. Albacete, Y. V. Kovchegov and A. Taliotis, "Asymmetric Collision of Two Shock Waves in AdS(5)", JHEP **0905**, 060 (2009) [arXiv:0902.3046 [hep-th]].

[14] I. Ya. Aref'eva, A. A. Bagrov and E. A. Guseva, "Critical Formation of Trapped Surfaces in the Collision of Non-expanding Gravitational Shock Waves in de Sitter Space-Time", JHEP **0912**, 009 (2009) [arXiv:0905.1087 [hep-th]].

[15] I. Ya. Aref'eva, A. A. Bagrov and L. V. Joukovskaya, "Critical Trapped Surfaces Formation in the Collision of Ultrarelativistic Charges in (A)dS", JHEP **1003**, 002 (2010) [arXiv:0909.1294 [hep-th]].

[16] Y. V. Kovchegov and S. Lin, "Toward Thermalization in Heavy Ion Collisions at Strong Coupling", JHEP **1003**, 057 (2010) [arXiv:0911.4707 [hep-th]].

[17] Y. V. Kovchegov, "Shock Wave Collisions and Thermalization in AdS_5", Prog. Theor. Phys. Suppl. **187**, 96 (2011) [arXiv:1011.0711 [hep-th]].

[18] E. Kiritsis and A. Taliotis, "Multiplicities from black-hole formation in heavy-ion collisions", JHEP **1204**, 065 (2012) [arXiv:1111.1931 [hep-ph]].

[19] I. Ya. Aref'eva, E. O. Pozdeeva and T. O. Pozdeeva, "Holographic estimation of multiplicity and membranes collision in modified spaces AdS_5", Theor. Math. Phys. **176**, 861 (2013) [arXiv:1401.1180 [hep-th]].

[20] I. Ya. Aref'eva, E. O. Pozdeeva and T. O. Pozdeeva, "Potentials in modified AdS_5 spaces with a moderate increase in entropy", Teor. Mat. Fiz. **180**, 35 (2014).

[21] D. S. Ageev and I. Ya. Aref'eva, "Holographic thermalization in a quark confining background", J. Exp. Theor. Phys. **120**, 436 (2015) [arXiv:1409.7558 [hep-th]].

[22] U. Gursoy, E. Kiritsis, L. Mazzanti and F. Nitti, "Holography and Thermodynamics of 5D Dilaton-gravity", JHEP **0905**, 033 (2009) [arXiv:0812.0792 [hep-th]];

[23] D. Mateos and D. Trancanelli, "Thermodynamics and Instabilities of a Strongly Coupled Anisotropic Plasma", JHEP **1107**, 054 (2011) [arXiv:1106.1637 [hep-th]].

[24] D. Mateos and D. Trancanelli, "The anisotropic N=4 super Yang-Mills plasma and its instabilities", Phys. Rev. Lett. **107**, 101601 (2011) [arXiv:1105.3472 [hep-th]].

[25] M. Chernicoff, D. Fernandez, D. Mateos and D. Trancanelli, "Drag force in a strongly coupled anisotropic plasma", JHEP **1208**, 100 (2012) [arXiv:1202.3696 [hep-th]].

[26] M. Chernicoff, D. Fernandez, D. Mateos and D. Trancanelli, "Jet quenching in a strongly coupled anisotropic plasma", JHEP **1208**, 041 (2012) [arXiv:1203.0561 [hep-th]].

[27] M. Chernicoff, D. Fernandez, D. Mateos and D. Trancanelli, "Quarkonium dissociation by anisotropy", JHEP **1301**, 170 (2013) [arXiv:1208.2672 [hep-th]].

[28] L. Patino and D. Trancanelli, "Thermal photon production in a strongly coupled anisotropic plasma", JHEP **1302**, 154 (2013) [arXiv:1211.2199 [hep-th]].

[29] D. Giataganas, "Observables in Strongly Coupled Anisotropic Theories", PoS Corfu **2012**, 122 (2013).

[30] V. Jahnke, A. Luna, L. Patino and D. Trancanelli, "More on thermal probes of a strongly coupled anisotropic plasma", JHEP **1401**, 149 (2014) [arXiv:1311.5513 [hep-th]].

[31] I. Ya. Aref'eva, "Formation time of quark-gluon plasma in heavy-ion collisions in the holographic shock wave model", Theor. Math. Phys. **184**, 1239 (2015) [arXiv:1503.02185 [hep-th]].

[32] D. Avila, D. Fernandez, L. Patino and D. Trancanelli, "Thermodynamics of anisotropic branes", JHEP **1611**, 132 (2016) [arXiv:1609.02167 [hep-th]].

[33] I. Ya. Aref'eva, A. A. Golubtsova and E. Gourgoulhon, "Analytic black branes in Lifshitz-like backgrounds and thermalization", JHEP **1609**, 142 (2016) [arXiv:1601.06046 [hep-th]].

[34] I. Aref'eva, "Multiplicity and theremalization time in heavy-ions collisions", EPJ Web Conf. **125**, 01007 (2016).

[35] I. Ya. Aref'eva, "Holography for Heavy Ions Collisions at LHC and NICA", EPJ Web Conf. **164**, 01014 (2017) [arXiv:1612.08928 [hep-th]].

[36] D. Giataganas, U. Gursoy and J. F. Pedraza, "Strongly-coupled anisotropic gauge theories and holography", [arXiv:1708.05691 [hep-th]].

[37] O. Andreev and V. I. Zakharov, "Heavy-quark potentials and AdS/QCD", Phys. Rev. D **74**, 025023 (2006) [arXiv:0604204 [hep-ph]].

[38] A. Karch, E. Katz, D. T. Son and M. A. Stephanov, "Linear confinement and AdS/QCD", Phys. Rev. D **74**, 015005 (2006) [arXiv:0602229 [hep-ph]].

[39] C. D. White, "The Cornell potential from general geometries in AdS / QCD", Phys. Lett. B **652**, 79 (2007) [arXiv:0701157 [hep-ph]].

[40] H. J. Pirner and B. Galow, "Strong Equivalence of the AdS-Metric and the QCD Running Coupling", Phys. Lett. B **679**, 51 (2009) [arXiv:0903.2701 [hep-ph]].

[41] A. Karch, E. Katz, D. T. Son and M. A. Stephanov, "On the sign of the dilaton in the soft wall models", JHEP **1104**, 066 (2011) [arXiv:1012.4813 [hep-ph]].

[42] O. Andreev, "Cold Quark Matter, Quadratic Corrections and Gauge/String Duality", Phys. Rev. D **81**, 087901 (2010) [arXiv:1001.4414 [hep-ph]].

[43] P. Colangelo, F. Giannuzzi and S. Nicotri, "Holography, Heavy-Quark Free Energy, and the QCD Phase Diagram", Phys. Rev. D **83**, 035015 (2011) [arXiv:1008.3116 [hep-ph]].

[44] D. Li, S. He, M. Huang and Q.-S. Yan, "Thermodynamics of deformed AdS5 model

with a positive/negative quadratic correction in graviton-dilaton system", JHEP **1109**, 041 (2011) [arXiv:1103.5389 [hep-th]].

[45] S. He, S.-Y. Wu, Y. Yang and P.-H. Yuan, "Phase Structure in a Dynamical Soft-Wall Holographic QCD Model", JHEP **04**, 093 (2013) [arXiv:1301.0385 [hep-th]].

[46] Y. Yang and P.-H. Yuan, "Confinement-deconfinement phase transition for heavy quarks in a soft wall holographic QCD model", JHEP **1512**, 161 (2015) [arXiv:1506.05930 [hep-th]].

[47] R.-G. Cai, S. He and D. Li, "hQCD model and its phase diagram in Einstein-Maxwell-Dilaton system", JHEP **1203**, 033 (2012) [arXiv:1201.0820 [hep-th]].

[48] R.-G. Cai, S. Chakrabortty, S. He and L. Li, "Some aspects of QGP phase in a hQCD model", JHEP **1302**, 068 (2013) [arXiv:1209.4512 [hep-th]].

[49] M. W. Li, Y. Yang and P. H. Yuan, "Approaching Confinement Structure for Light Quarks in a Holographic Soft Wall QCD Model", Phys. Rev. D **96**, 066013 (2017) [arXiv:1703.09184 [hep-th]].

[50] A. Chamblin, R. Emparan, C. V. Johnson and R. C. Myers, "Charged AdS black holes and catastrophic holography", Phys. Rev. D **60**, 064018 (1999) [arXiv:9902170 [hep-th]].

[51] O. DeWolfe, S. S. Gubser and C. Rosen, "A holographic critical point", Phys. Rev. D **83**, 086005 (2011) [arXiv:1012.1864 [hep-th]].

[52] O. DeWolfe, S. S. Gubser and C. Rosen, "Dynamic critical phenomena at a holographic critical point", Phys. Rev. D **84**, 126014 (2011) [arXiv:1108.2029 [hep-th]].

[53] J. Knaute, R. Yaresko and B. Kampfer, "Holographic QCD phase diagram with critical point from Einstein-Maxwell-dilaton dynamics", Phys. Lett. B **778**, 419 (2018) [arXiv:1702.06731 [hep-ph]].

[54] E. Brehm, "Heavy Quarks in Strongly Coupled Non-Conformal Plasmas with Anisotropy", [arXiv:1711.08943 [hep-th]].

[55] D. Dudal and S. Mahapatra, "Thermal entropy of a quark-antiquark pair above and below deconfinement from a dynamical holographic QCD model", Phys. Rev. D **90** 126010 (2017) [arXiv:1708.06995 [hep-th]].

[56] I. S. Gradshteyn and I. M. Ryzhik, "Table of integrals, Series, an Products", 5-th edition, 8.35 The incomplete gamma functions.

[57] I. Ya. Aref'eva, A. A. Golubtsova and G. Policastro, "Exact holographic RG flows and the $A_1 \times A_1$ Toda chain", [arXiv:1803.06764 [hep-th]].

[58] E. Kiritsis, W. Li and F. Nitti, "Holographic RG flow and the Quantum Effective Action", Fortsch. Phys. **62**, 389 (2014) [arXiv:1401.0888 [hep-th]].